

VILNIUS UNIVERSITY
CENTER FOR PHYSICAL SCIENCES AND TECHNOLOGY

JUSTINA GAIDUKEVIČ

NANO-STRUCTURED GRAPHENE CATALYSTS, CATALYST
SUPPORTS AND COATINGS: SYNTHESIS AND INVESTIGATION

Doctoral dissertation
Physical Sciences, Chemistry (03 P)

Vilnius, 2017

The dissertation was carried out at the Vilnius University in the period of 2013–2017.

Scientific supervisor:

Prof. dr. Jurgis Barkauskas (Vilnius University, Physical Sciences, Chemistry - 03 P).

Scientific consultant:

Prof. dr. habil. Mieczysław Kozłowski (Adam Mickiewicz University in Poznań, Poland, Physical Sciences, Chemistry - 03 P).

VILNIAUS UNIVERSITETAS
FIZINIŲ IR TECHNOLOGIJOS MOKSLŲ CENTRAS

JUSTINA GAIDUKEVIČ

NANOSTRUKTŪRINIŲ GRAFENO KATALIZATORIŲ,
KATALIZATORIŲ NEŠIKLIŲ IR DANGŲ SINTEZĖ BEI TYRIMAS

Daktaro disertacija
Fiziniai mokslai, chemija (03 P)

Vilnius, 2017

Disertacija rengta 2013 – 2017 metais Vilniaus universitete.

Mokslinis vadovas:

Prof. dr. Jurgis Barkauskas (Vilniaus universitetas, fiziniai mokslai, chemija - 03 P).

Mokslinis konsultantas:

Prof. dr. habil. Mieczysław Kozłowski (Adomo Mickevičiaus universitetas Poznanėje, Lenkija, fiziniai mokslai, chemija - 03 P).

CONTENTS

LIST OF ABBREVIATIONS.....	7
INTRODUCTION	10
1. LITERATURE SURVEY	14
1.1. Carbon nanomaterials.....	14
1.2. Catalysis on carbon nanomaterials.....	19
1.2.1. Transesterification process for biodiesel production.....	20
1.2.2. Electrocatalysts for oxygen reduction reaction.....	24
1.2.3. Carbon materials as catalyst supports.....	27
1.3. Graphene-based coatings: preparation and transfer	33
2. EXPERIMENTAL.....	38
2.1. Materials and reagents.....	38
2.2. Synthesis methods	39
2.2.1. Synthesis of graphite oxide.....	39
2.2.2. Thermal reduction of graphite oxide.....	40
2.2.3. Synthesis of catalytically active materials for transesterification reaction.....	41
2.2.4. Synthesis of catalytically active materials for oxygen reduction reaction.....	43
2.2.5. Preparation of graphene oxide coatings	46
2.3. Characterization techniques	52
2.4. Activity studies.....	56
3. RESULTS AND DISCUSSION	59
3.1. Graphene-based heterogeneous catalysts for transesterification process	59
3.1.1. Structural characterizations of graphene-based acidic catalysts.....	59
3.1.2. Activity of solid acidic catalysts	73
3.1.3. Structural characterizations of graphene-based basic catalyst.....	76
3.1.4. Activity of solid basic catalysts	91
3.2. Graphene-based nanocomposite material containing (SCN) _n as highly efficient electrocatalyst for ORR.....	93

3.2.1. Structural characterizations.....	93
3.2.2. Electrochemical study.....	108
3.3. Thermally reduced graphene oxide as support material for D-fructose biosensor.....	114
3.3.1. Examination of TRGO fractions	114
3.4. Optimization of the transfer process of graphene oxide coatings	122
CONCLUSIONS	135
LIST OF PUBLICATIONS	138
ACKNOWLEDGEMENTS.....	142
REFERENCES	143

LIST OF ABBREVIATIONS

GO	Graphene oxide;
rGO	Reduced graphene oxide;
GrO	Graphite oxide;
CNTs	Carbon nanotubes;
SWNHs	Single-walled carbon nanohorns;
OLC	Onion-like carbon;
ORR	Oxygen reduction reaction;
TRGO	Thermally reduced graphene oxide;
PQQ	Pyrroloquinoline quinone;
DET	Direct electron transfer;
FAME	Fatty acid methyl ester;
FFAs	Free fatty acids;
VSHE	Potential of standart hydrogen electrode;
Qds	Quantum dots;
DNA	Deoxyribonucleic acid;
CVD	Chemical vapour deposition;
LBL	Layer by layer self-assembling;
LB	Langmuir-Blodgett;
EPD	Electrophoretic deposition;
PET	Polyethylene terephthalate;
PS	Polystyrene;
PI	Polyimide;
PMMA	Poly(methyl-methacrylate);
PIB	Polyisobutylene;
PDMS	Polydimethylsiloxane;
p.a.	Pure Analytical;
BDS	4-aminobenzenesulphonic acid;
DMF	N, N – dimethylformamide;
PEI	Polyethylenimine;

PVA	Poly(vinyl alcohol);
PEO	Poly(ethylene oxide);
AA	Adipic acid;
PVP	Polyvinylpyrrolidone;
SDS	Sodium dodecyl sulphate;
HEC	2-hydroxyethyl cellulose;
PC	Polycarbonate;
MWCO	Cutoff molecular weight;
TRGO1	First fraction of thermally reduced graphene oxide;
TRGO2	Second fraction of thermally reduced graphene oxide;
TRGO3	Third fraction of thermally reduced graphene oxide;
(SCN) _n	Polythiocyanogen;
PB	Plackett-Burman;
CF	Chloroform;
FTIR	Fourier Transform infrared spectroscopy;
XRD	X-ray Powder Diffraction;
FWHM	Full width at half max;
SEM	Scanning electron microscopy;
SEC	Size exclusion chromatography;
XPS	X-ray photoelectron spectroscopy;
CAM	Contact angle measurement;
TG/DTG	Thermogravimetry and differential thermogravimetry;
BET	Brunauer-Emmett-Teller;
FID	Flame ionization detector;
GC	Gas chromatograph;
LSV	Linear sweep voltammetry;
a.u.	Arbitrary unit;
EA	Elemental analysis obtained by CHNS analyser;
deg.	Degree;
M _n	Mean number average molecular weight;
M _w	Mean weight average molecular weight;

PTC film	Polythiocyanogen film;
B.E.	Binding energy;
QSPR	Quantitative Structure Property Relationship;
ER	Electrical resistance.

INTRODUCTION

In recent years a variety of environmental issues in creating alternative fuels, reducing harmful by-products in manufacturing, cleaning up the environment and preventing future pollution, dealing with the causes of global warming, etc., have emerged. Environmental and economical considerations have raised a strong interest to re-design the commercially important processes to avoid the use of harmful substances and the generation of toxic waste. In this respect, there is no doubt that heterogeneous catalysis play a dominant role in the development of environmentally benign processes in petroleum chemistry and in the production of chemicals. Development of catalytic processes for chemical energy conversion from renewable sources is proving to be one of the most pressing and challenging issues for modern science [1-3].

Catalysis play a key role in modern chemical technology, in fact, it is the backbone of chemical industry. Over 90% of all commercially available chemical products involve using catalysts at certain production stage [4]. The most widely applied catalytic materials have been concentrated on the noble metals (Pt, Rh, Pd) and metal oxides, hybrid materials or composite structures with the active metallic centers, and organometallic compounds [5-7]. Although metal-based catalysts have been playing a major role in numerous industrial processes, they still suffer from numerous drawbacks, including their sensitivity to poisoning, high cost and harmful effects on the environment. In addition, the noble metal residues in the reaction systems may hinder the purification process of products. Therefore, developing catalysts from sustainable metal-free materials could be a smart way to overcome these shortcomings. Currently, the research is primarily focused towards nanostructured carbonaceous catalysts with enhanced physicochemical properties [8].

The use of carbon nanomaterials in catalysis has dominated advances in nanotechnology for the last 20 years. Carbon nanomaterials, including carbon black, carbon nanotubes, graphene and their derivatives, are important components of many synthetic catalysts. They have been used as effective

catalysts or as supports for immobilization of active species [9, 10]. Among the carbon materials mentioned above, graphene and its derivatives have recently attracted the most attention [3]. This is mainly due to the fact that graphene has several significant advantages over the other carbon allotropes for developing new catalysts. Graphene has a theoretical specific surface area as high as $2630 \text{ m}^2 \cdot \text{g}^{-1}$, being twice that of single walled carbon nanotubes and much higher than those of most carbon black and activated carbons. This structure characteristic makes graphene highly desirable for potential application as a 2D support for loading catalyst of metals, oxides, enzymes or other carbon nanomaterials [10-12]. Moreover, the superior electron mobility of graphene facilitates the electron transfer during the catalytic reactions, improving its catalytic activity [13]. This new carbon allotrope also has high chemical, thermal, optical and electrochemical stability, which can potentially improve the lifetime of catalysts [11]. Finally, graphene-based materials, especially chemically modified graphene such as graphene oxide (GO) and reduced GO (rGO), which are promising catalysts themselves and may be also attractive components for developing of new catalysts, can be obtained at relatively low cost on a large scale by using graphite, graphite oxide (GrO) as the starting materials [10, 14]. Investigation in new catalytic materials or optimization of existing catalyst systems is of huge importance in order to increase the efficiency of the catalyst, resulting in higher product yields and purities.

Graphene-based materials are widely used in the form of membranes and coatings. Graphene coatings are one of the most promising candidates that may find application in biosensor design, where they serve as a versatile platform for enzyme immobilization, which is key significant to establish an efficient enzymatic bioanalytic system [15, 16]. For this purpose the graphene coatings must be transferred onto arbitrary insulating, flexible substrates. However, it is important to avoid undesirable changes in the structure during the transfer process. To reach this task, it is necessary select the optimum conditions for the transfer process. This is a multiparameter problem, which requires a lot of time and production costs.

The main aim of this research was to prepare graphene-based nanomaterials and validate their potential utility as catalysts for biodiesel production, electrochemical oxygen reduction reaction and enzyme support for biosensor application. The additional aim was to prepare the graphene oxide coatings and optimize the transfer process of these coatings on transparent PET substrate. Therefore, the tasks of the present thesis were formulated as follows:

1. To synthesize and characterize graphite oxide and thermally reduced graphene oxide as well as to design optimized method which would allow to synthesize the different fractions of thermally reduced graphene oxide having specific properties.
2. To produce and characterize functionalized thermally reduced graphene oxide catalysts with either acidic or basic sites on their surface, and to investigate their catalytic activity in the transesterification reaction of rapeseed oil with methanol.
3. To synthesize a new highly electrocatalytically active nanocomposite material derived by solid-solid reaction between graphite oxide and KSCN, to investigate its structure and to evaluate this potential catalyst in terms of electrocatalytic performance for oxygen reduction reaction.
4. To prepare graphene oxide coatings on polycarbonate substrate using filtration method, as well as to optimize the process of transfer of these coatings on the transparent polyethylene terephthalate (PET) substrate using two-stage optimization procedure (Plackett–Burman and simplex design of experiment).

Scientific novelty

1. First time proposed vertical thermal reduction system of graphite oxide allowed us to collect three different fractions of rGO with specific properties.
2. To the best of our knowledge, the novel graphene-based catalysts, not used earlier, have been proposed for the transesterification reaction of rapeseed oil with methanol. It has been shown, that the catalyst obtained by

functionalization of TRGO with 4-aminobenzenesulphonic acid, were a prospective candidates to replace commercial acidic catalyst Amberlyst 15.

3. Novel graphene-based nanocomposite containing inorganic polymer polythiocyanogen was prepared in order to fabricate superior metal-free catalyst for electrochemical oxygen reduction. The electrochemical measurements showed that obtained product exhibited at least 5 times higher catalytic activity towards oxygen reduction reaction compared to that of commercial Pt catalyst.
4. A novel method of preparation of graphene oxide coatings by filtering through a polycarbonate membrane filter was developed in the laboratory. Also for the first time the transfer process of graphene oxide coatings onto PET substrate was developed using a sequence of Plackett–Burman and simplex experimental design methods.

1. LITERATURE SURVEY

1.1. Carbon nanomaterials

Carbon is a remarkable element and has been described as “the master element of living substances” [17]. Carbon atoms characterize the unique ability to form strong covalent bonds between one another or other non-metals in different hybridization states, like sp , sp^2 or sp^3 , which result in a wide range of structures, from small molecules to long chains. There is no other element like carbon that can form such diverse and completely different substances as a single element, in terms of structures and properties, such as diamond, graphite and carbyne. All of these materials are the most well-known carbon allotropes [17, 18]. Over thirty years ago, the classical allotropes of carbon were enriched with the discovery of fullerenes in 1985 [19]. Soon afterwards, carbon nanotubes (CNTs) were also discovered and, since then, a great amount of studies have been dedicated to these new and fascinating forms of carbon [20]. The discoveries of these two key materials, fullerenes and CNTs, were followed by the development of new carbon nanostructures such as single-walled carbon nanohorns (SWNHs), onion-like carbon (OLC) spheres, carbon dots, endohedral fullerenes, graphene and etc [21]. Various forms of carbon nanomaterials are shown in Fig. 1.

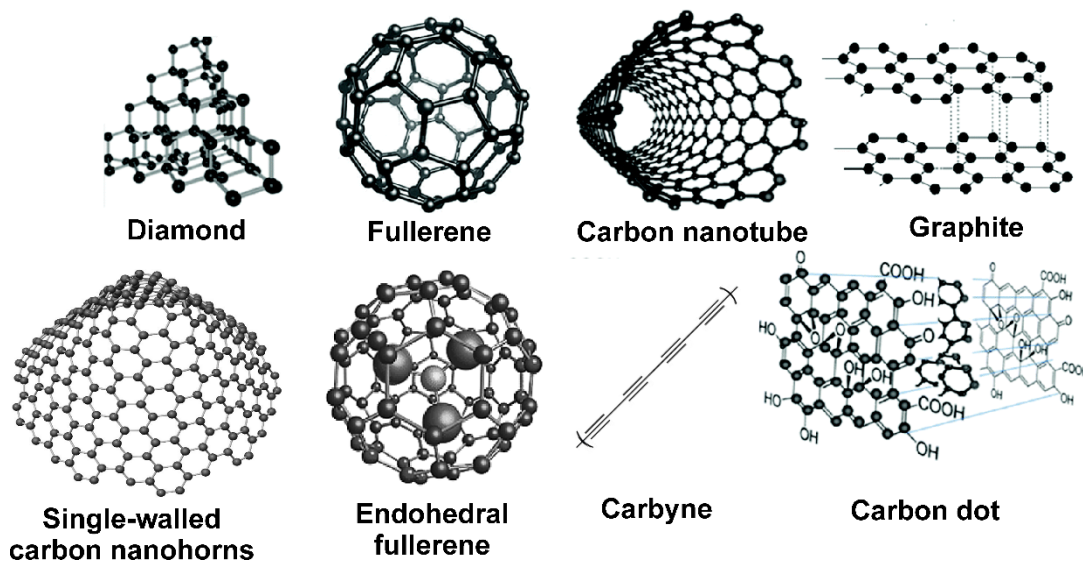


Fig. 1. Representation of possible carbon allotropes [18].

Carbon's versatile bonding has motivated to the discovery of a wide variety of nanostructures, which urgently need a systematic and standard nomenclature [21]. There are numerous ways that carbon nanoforms could be classified. These include their synthesis conditions, physical properties such as density and internal surface area [22]. Carbon nanostructures can be also cut into two general groups on the basis of the predominant types of covalent bonds between carbon atoms. The first group contains the graphene-like nanostructures, which are primarily made up of sp^2 carbon atoms that are densely packed in a hexagonal honeycomb crystal lattice, although they may also contain some sp^3 carbon atoms at the edges or defect sites. This group includes graphene, CNTs, nanohorns, onion-like carbon nanospheres, and carbon dots. The second group of carbon nanoforms contain both sp^3 and sp^2 carbon atoms in various ratios and have mixtures of amorphous and graphitic regions, or consist mainly of sp^3 carbon atoms. Nanodiamond and carbon dots with non-graphitic structures are the only known members of this group [23-25].

It is also possible to classify carbon nanostructures according to their morphological characteristics. To this classification attributed nanostructures with empty internal spaces such as fullerene, carbon nanotubes, and nanohorns. Nanostructures without internal spaces such as nanodiamonds, carbon dots, and onion-like carbon nanospheres would belong to a separate second category under this classification type [23].

Moreover, the carbon nanomaterials may be classified on the basis of their dimensionality. By this classification, carbon nanomaterials could be 0D (fullerenes, OLC structures, carbon dots), 1D (CNTs, carbon nanofibers, and SWNHs), 2D (graphene, graphene nanoribbons) or 3D (diamond, graphite) dimension structures [21, 23].

Two-dimensional (2D) nanomaterials have gained a worldwide attention in recent years because of their outstanding properties. The 2D nanomaterials offer promising opportunities for various applications to be used in an exfoliated state, as single- or few-layer structures, at scientific and technological levels [26]. The most widely known 2D layered material is graphene. This carbon

nanomaterial is the basic structural element of some carbon allotropes and can be considered as mother of all graphitic forms. The graphene nanosheet can be wrapped up into 0D fullerenes, rolled into 1D carbon nanotubes, or stacked into 3D graphite [27]. Graphene is a single layer of carbon atoms bound through sp^2 bonds forming a hexagonal two-dimensional crystal lattice. Each carbon atom is about 0.142 nm from its three neighbours, with each of which it shares one σ bond. The fourth bond is a π -bond, which is directed along the z-axis (out of the plane) [25, 28-30].

Graphene has shown exceptional physical properties, not seen in any other material. It has a very high electron mobility at room temperature, with values of up to $200000 \text{ cm}^2 \cdot \text{V}^{-1} \cdot \text{s}^{-1}$. Theoretically, this new form of carbon is the strongest material in the world, it is about 100 times stronger than steel. The breaking strength is $42 \text{ N} \cdot \text{m}^{-1}$ and the Young's modulus is 1.0 TPa. Similarly it was found that graphene has high optical transparency of 97.7%, high thermal conductivity of up to $5000 \text{ W m}^{-1} \cdot \text{K}^{-1}$, extremely high theoretical specific surface area of $2630 \text{ m}^2 \cdot \text{g}^{-1}$ and is not permeable to gas [11, 31, 32].

The whole complex of mechanical, structural, electronic, thermal and other extraordinary properties have created a number of potential commercial applications for this material. These include the development of electronic devices (e.g. transistors [33], transparent conducting electrodes [34, 35]), sensors for single molecule gas detection [36] and supercapacitors [35]. Graphene has potential applications in fuel cells [37], composites [12], hydrogen storage devices [38], batteries [39]. Moreover, graphene has generated great interest in the field of nanomedicine, nanofiltration, catalysis etc. [40-42]. To fulfil such applications, the preparation of high-quality 2D graphene sheets is a primary criterion. However, the production of graphene on a large scale still remains a challenge and is being explored by many researchers all over the world. To date, different methods have been developed to produce single-layer or few-layer graphene such as mechanical exfoliation [43], liquid-phase exfoliation [44], chemical vapour deposition of hydrocarbons on metal surfaces [45], bottom-up organic synthesis [46], solvothermal synthesis [47], epitaxial

growth on silicon carbide (SiC) surfaces and metal surfaces [48, 49], and unzipping of carbon nanotubes [50]. Unfortunately, these methods are impractical for large-scale synthesis and suffer from the limited controllability over the edge, shape and size of graphene sheets. Concurrently, the preparation of graphene materials by the chemical reduction of graphite oxide has attracted a significant interest due to high yield, opportunity for further functionalization and tunable properties of graphene materials. The reduction of GrO is one of the most frequently reported methods. Several types of reduction agents have been proposed, such as hydrazine [14], vitamin C [51], sodium borohydride [52], sulphur compounds such as: NaHSO_3 , SO_2 , SOCl_2 , $\text{Na}_2\text{S}_2\text{O}_3$, Na_2SO_3 and $\text{Na}_2\text{S} \cdot 9 \text{H}_2\text{O}$ [53, 54]. In addition to the reduction with chemical agents, electrochemical [55, 56], photo chemical [57] and thermal [58, 59] reduction methods have been developed as well.

GrO is a compound of carbon, oxygen, and hydrogen in variable ratios, obtained by processing graphite with strong oxidizers. The maximally oxidized product is a yellow solid with C:O ratio between 2.1 and 2.9, that keeps the layer structure of graphite but with a much wider spacing (6 – 12 Å, depending on the humidity) due to water intercalation. GrO is an electrical insulator, with a conductivity of around $0.5 \text{ S} \cdot \text{m}^{-1}$, due to the strong destruction of the sp^2 carbon network. Due to the oxygen-containing functionalities (hydroxyl, carboxyl, epoxy, etc.) GrO is hydrophilic and readily disperses in water to form stable colloidal suspension. Water is the most common dispersion media for GrO, and there are two different ways to disperse GrO in water including mechanical stirring and sonication. The GrO can also be dispersed in many other solvents such as ethylene glycol, N-methylpyrrolidine, N,N-dimethylformamide, tetrahydrofuran, etc. [55, 60].

Graphite oxide was first prepared long ago by Brodie in 1859 who treated graphitic powder with potassium chlorate in concentrated fuming nitric acid [61]. Later in 1898, Staudenmaier improved the Brodie's synthesis method for GrO by adding the chlorate in multiple aliquots over the course of the reaction rather than in a single addition [62]. After Staudenmaier's approach, two

chemists, Hummers and Offeman developed an alternative method for producing GrO. They prepared GrO by oxidizing graphite with a concentrated sulphuric acid, potassium permanganate and sodium nitrate mixture [63]. Since then, there have been many different variations in the preparation of graphite oxide. Some other oxidizing agents have been used for the formation of GrO, though Jones' reagent ($\text{H}_2\text{CrO}_4/\text{H}_2\text{SO}_4$), concentrated acids (H_2SO_4 , H_2SeO_4 , H_3BO_3 , HNO_3), peroxide and peroxy-compounds (H_2O_2 , $\text{K}_2\text{S}_2\text{O}_8$) [55, 64].

The exact chemical structure of GrO has been debated over the years. Even today there is no definite GrO structure model. There are many reasons for this, but the primary factors are mainly related to the absence of long-range structural order in GrO and to its intrinsic non-stoichiometric atomic composition [55, 65]. The most well-known structural model for GrO was proposed by Lerf and Klinowski, which are presented in Fig. 2. According to this model, GrO layer has two types of regions – oxidized regions and non-oxidized regions. They are randomly distributed and their relative size depends on the degree of oxidation. The oxidized region of GrO is composed by sp^2 -hybridized carbon sheets containing epoxy and hydroxyl groups in the basal planes and carboxyl groups at the plane edges. In the non-oxidized regions the original sp^2 carbon network is preserved [65, 66].

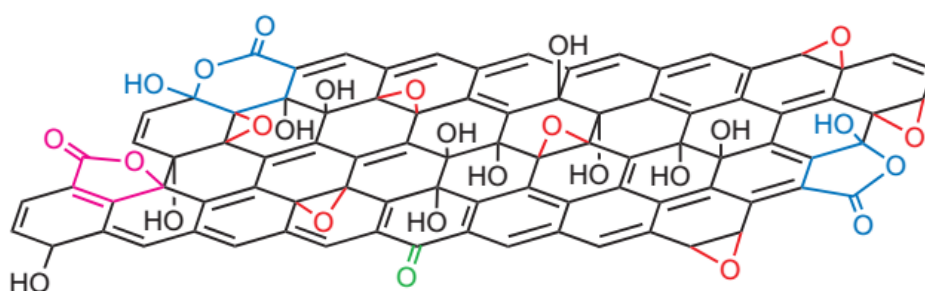


Fig. 2. Lerf and Klinowski's structural model of GrO, taking into account the five- and six-membered lactol rings (blue), ester of a tertiary alcohol (pink), hydroxyl (black), epoxy (red) and ketone (green) functionalities [66].

Carbon nanomaterials have a unique place in nanoscience owing to their exceptional thermal, electrical, chemical and mechanical properties and have

found broad application in areas diverse as composite materials, energy storage and conversion, sensors, drug delivery, field emission devices and nanoscale electronic components. Moreover, recently these materials have been shown to be useful in synthesis and catalysis [37-39].

1.2. Catalysis on carbon nanomaterials

Catalysts play a very important role in the chemical and petroleum industries as they improve reaction yields, reduce temperatures of chemical processes and promote specific selectivity in chemical reactions. [4]. To date, the most widely applied catalytic materials have been concentrated on the noble metals (Pt, Rh, Pd) and metal oxides, hybrid materials or composite structures with the active metallic centres, and organometallic compounds [5-7]. However, some limitations have already emerged for traditional catalysts, such as they are sensitive to poisoning, expensive and harmful for environment. Accordingly, exploiting an alternative cost-effective and stable catalyst is urgently required.

Recently, carbon nanomaterials have been demonstrated as a promising metal-free alternatives for low-cost catalytic processes, because of their wide availability, environmental acceptability, corrosion resistance, and unique surface properties such as large surface area, high thermal stability and various chemical modification potentials [8, 67-69]. Different carbon materials including activated carbon, carbon nanotubes, fullerenes, nanodiamonds, graphene and its derivatives have been used as the effective catalysts or catalyst supports [68, 69].

Today, most of the reactions that are catalyzed by carbon based materials can be classified into one of the following groups: (i) oxidation-reduction; (ii) hydrogenation-dehydrogenation; (iii) combination with halogens; and (iv) decomposition. There are also examples of the catalysis of dehydration, polymerisation, isomerisation, oxygen reduction, esterification and transesterification reactions [8, 70, 71]. In our research we have investigated the oxygen reduction (ORR) and transesterification reactions because of their great technological importance. We also prepared and characterized thermally reduced

graphene oxide (TRGO) based catalysts support for pyrroloquinoline quinone (PQQ)-dependent D-fructose dehydrogenase which possessed the beneficial properties of D-fructose biosensor operating effectively direct electron transfer (DET). This mean that the electron is transferred directly from substrate to the electrode via the active site of the enzyme without any additional mediating compounds. The absence of mediators is the main advantage of such biosensors enhancing the selectivity, proper sensitivity and reducing the cost [72].

1.2.1. Transesterification process for biodiesel production

The world's total energy output is mainly generated from fossil fuels and experts have warned about depletion of this source in the future. Increase of population, industrial and technological developments and huge world's energy demand are the main reasons of the reduction of fossil fuel resources. Moreover, combustion of such fuels generates many harmful products in the form of exhaust gases. Because of these reasons, current research is progressively directed towards examination of alternative renewable fuels. One of the possible solutions of these problems is the gradual replacement of diesel fuel produced from non-renewable sources with biodiesel, which is made from renewable biological sources [73, 74].

Biodiesel, an alternative diesel fuel, is a promising, non-toxic, environmentally friendly and biodegradable fuel defined as a mixture of alkyl (usually methyl) esters of long chain fatty acids (FAME), which are produced from vegetable oils or animal fats and alcohol [75, 76]. FAME combustion products contain lower amounts of particulates, carbon monoxide [76, 77] sulphur oxides, nitrogen oxides, aromatic hydrocarbons and soot particles [78, 79].

There are at least four methods for producing biodiesel, including direct use and blending of raw oils [80], microemulsion [80, 81], thermal cracking or pyrolysis [82, 83], and transesterification [80, 83]. Among all, transesterification of vegetable oils/fats is the easiest and the leading process of biodiesel production on large scale. It is a process of reacting the triglycerides, which are

present in the inedible (e.g. *Jatropha*, *Pongamia*,) or edible vegetable oils (e.g. sunflower, rapeseed, soybean, olive, palm, coconut) or animal fats, with an alcohol (e.g. methanol, ethanol, propanol, butanol, amyl alcohol) in the presence of a catalyst [84-86]. In addition, the process yields glycerol which has potential applications in the pharmaceutical, cosmetic, food and plastics industries [87].

Transesterification consists of a sequence of three consecutive reversible reactions. The reaction mechanism for biodiesel production by the transesterification reaction is presented in Fig. 3. The first step is the conversion of triglycerides to diglycerides, afterward the conversion of diglycerides to monoglycerides, and finally monoglycerides into glycerol, yielding one methyl ester molecule from each glyceride at each step.

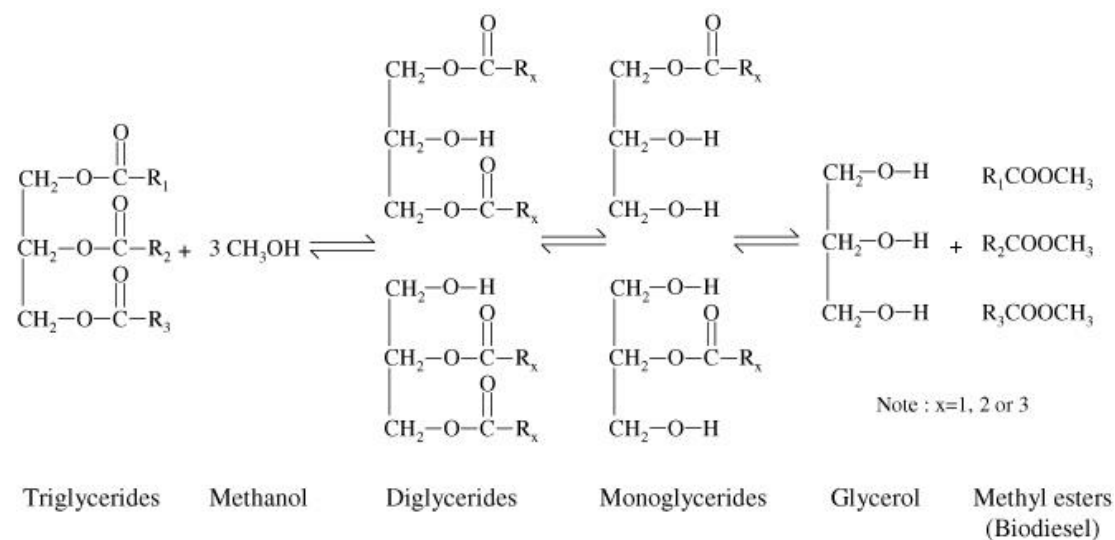


Fig. 3. Reactions in the transesterification of a triglyceride, where $R_1 - R_3$ are the carbon chains of oleic, linoleic, linolenic, palmitic and other fatty acids [88].

The selection of a proper catalyst has a fundamental significance for the sustainable transesterification process. Homogeneous, heterogeneous and enzymatic catalysts have been investigated [75, 89-92]. Currently, homogeneous alkaline catalysts, such as alkaline metal hydroxides, carbonates and alkoxides are most commonly used in industrial transesterification processes for biodiesel production [84, 93]. However, despite the advantages of this method (e.g. high conversion at low temperatures) the use of homogeneous alkaline catalysts

causes some problems. Firstly, these types of catalysts cannot be reused in the process. Secondly, the hydroxides are partly soluble in reaction products, which indicates the need for an additional step of purification [85, 91]. Moreover, for alkali-catalysed transesterification, the feedstock (oil or fat) must contain comparatively low levels of free fatty acids (FFAs) and the alcohol used should be essentially anhydrous, otherwise, the undesirable soap formation and ester hydrolysis may occur. The soap reduces the yield of esters and increases the viscosity, so the separation and purification of esters and glycerol becomes more difficult [94, 95]. In the cases where the raw materials contain high levels of FFAs, acid is usually used to catalyse transesterification process. The typical acid catalysts used in the reaction are sulphuric, phosphoric and hydrochloric acids. The acid-catalysed process is potentially a competitive alternative to the commonly used alkali-catalysed process due to its insensitivity to FFAs in feedstock. Despite this, homogeneous acid catalysts may cause corrosion and environmental problems, and require more expensive equipment [96-99]. The next group of catalysts are enzyme based ones. However, they are disadvantageous because of their high cost and a long reaction time [100, 101].

High energy consumption during transesterification process and costly separation of the homogeneous catalyst from the reaction mixture have encouraged the development of heterogeneous catalysts. Solid catalysts have received considerable attention due to their easy separation for recycling and less corrosive and toxic effects. Moreover, they are much more tolerant to water and FFAs in the feedstock [90-92, 102]. For the last few years, the use of heterogeneous catalysts for the transesterification reaction was extensively studied. The most commonly used for this purpose are metal oxides (e.g. MgO, CaO and SrO) or sulphides, metallic salts (e.g. sodium silicate, vanadyl phosphate, calcium zincate), zeolites, heteropolyacids (e.g. $H_3PW_{12}O_{40}$), hydrotalcites (e.g. $Mg_6Al_2(OH)_{16}CO_3 \cdot 4H_2O$), ion-exchange resins (e.g. Amberlyst-15), basic oxides supported on high-surface-area materials and organic bases (e.g. triethylamine, piperidine, guanidines such as 1,5,7-triazabicyclo[4.4.0]dec-5-ene) [85, 91, 103-106]. Although these solid

catalysts certainly overcome some drawbacks mentioned above, most of them still suffer from disadvantages, such as deactivation, high cost and harmful effects on the environment because of the presence of certain metals [107, 108].

Carbon-based solid acid catalysts have become a hot research area compared to the other solid catalysts because they can promote esterification of FFAs in parallel with transesterification of triglycerides present in oil feedstock without saponification [109]. Consequently, these catalysts enable a reduction of processing steps in biodiesel production, which meets the requirements of green and sustainable chemistry in the catalytic production of biodiesel. Recently, a few of research groups have successfully explored the potential of solid acid carbon-based catalysts in transesterification process.

For example Hara's group prepared a solid Brønsted acid of amorphous carbon bearing $-\text{SO}_3\text{H}$, $-\text{COOH}$, and phenolic $-\text{OH}$ groups using microcrystalline cellulose powder as the starting material and fuming sulphuric acid as the $-\text{SO}_3\text{H}$ source. The as-prepared sulphonated carbon-based material showed high catalytic performance for transesterification of triolein, and its activity outperformed commercial solid acids such as Amberlyst-15 and Nafion NR50. Over a period of 6 h, the yield of methyl oleate reached 24.1% (SO_3H -bearing carbon), 5.0% (Amberlyst-15) and 1.5% (Nafion NR50) [110]. Maneechakr and co-authors have reported that a sulphonated D-glucose derived sugar catalyst showed higher catalytic performance towards transesterification of waste cooking oil with methanol compared with commercial catalysts Amberlyst-15. Moreover, it had excellent operational stability, and after more than ten cycles of successive reuse, it still retained a remarkably high proportion (90.8%) of its original catalytic activity in the FAME formation reaction. Furthermore, this sugar catalyst is very promising to replace H_2SO_4 as a green catalyst for efficient production of biodiesel from higher fatty acids and especially waste oils with a high acid value [111]. Yuan's group have reported that the sulphonated carbon based catalyst, prepared by impregnation of activated carbon with sulphuric acid exhibited remarkably high catalytic activity towards the transesterification of castor oil with methanol at 65°C . Under the same conditions, its catalytic activity

is superior to H_2SO_4 [112]. Ning and co-authors have reported the 97.8% yield of fatty acid ethyl ester from transesterification reaction under the optimum reaction conditions as using sulphonated multi-walled CNTs [113]. More recently, Felpin's group have reported that a sulphonated graphene-based catalyst showed excellent catalytic performance towards transesterification of palm oil with methanol (yield of FAME 98%) [114]. To date, there are few studies on the biodiesel production from transesterification of triglycerides containing feedstocks catalyzed by sulphonated graphene-based catalysts.

The use of carbon based solid acid catalysts for biodiesel production processes is promising, as the carbon materials or their precursors are renewable and the feedstock for the acid catalysts preparation are of low-cost [113, 115]. Although the method to prepare sulphonated carbon catalyst is simple, it is challenging to obtain catalyst with high total acid density and to prevent the active site, such as $-\text{SO}_3\text{H}$, leaching from the structure [115].

1.2.2. Electrocatalysts for oxygen reduction reaction

Oxygen reduction reaction is one of the most important electrocatalytic reaction because of its key role in electrochemical energy conversion (e.g. fuel cells, metal–air batteries, etc.), corrosion, and a few other industrial processes [116]. The ORR mechanism mainly depends on the nature of electrode and electrolyte [117]. It is rather complicated and involves multiple electrochemical reactions. ORR in aqueous solutions occurs mainly by two pathways. One is that O_2 will be reduced directly to H_2O (in acidic media) or OH^- (in alkaline media) via a more efficient four-electron path and the other is that O_2 will be reduced to H_2O_2 (in acidic medium) or HO_2^- (in alkaline media) via a two-electron path, followed by further reduction to H_2O (in acidic media) or OH^- (in alkaline media) [118]. The corresponding reactions are summarized in Table 1. In fuel cell processes, the 4-electron direct pathway is highly preferred [119].

Table 1. Possible pathways for ORR in aqueous media.

ORR pathway	Electrolyte	
	Acidic medium	Alkaline medium
4e ⁻	$O_2 + 4H^+ + 4e^- \rightarrow 2H_2O$ $E_0 = 1.23 V_{SHE}$	$O_2 + 2H_2O + 4e^- \rightarrow 4OH^-$ $E_0 = 0.40 V_{SHE}$
	$O_2 + 2H^+ + 2e^- \rightarrow H_2O_2$ $E_0 = 0.682 V_{SHE}$	$O_2 + H_2O + 2e^- \rightarrow HO_2^- + OH^-$ $E_0 = -0.065 V_{SHE}$
2e ⁻	$H_2O_2 + 2H^+ + 2e^- \rightarrow 2H_2O$ $E_0 = 1.76 V_{SHE}$	$H_2O + HO_2^- + 2e^- \rightarrow 3OH^-$ $E_0 = 0.867 V_{SHE}$

The application of ORR in fuel cells has been the research focus area of material chemists and electrochemists in the past few decades. Fuel cells have gained a great interest for many years due to their high efficiency and environmental friendliness. In a fuel cell, the energy source such as hydrogen, methanol, and formic acid is oxidized at the anode, and the released electrons are transferred to cathode where oxygen is reduced. Generally, the ORR at the cathode has a sluggish reaction kinetics because of its multi-electron characteristic and large overpotential, which limits the cell performance [118, 120]. Therefore, the ORR usually needs to be accelerated by catalysts. Traditionally, platinum has been considered as the best catalyst for fuel cells, although it still suffers from multiple disadvantages, including its high susceptibility to methanol crossover effect, CO poisoning effects and high tendency for particle aggregation. In addition, Pt is too expensive for commercialization in large scale production [117]. Therefore, it is strongly desired to develop cost-effective, metal-free electrocatalytic materials for the replacement of Pt-based fuel cell catalysts.

Heteroatom-doped carbon-based nanostructures, such as carbon nanoparticles [121], CNTs [122] and graphene [123, 124] were regarded as one of the possible alternatives to Pt-based catalysts due to their lower price, greater abundance, and high stability. Among these candidates, heteroatom-doped graphene related materials have attracted considerable interest because of their

outstanding properties, including large surface area, high carrier mobility, excellent mechanical flexibility, and superior chemical stability.

It is reported that the N-doped graphene may have a high electrocatalytic activity towards the ORR [125]. Calculations based on hybrid density functional theory suggest that this effect is likely attributable to the strong electron affinity of N atoms and substantially high positive charge density on the adjacent C atoms resulting in very favorable adsorption of O₂ [125]. This parallel diatomic adsorption may effectively weaken the bonding in oxygen molecule and facilitate the direct reduction of oxygen [122]. Doped N atoms in graphene may be assigned to pyrrolic, pyridinic and quaternary (graphitic) [125]. The content of different nitrogen types usually varies with nitrogen doping level. It is worth noting that a higher amount of N incorporated in the graphene layer does not always lead to better ORR performance. Moreover, not only substitutionally N-doped graphene derivatives show the ORR activity but also the composite materials with adsorbed nitrogen-containing structures have the same effect. For example, the ORR activity of composite materials made of graphene and polyaniline/polypyrrole is reported several times [126]. This composite catalyst is active in acidic media, while in most cases the N-doped graphenes show their ORR activity in alkaline media.

Recently, research involving the electrocatalytic activities of carbon materials doped with other low (e.g. B, P) or similarly (e.g. S, Se) electronegative atoms have attracted increasing attention [127]. The reported results suggest that the operational activity and stability of such catalysts are better when compared with the performance of single N-doped graphenes. Many authors emphasize that the mechanism of such effects is still unclear [125].

The sulphur doped graphenes (S-graphenes) can exhibit the excellent catalytic activity and long-term stability for ORR [128]. It was found that the graphenes doped with other elements of similar electronegativity (e.g. Se) show similarly high ORR catalytic activity [129]. A vital role for the high ORR activity of S-graphene may play the unique electron structure derived from the conjugation between the sulphur lone-pair electrons and the graphene π system

[125]. In this case tailoring the π electronic system of graphene may be a crucial factor for the producing of considerably improved materials for ORR. These types of doped structures may provide enhanced opportunities for further developing of high-active and poison-resistant electrocatalysts with long lifetimes.

In addition to single-atom doped graphene materials and their ORR activity it is possible to find information about the multi-doping with several atoms. The multi-doping strategy is acknowledged as an effective tool for the enhanced ORR activity. The dual-doped carbon catalysts showed the highest onset potential and electrochemical activity in acidic media, about 43% of that of commercial Pt/C (40 wt%) [130]. It was concluded that the co-presence of sulphur and nitrogen is likely to increase the ORR activity of the graphene material in both basic and acidic media [131]. This study of the synergistic effect of combined sulphur- and nitrogen-doping in catalysis of the ORR is expected to be significant to future research in improvement of heterogeneous, metal-free, carbon-based catalysts. Feng and co-authors reported the preparation of efficient metal-free electrocatalyst for ORR by using a thiocyanate precursor and GO by a hydrothermal procedure [132]. This N- and S- co-doped catalyst was active in alkaline solution. Presented report demonstrate that the preparation conditions are crucial for this type of electrocatalyst; its operation can be improved by optimizing the synthesis conditions.

Despite the recent progress, the metal-free carbon catalysts currently are still far from that desired for practical applications. The need of much additional research is emphasized to produce commercially valid material with high activity and practical durability for ORR.

1.2.3. Carbon materials as catalyst supports

A key issue in catalysis is to obtain high surface area catalysts in order to improve catalytic activity and selectivity [133]. This is achieved by using a catalyst support, which is the basic function is to provide good electrical conductivity with high surface area, also bring the catalyst particles close to the

reactants via the pore structure and provide a corrosion stability under oxidizing conditions [134]. However, it is well known that the role of the support is not simply that of a carrier, the interaction between the catalytic phase and the support can affect the activity [135]. Because of these reasons the choice of the right support material is vital in the industrial process development. The selection of the support is based on a series of desirable characteristics such as inertness, stability under reaction and regeneration conditions, suitable mechanical properties, large surface area, porosity and chemical nature [8]. According to the literature, the catalyst support can be materials such as alumina, zeolites and metal oxides of the transition metals (TiO_2 , La_2O_3 , CeO_2 and ZrO_2 etc.), which are among the most commonly used heterogeneous catalyst carriers [136, 137]. The challenge related to the use of the above supports is that they are not easy to eliminate from the products at the end of the reaction due to their high degree of insolubility. To overcome this drawback, a new prospective materials have been developed.

For almost twenty years there has been an increasing interest in the use of nanostructured carbon materials as catalyst supports [68, 136]. Following the nanotechnology revolution, a wide variety of carbon nanomaterials has been investigated as catalyst carriers, including fullerenes [138], CNTs [139], carbon nanofibers [140], carbon onions [8], nanodiamonds [141], graphene or GO [136]. Carbon materials have some characteristics that are very valuable for their application as catalysts supports, some of them not attainable with any other materials. The main advantages offered by carbon based supports are:

- (i) Carbon nanomaterials have a high surface area and its porous framework can be modified to obtain the pore size distribution optimum for each particular reaction. High surface area and a well-developed porosity are very important for achieving a high dispersion (e.g. fraction of metal atoms that are on the surface of the support in relation to the total metal loading) of the active phase in the catalyst. However, in some cases, a high surface area of the carbon support may be harmful if it is limited in narrow micropores that are not accessible to the reactant molecules. This is

especially important in processes where large molecules are involved, as in the treatment of petroleum feedstocks and in liquid-phase reactions in which diffusion of reactants and/or products may be hindered by the narrow porosity [8, 142].

- (ii) Carbon surface is relatively inert. Their surface is resistant to both acidic and basic media [143].
- (iii) The mesoporous nature of these supports can be of interest for liquid-phase reactions, thus limiting the mass transfer [8];
- (iv) Carbon supports are usually cheaper than other commercial supports, such as alumina and silica [142].
- (v) Carbon materials may be obtained in different forms (granules, pellets, fibers, foams, monoliths, fabrics, coatings, etc.) [142].
- (vi) The active phase, usually expensive, can be easily recovered by burning away the carbon support [142].
- (vii) Although carbon is usually a material with a hydrophobic nature, the chemical nature of their surface can be easily chemically modified to give them some hydrophilicity that offers numerous perspectives for adsorption and dispersion of the active phase. The surface chemistry of carbon materials is a key property that allows designing the interactions between the support and the active species [143].

Nevertheless, carbon supports also have some limitations: they can be easily gasified, which makes them difficult to use in high temperature oxidation and hydrogenation reactions, and their reproducibility can be poor, especially activated carbon-based catalysts, since different groups of the same material can contain unpredictable ash amounts [8].

The methods used for the preparation of carbon-supported catalysts are similar to those used with other supports. In the literature many preparation recipes have been proposed including, chemical vapor deposition [144], precipitation or co-precipitation method [145], the liquid phase reduction [146] and the most common used impregnation method [136].

Carbon-based materials are still the most practical for the preparation of noble metal catalysts, particularly for Pd, Pt, Ir, Co based catalyst. Also carbon based support materials have been widely used in the bi-functional catalyst system, including MnO_2 nanowires, MnFe_2O_4 , Co_3O_4 , CuFe_2O_4 , NiFe_2O_4 , $\text{Fe}_2\text{O}_3 \cdot \text{Co}(\text{OH})_2$ and CoFe_2O_4 or in bimetallic catalyst systems such as Pt-Au, Pd-Ag, Pt-Ru, etc. [123, 136] The use of nanocarbon materials to create bioelectrodes for biosensing applications by supporting enzymes and/or micro-organisms is another emerging area of development [147, 148].

Electrochemical biosensors are currently extensively exploited in sectors as diverse as medicine, environmental monitoring, industries and domestic use. Electrochemical detection has a large potential for development of portable instrumentation suitable for analysis in many fields. Due to the high demand of the world market, the number of biosensors suitable for commercial use is increasing regularly. Nevertheless, there is a range of problems hindering the widespread use of biosensors, and most of them are related to the design of a biosensor [149].

An electrochemical biosensor is defined as a device that transforms biochemical information into an analytically useful electrochemical signal. It is essentially comprised of the immobilization of a biomolecular recognition element e.g. microorganisms, organelles, cell receptors, enzymes, antibodies, nucleic acids, etc. (bioreceptor) onto the corresponding transducer, the system that converts the biochemical response into an electrical signal. A biosensor is composed of these two parts, which constitute a working electrode. In the design of a biosensor the general aim is to enable quick and convenient testing, i. e., to get reliable and strong analytical signal. This aim can be reached by a proper selection of bioreceptor and support/transducer system, simultaneously taking into account their mutual interaction [134, 150].

In recent years achievements in the field of nanotechnology have made a significant impact on the biosensor design. Various configurations of biosensors, wherein nanomaterials such as gold nanoparticles, magnetic nanoparticles, and the like serve as electrode material have been reported so far [151]. The use of

nanomaterials allows expect a substantial improvement in a biosensor quality, including accuracy, reproducibility, detection limits, exploitation time, and reliability. The dimensions of nanoparticles lay in the same range or even smaller than these of enzymes, therefore, many of nanomaterials can serve as excellent supports for the enzyme immobilization. The combination of surface chemistry of nanomaterials and proper enzyme orientation control holds a great potential for outstanding biosensors. The site-selective immobilization of enzyme is a promising strategy for stable, efficient, and oriented protein attachment with low nonspecific adsorption [152]. Based on this strategy, implantable biosensors were prepared by exploiting the unique properties of nanomaterials [151].

The use of carbon nanomaterials for biosensors in the form of quantum dots (Qds), CNTs, graphene, graphene oxide, and the like is reported so far [153]. Single- and multiwalled CNTs were utilized as support/transducer systems of various biosensors having aim to make use of their nanoscale dimensions, electrocatalytic properties, and high surface area. Among the most significant advantages promoting the use of CNTs (especially, SWCNTs) in biosensors are their small diameter-to-length ratio, which allocates a close contact between the enzyme and electroconductive CNT [154]. There CNTs can be active mediators, which promote a direct electron transfer from enzyme active sites. The biosensor nanoelectrode arrays made of CNTs are reported for various substrates [155]. The immobilization of enzyme on CNTs is a key technology, which allows benefit the advantages of a CNT use. Non-covalent immobilization has been studied more intensively in comparison with the covalent methods due to its less destructive influence on enzyme's structure and uncomplicated operation. During the covalent immobilization, specific functional groups are attached to the ends or side-walls of CNTs [156]. However, there is not a universal enzyme support and the best method of immobilization might differ from enzyme to enzyme, from application to application, and from carrier to carrier. A definite number of problems related to the preparation and use of CNT in biosensors still remain.

More recently, graphene and its related materials have attracted much interest in sensing applications. It can be considered as a competitor to CNTs, while it exhibits excellent performance in direct electrochemistry of enzymes [157]. Currently the efforts in graphene technology are focused both in the reproducible synthesis of large quantities of uniform high-quality graphene and in tailoring of on-demand graphene properties. As in the case of CNTs, much emphasis is put on the better understanding of processes that occur on the interface of graphene and biomolecule (e.g., the mechanisms of absorption molecules on graphene surface, the orientation of biomolecules on the graphene, and how these interactions impact the transport properties of graphene). Graphene-based composites with other organic or inorganic materials (including electroconductive polymers and CNTs) considerably extend the possibilities of biosensor development [16].

Graphene oxide may also be an ideal substrate for biomolecules immobilization. GO is enriched with oxygen-containing groups, making it possible to immobilize active phase through electrostatic interaction without surface modification or coupling reagents [142]. While GO particles are well-known for their biomolecules immobilization abilities, few reports are available regarding the immobilization of active phase on reduced GO [158]. Both GO and rGO can serve as an excellent immobilization platform for enzymes, proteins and DNA used in biosensors. Through the interactions of GO and rGO with enzymes, proteins, or short-chain peptides, more complicated supramolecular architectures were assembled. Some of the as-obtained conjugates showed unique biological and chemical properties that were found applicable as bioprobes and biosensors [15]. Among the issues to be resolved working with GO and rGO application in biosensors several problems should be mentioned. One of them is the detailed characterization of these materials, especially the distribution of oxygen-containing groups, which is crucial for the interaction with enzyme molecules. The problem remains how to synthesize the individual graphene sheets of controllable size and quality. Control of

conductivity, number of layers, and shape is also important in application of these materials in biosensors [16].

Graphene, GO, rGO and CNTs are the most widely used carbon nanomaterials in biosensors. The use of each in this group of materials has their own advantages and limitations, which are related to their properties and structural characteristics [155]. In comparison with CNTs, graphene exhibits potential advantages of low cost and higher purity from heavy metals in the case, when it is produced using GO as a precursor. Nevertheless, the cost of epitaxially grown graphene is comparable to that or even higher as CNTs. The defect-free graphene possess excellent electrical conductivity, which significantly decreases in the case of rGO, or especially, GO. On the other hand, graphene suffers from the lack of the functional groups on the surface hindering the immobilization of enzymes. The surface of CNTs is more active, both at the sidewalls and, especially, at the tips. GO and rGO are useful platforms for the enzyme immobilization, but the procedure of immobilization should be controlled carefully trying retain the maximal enzyme activity [155, 157]. In summary, the preparation of a biosensor is still a very complex and difficult task, where a number of technical and scientific problems should be resolved. Among these one of the most important is the preparation of a suitable electroconductive coating for electrochemical biosensor, which would meet the high-standard requirements for analysis in health care. Working in this field, the opportunities of carbon nanomaterials are not completely exploited yet so far.

1.3. Graphene-based coatings: preparation and transfer

Owing to their unique physical, chemical, and mechanical properties, carbon nanomaterials such as fullerenes, CNTs and graphene are among the most important and widely used materials in many areas such as chemistry (catalyst support, absorbent), electrochemistry (electrodes), bioengineering (biocompatible implants, biosensors), mechanical engineering, tribology (solid lubricant), electronics (substrates) and in many other fields. In some of these

applications, carbon coatings are as important as bulk materials, and sometimes only thin coatings can be used [159-161].

During the last ten years, graphene and its coatings have gained increasing research interest due to their high electrical conductivity and mechanical flexibility. Graphene films are regarded as one of the most promising candidates that could be used for biosensors electrode, stretchable electronic and optoelectronic devices [162-164]. Many methods have been reported for the fabrication of graphene thin films, including epitaxial growth on SiC wafer under ultrahigh vacuum conditions [165] or chemical vapor deposition (CVD) of hydrocarbon precursors onto transition metal substrates, such as Cu, Ni, Ir, Co, Pt, Ru, etc. [166]. The graphene coatings fabricated by using GO suspension can avoid the use of expensive catalytic surfaces and can be operated under mild conditions. The general procedure for preparing graphene films from GO suspension involves the deposition of GO films followed by reduction. GO nanosheets can be deposited on various substrates by using solution-based techniques, such as dip coating [167], spin coating [168], vacuum filtration [169], layer by layer self-assembling (LBL) [170], Langmuir-Blodgett (LB) [171], spray coating [172], electrophoretic deposition (EPD) [173]. Among the different techniques to obtain graphene coatings, CVD method on a metal substrate presents the best trade-off between material quality and industrial scalability. However, for most applications a transparent or insulating substrate is needed. Therefore, the graphene layer requires to be transferred from the metal to the arbitrary substrate. Graphene is transferred on many substrates such as polymers (polyethylene terephthalate) (PET), polystyrene (PS), polyimide (PI) [174-176], boron nitride [177], InAs/GaAs [178]. Graphene can likewise be transferred on structured substrate such as holey transmission electron microscopy grids [179] or perforated substrate [180]. For this purpose, several procedures have been developed.

To date, the most common method for transferring graphene from a transition metal or SiO₂ growth substrate is the polymer supported transfer method [181]. A schematic diagram of the transfer process is shown in Fig. 4.

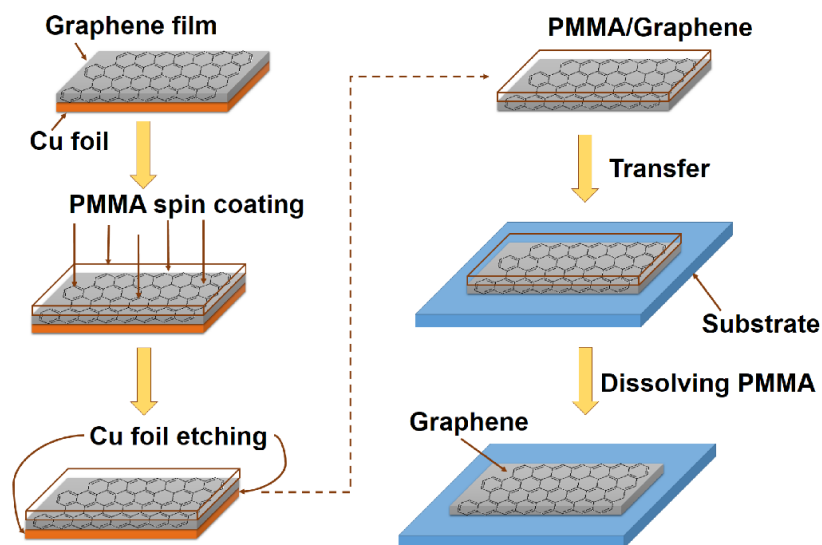


Fig. 4. Schematic illustration of the transfer process of graphene onto transparent substrate [181].

According to this method, a layer of poly(methyl-methacrylate) (PMMA) is coated onto the graphene/metal surface. Afterward, the metal is chemically etched away and the PMMA/graphene membrane is transferred onto the target substrate. Finally, the PMMA is removed either via dissolving in acetone (or acetone vapor) or high-temperature annealing ($\sim 350 - 500$ °C) [181]. This transfer technique is powerful for graphene growth by CVD on a metallic substrate, such as Cu or Ni, which can be easily removed [182]. Different etching agents are used in relationship with the nature of the substrate. For copper foil, various compounds are employed such as ammonium persulphate, ammonium sulphate, iron (III) chloride, iron (III) nitrate, H_2O_2 (3%)/HCl (35%) mixture, Marble's reagent ($\text{CuSO}_4/\text{HCl}/\text{H}_2\text{O}$: 10g/50mL/50mL). For etching of nickel foil, hydrogen fluoride solution, hydrochloric acid are used as etchants. To etch silicon oxide layer, sodium hydroxide (1 M - 90°C) and potassium hydroxide could be used [182]. In addition, besides using PMMA as the polymer supporting layer, poly(bisphenol A carbonate), polyisobutylene (PIB), Polydimethylsiloxane (PDMS) can be used in the transfer method [175, 182]. Lots of polymers are proposed but PMMA is the most commonly used polymer supporting layer. However, PMMA-based technique has some disadvantages,

such as PMMA often was not fully washed away with acetone and remained as a residue, also most flexible substrates either dissolve in acetone or cannot withstand the annealing temperature [181, 183]. Other PMMA-free techniques have been investigated, including using thermal release tape as the transfer membrane or using particular functional groups to attach graphene to other flexible substrates [182].

Recently, a transfer method by electrochemical bubbling was proposed. A schematic diagram of the transfer process is shown in Fig. 5. According to this method, the hydrogen bubbles are formed and squeezed into the graphene/substrate interface to mechanically delaminate the graphene/polymer from the substrate. Afterwards, the film is placed onto the arbitrary substrate and the polymer is dissolved. The electrochemical bubbling is a strong candidate for the transfer technique in graphene industry. Nevertheless, it is not yet widely applied. One of the main reasons is that the graphene after transfer often shows some wrinkles and holes. In comparison, the metal etching based transfer usually results in less damage [175, 184].

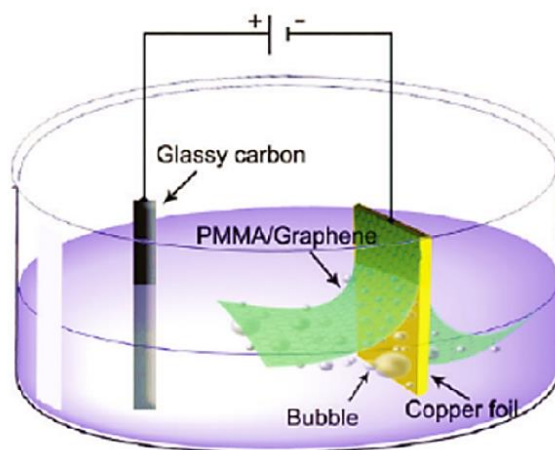


Fig. 5. Schematic diagram of the electrochemical transfer of graphene from a metal substrate using an electrochemical bubbling method [175].

The graphene layer also can be transferred by direct pressure between graphene and a arbitrary substrate. Actually, it is possible to find in the literature transfer techniques such as roll-to-roll method or hot press lamination method

[175, 185]. Moreover, above mention techniques could be used together in order to improve the quality or the ability of the graphene transfer.

Each technique has its own merits and limitations. The transfer of prepared graphene coatings from one substrate to another becomes an urgent problem, since it improves the processability and extends the potential application areas of coatings. However, this problem is seldom discussed in the literature [186]. To avoid undesirable changes in the structure during the transfer procedure, it is necessary to solve the multi-objective optimization problems. The procedure includes a suitable choice of testing and sample preparation methods [187]. The use of combinatorial approach for the sample preparation and testing is becoming increasingly accepted in the field of materials science. Among the other advantages of using the combinatorial method, opportunity to determine the structure–property relationships should be mentioned [188].

2. EXPERIMENTAL

2.1. Materials and reagents

Graphite used for the synthesis was of extra pure grade (Merck). The particle size of the pristine graphite (according to manufacturer's data) was $\geq 50.0 \mu\text{m}$ (99.5%). Graphite rod (\varnothing 3 mm, Sigma-Aldrich) was used for the preparation of working electrodes. The commercially available rapeseed oil "Olej Wyborny Rzepakowy" (Poland) was used for transesterification process. Deionised water was used for solutions preparations and washing. All reagents and materials were of analytical grade or high purity, and unless otherwise stated were used as received. Sulphuric acid (H_2SO_4 , $\geq 98\%$, Eurochemicals), potassium persulphate ($\text{K}_2\text{S}_2\text{O}_8$, 99.99%, Sigma-Aldrich), phosphorus pentoxide (P_2O_5 , $\geq 99\%$ purity, Carl Roth), sodium nitrate (NaNO_3 , p.a., Chempur), hydrochloric acid (HCl , p.a., Eurochemicals), potassium permanganate (KMnO_4 , $\geq 99\%$ purity, Sigma-Aldrich), hydrogen peroxide (H_2O_2 , 30%, p.a. POCH), 4-aminobenzenesulphonic acid (BDS, 4-(H_2N) $\text{C}_6\text{H}_4\text{SO}_3\text{H}$, ACS reagent, 99%, Sigma-Aldrich), sodium nitrite (NaNO_2 , p.a. PubChem), methanol (CH_3OH , anhydrous, 99.8%, PubChem), sodium hydroxide (NaOH , p.a. PENTA), potassium hydroxide (KOH , p.a., Chempur), N,N-dimethylformamide (DMF, $\geq 99\%$, Chempur), acetone ($(\text{CH}_3)_2\text{CO}$, p.a., Eurochemicals), phosphoric acid (H_3PO_4 , 85%, Lach-Ner), melamine ($\text{C}_3\text{N}_3(\text{NH}_2)_3$, $\geq 99\%$, PubChem), potassium thiocyanate (KSCN , $\geq 99\%$, PubChem), ammonium persulphate ($(\text{NH}_4)_2\text{S}_2\text{O}_8$, p.a. Lach-Ner), lead(II) thiocyanate ($\text{Pb}(\text{SCN})_2$, 99.5%, Sigma-Aldrich), ammonium thiocyanate ($(\text{NH}_4)\text{SCN}$, p.a. Reachem), dichloromethane (CH_2Cl_2 , anhydrous, $\geq 99.8\%$, Sigma-Aldrich), bromine (Br_2 , $\geq 99\%$, Reachem), tetrahydrofuran ($\text{C}_4\text{H}_8\text{O}$, anhydrous, $\geq 99.9\%$, Sigma-Aldrich), magnesium sulphate (MgSO_4 , anhydrous, $\geq 99.99\%$, Sigma-aldrich), n-heptane (C_7H_{16} , 99%, PubChem), methyl heptadecanoate ($\text{CH}_3(\text{CH}_2)_{15}\text{COOCH}_3$, analytical standard, $\geq 99.0\%$ (GC), Sigma-Aldrich), ethanol ($\text{CH}_3\text{CH}_2\text{OH}$, 96%, Vilniaus degtinė), Nafion® perfluorinated resin (aqueous dispersion, 10 wt. % in H_2O , Sigma-Aldrich),

potassium bromide (KBr, optical grade, $\geq 99.9\%$, Sigma-Aldrich), polyethylenimine (PEI; branched, $\leq 1\%$ water, Sigma-Aldrich), poly(vinyl alcohol) (PVA; 99+% hydrolysed, Sigma-Aldrich), poly(ethylene oxide) (PEO; Sigma Aldrich), adipic acid ($\text{HOOC}(\text{CH}_2)_4\text{COOH}$, 99%, Fluka), polyvinylpyrrolidone (PVP, extra pure, Carl Roth), sodium dodecyl sulphate (SDS, anal. grade, Reachem), 2-hydroxyethyl cellulose (HEC, Sigma Aldrich), Nadir® - dialysis tubing cellulose hydrate (Carl Roth), polycarbonate membrane filter (PC, pore size 0.45 μm , Carl Roth). The gases (Ar, N₂, He, H₂, NH₃) were supplied by Elme Messer Lit. ($>99\%$ purity).

2.2. Synthesis methods

2.2.1. Synthesis of graphite oxide

GrO was synthesized from the natural graphite by synthesis protocol reported by Yan et al. [189]. In a typical synthesis, graphite powder (6.0 g) was put into an 80 °C solution of concentrated H₂SO₄ (24.0 mL), K₂S₂O₈ (5.0 g), and P₂O₅ (5.0 g). The mixture was kept at 80 °C for 4.5 h using a hot plate. Successively, the mixture was cooled to room temperature and diluted with 0.5 L of H₂O and left overnight. The mixture was then filtered and washed with H₂O to remove the residual acid. The product was dried under ambient condition. Then, this pre-oxidized graphite was subjected to oxidation by Hummers method [63] described as follows.

Pre-treated graphite powder was put into cold (3 °C) concentrated H₂SO₄ (240.0 mL) and NaNO₃ (3.0 g) mixture. Then, KMnO₄ (30.0 g) was added gradually under stirring and the temperature of the mixture was kept to be below 20 °C by cooling. Afterward the resulting mixture was left at room temperature for 3 days. Successively, the mixture was stirred at 35 °C for 1 h, and then carefully diluted with 276.0 mL of H₂O. After that, the mixture was stirred at 70 °C temperature for 15 min, and an additional 840.0 mL of H₂O was then added. Shortly, 20.0 mL of 30% H₂O₂ was added to the mixture. The resulting brilliant-yellow mixture was filtered and washed with 10 wt% HCl aqueous

solution (1.0 L) to remove metal ions. Afterwards the GO particles were washed several times with distilled water by centrifugation (ultracentrifuge SIGMA 1-6P) at 5500 rpm (each run for 20 min). The mixture was transferred into a dialysis tubing cellulose membrane with a cutoff molecular weight (MWCO) of 10000 – 20000 Da and dialyzed against distilled water until the dialysate was free of sulphate and exhibited a pH 6. The suspension was filtered using a Buchner funnel and obtained brown powder was dried in a vacuum desiccator to a constant weight.

2.2.2. Thermal reduction of graphite oxide

Thermal reduction of GrO and fractionation of obtained TRGO was performed using the equipment shown in Fig. 6.

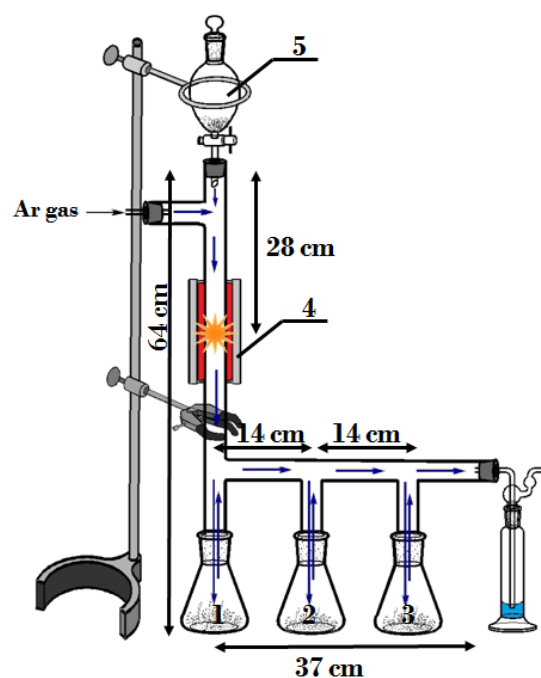


Fig. 6. Equipment used for the thermal reduction of GrO. 1-chamber for TRGO1, 2-chamber for TRGO2, 3-chamber for TRGO3, 4- eating zone, and 5-separatory funnel for GrO.

1.0 g of dry GrO powder crushed in an agate mortar has been added to the separator funnel (Fig. 6; 5) and sealed. Ar gas was passed through the system

during 1 h; Ar flow rate was maintained at $60.0 \text{ ml} \cdot \text{min}^{-1}$. After 1 h the furnace (Fig. 6; 4) was heated up to $800 \text{ }^\circ\text{C}$ and GrO powder from the sealed separator funnel has been subjected to the hot zone in small portions ($\sim 0.05 \text{ g}$). During this part of the experiment the Ar flow rate was maintained at $100.0 \text{ ml} \cdot \text{min}^{-1}$. According to Schniepp et al. [190] and McAllister et al. [191] the thermal reduction of GrO resulted removing of oxygen-containing functional groups, thereby forming carbonaceous (CO and/or CO_2) species. High pressure (130 MPa) arising between the graphene layers destroys the layered structure, influences the structural changes and formation of vacancies and topological defects. Obtained thermally reduced GO particles are moved away from the hot reaction zone by the Ar flow and settle in subsequent chambers (Fig. 6; 1, 2 and 3) depending on the charge and mass. Collected fractions of TRGO are labeled as TRGO1, TRGO2 and TRGO3 respectively. The mass ratio of TRGO1:TRGO2:TRGO3 in the experiment was obtained as 0.428:0.019:0.004 respectively.

The same technique was used to prepare TRGO, which was modified with different agents in order to introduce acidic or basic functional groups on its surface.

2.2.3. Synthesis of catalytically active materials for transesterification reaction

Functionalization of TRGO with concentrated sulphuric acid.

The treatment with sulphuric acid was performed as follows [192]: TRGO (3.0 g) and concentrated H_2SO_4 ($95 \text{ wt}\%$, 140.0 mL) were put in a three-neck round-bottom flask. The mixture was heated at $140 \text{ }^\circ\text{C}$ for 5 h or 20 h , under argon flow rate of $30.0 \text{ mL} \cdot \text{min}^{-1}$, with continuous stirring. Then the suspension was cooled to room temperature and the obtained catalyst sample was washed with hot distilled water ($60 \text{ }^\circ\text{C}$), dried overnight at $110 \text{ }^\circ\text{C}$ and sieved to a uniform size range of $\leq 0.4 \text{ mm}$. The modified carbons were denoted as C_SA_5, C_SA_20, respectively.

Functionalization of TRGO with 4-aminobenzenesulphonic acid.

In order to introduce sulphonic groups on the TRGO surface via *in situ* generated diazonium cation, the method proposed by Toupin and Bélanger was applied [193]. Briefly, TRGO (2.0 g) was dispersed in distilled water (100 mL), then an equimolar amount of 4-aminobenzenesulphonic acid (2.87 g) and sodium nitrite (1.15 g) was added and finally concentrated hydrochloric acid (20 mL) was added dropwise. The reaction was carried out at ambient temperature for 20 h under continuous stirring. Prepared catalyst was washed with distilled water, methanol, DMF and acetone. The sample was dried overnight at 110 °C and sieved to a uniform size range of ≤ 0.4 mm. The modified carbon was denoted as C_BDS.

Functionalization of TRGO with phosphoric acid

The modification of TRGO with H₃PO₄ was performed according to the protocol reported by Puziy et al. [194]. Initial TRGO (2.5 g) was impregnated with phosphoric acid (7.0%, 53.8 g) at ambient temperature for 4 h under mechanical stirring. After this time the mixture was dried overnight at 190 °C. Then, the impregnated carbon was subjected to heat treatment at 800 °C for 30 min under nitrogen flow rate 830 mL · min⁻¹. To remove any remaining phosphoric acid, the sample was extensively washed with hot distilled water until filtrate attained a neutral pH value. Next, the catalyst was dried overnight at 110 °C and sieved to a uniform size range of ≤ 0.4 mm. The modified carbon was denoted as C_PA.

Functionalization of TRGO with gaseous ammonia

To introduce basic sites TRGO was treated with gaseous ammonia at different temperatures in a vertical tube furnace [195]. Around 3.0 g of TRGO was placed in a quartz reactor and introduced into the tubular furnace. Then sample was held under a flow rate of 100 mL · min⁻¹ of Ar for 20 min to remove oxygen residue completely. Afterwards the furnace was switch on (heat rate 10 °C · min⁻¹). When the furnace reached the desired temperature 850 °C or

950 °C the gas flow was switched from Ar to NH₃ (100 mL · min⁻¹) and then held for 4 h or 8 h. After the reaction time, the furnace was cooled to 600 °C under a flow of ammonia. Finally the quartz reactor was removed from the furnace and cooled quickly down to room temperature under Ar gas. Prepared catalysts were sieved to a uniform size range of ≤ 0.4 mm. The modified carbons were denoted as C_Am_4_850, C_Am_8_850, C_Am_4_950, C_Am_8_950, respectively.

Functionalization of TRGO with melamine

The modification of TRGO with melamine was performed according to the protocol reported by Ouyang et al. [196]. Detailed procedure as follows, 2.0 g of TRGO powder and 10.0 g of melamine in 100 mL of distilled water were mixed together about 4 h under ambient conditions. Then mixture was dried at 60 °C temperature, and placed in a quartz boat, which was placed at the center of the horizontal tube furnace. Before the furnace was heated to 700 °C nitrogen gas was flowed for about 20 min. When the center of the furnace reached the designed reaction temperature the mixture was annealed for 1 h at this temperature. Then the boat was shifted to the cold part of the quartz tube, and held there till room temperature was reached. The reaction was carried out in an N₂ flow of 50 L · min⁻¹. The modified carbon was denoted as C_Me_1_700.

2.2.4. Synthesis of catalytically active materials for oxygen reduction reaction

Novel graphene-based nanocomposite containing polythiocyanogen ((SCN)_n) was prepared in order to fabricate superior metal-free catalyst for oxygen reduction. Although (SCN)_n has been known for a long time, its solid state structure continues to be uncertain and controversial yet. Structures of (SCN)_n proposed by various investigators are presented in Fig. 7.

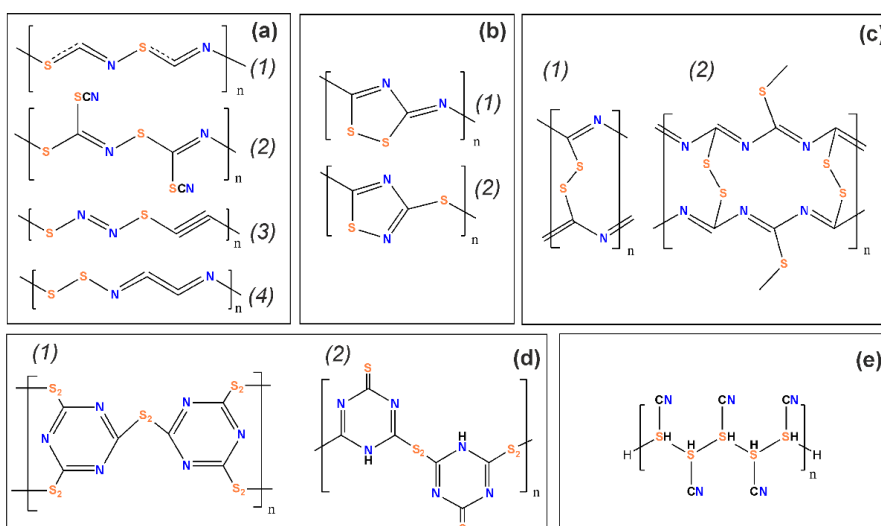


Fig. 7. Structures of $(\text{SCN})_n$: (a) – linear, (b) - containing thiazole rings, (c) - polyazomethine chains, (d) -triazine rings, and (e) - sulphur(IV) chains [197-200].

Methods used for the synthesis of polythiocyanogen and designation of products are presented in Table 2. The reaction time (in minutes) where necessary is marked next to the designation of the product (e.g., SS/A-10 means that the solid-solid reaction between KSCN and $(\text{NH}_4)_2\text{S}_2\text{O}_8$ was performed for 10 minutes).

Table 2. Methods used for the synthesis of $(\text{SCN})_n$

Precursors	Reaction	Reference	Product
KSCN + $(\text{NH}_4)_2\text{S}_2\text{O}_8$	Solid-solid	[198]	SS/A
KSCN + GrO	Solid-solid	-	SS/G
$(\text{NH}_4)\text{SCN}$ + $(\text{NH}_4)_2\text{S}_2\text{O}_8$	Aqueous solution	[201]	AS/A
$(\text{NH}_4)\text{SCN}$ + GrO	Aqueous solution	-	AS/G
$(\text{SCN})_2$	Thermal polymerization	[197]	TP

Synthesis of polythiocyanogen by mechanochemical process

The solvent-free, solid-solid reaction between peroxydisulphate and thiocyanate was applied for this purpose [198]. The mixture of KSCN and

$(\text{NH}_4)_2\text{S}_2\text{O}_8$ in a mole ratio (2:1) was grinded in an agate mortar with a pestle at room temperature from 10 to 90 minutes. Polythiocyanogen is insoluble in water. Therefore, to purify the $(\text{SCN})_n$, crude product (SS/A) was washed with water until substantially free from thiocyanate, peroxydisulfate and sulfate ions. The product is isolated by filtrating and is dried at room temperature in desiccators. Considering the strong oxidizing properties of GrO [202], a similar procedure for the preparation of $(\text{SCN})_n$ from KSCN, using GrO as radical initiator, was carried out to obtain SS/G products.

Synthesis of polythiocyanogen in aqueous solution

$(\text{SCN})_n$ was prepared by synthesis protocol reported by S. A. Kahani [201]. A solution of ammonium thiocyanate (9.7 g, 0.1 mol) in distilled water (50.0 mL) was stirred at room temperature, while ammonium peroxydisulfate (13.5 g, 0.05 mol) in distilled water (50.0 mL) was added dropwise. The resultant mixture was stirred for a 1 h at room temperature. The product was found to be pale yellow, which upon completion of the reaction became a yellow precipitate. To purify $(\text{SCN})_n$, crude product (AS/A) was washed with water until substantially free from thiocyanate, peroxydisulfate and sulfate ions respectively. The product was filtrated and dried at room temperature in desiccators. A similar procedure for the preparation of $(\text{SCN})_n$ from NH_4SCN using a GrO oxidant was carried out (AS/G product).

Synthesis of polythiocyanogen by thermal polymerization of thiocyanogen

$(\text{SCN})_n$ was prepared by thermal polymerization of thiocyanogen $(\text{SCN})_2$ (TP product) by synthesis protocol reported by F. Cataldo [197]. Thiocyanogen, unstable at room temperature, was synthesized by a displacement reaction between $\text{Pb}(\text{SCN})_2$ and Br_2 .

$\text{Pb}(\text{SCN})_2$ (5.0 g) was suspended in 35.5 mL of dichloromethane with vigorous stirring and the flask was put into an ice/water bath. Then a solution of 0.74 mL of bromine in 59.3 mL of dichloromethane was added slowly and dropwise. When the addition was complete, the mixture was stirred for 1 h and

the color of free bromine completely disappeared. The PbBr_2 which formed was separated from the thiocyanogen solution by decantation and the solution was filtered. The solvent was evaporated in water bath at 50 - 60°C. When all the solvent was distilled off, a detonation occurred with sudden polymerization of the distillation residue. The product was a dark, brick red material.

2.2.5. Preparation of graphene oxide coatings

Preparation of GO mixture.

Aqueous suspensions of GO were prepared by dispersing the particles in distilled water. Therefore, 0.15 g of GrO was placed in 10.0 mL distilled water and agitated for 12 h in a KS 130 orbital shaker. Then, the GrO suspension was sonicated for 1 h using a VibraCell VCX-130 ultrasonic processor. Afterwards, suspension was diluted up to 100.0 mL and sonicated repeatedly for 1 h. Prepared GO suspension was stable for several months under the laboratory conditions. It was used as a stock solution from which a working GO suspensions ($1.5 \cdot 10^{-4} \text{ g} \cdot \text{mL}^{-1}$) has been prepared by diluting (10 times) and subsequent sonification for 1 h. Suspensions of various concentrations (Table 3) were prepared according to these procedures.

Table 3. Coatings thickness and concentrations of GO suspensions.

m (GrO), g	0.050	0.062	0.075	0.087	0.100	0.150
c (GO), $\text{g} \cdot \text{mL}^{-1}$	$5 \cdot 10^{-5}$	$6.2 \cdot 10^{-5}$	$7.5 \cdot 10^{-5}$	$8.7 \cdot 10^{-5}$	$1.0 \cdot 10^{-4}$	$1.5 \cdot 10^{-4}$
Coatings thickness, nm	400	500	600	700	800	1200

Preparation of GO coatings.

Graphene oxide coatings were prepared from aqueous suspensions by slow filtering ($\sim 0.20 \text{ mL} \cdot \text{min}^{-1}$) through a polycarbonate membrane filter into alkaline media (0.10 M KOH). Filtration device developed in our laboratory are show in Fig. 8.

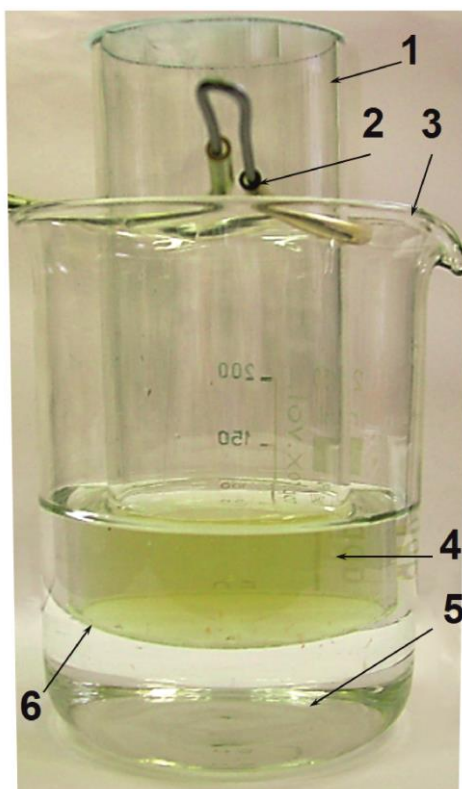


Fig. 8. Filtration device. 1 – quartz tube, 2 – holder, 3 – 250 mL laboratory glass, 4 – 24.50 mL GO suspension, 5 – 0.10 M KOH solution, 6 – polycarbonate membrane filter.

Obtained GO coatings were dried at room temperature, cut-off from the cylinder and used for the further investigations. Coatings of various thickness (varying from 400 to 1200 nm) have been prepared (Table 3).

Optimization of the transfer process of graphene oxide coatings.

The two-stage optimization procedure was chosen to optimize the process of transfer of GO coating prepared by filtration on the transparent polyethylene terephthalate substrate. At the first stage, a Plackett-Burman (PB) matrix was used to identify the most significant parameters influencing model behavior. The samples for screening were arranged using a combinatorial approach by changing the preparation conditions. After identification of the most significant parameters, further optimization was performed by the simplex method. This approach has led to the optimum conditions by changing simultaneously three

parameters. After transferring on the PET substrate, GO coatings could be used in a wide range of applications.

During the first stage of optimization PB designs were used for screening experiments because, in a PB design, the main effects are, in general, heavily confounded with two-factor interactions. These designs are very useful for economically detecting large main effects, assuming all interactions are negligible when compared with the few important main effects. Methods of construction of PB design matrix more detailed are described elsewhere [203]. In this work we used a PB experimental design matrix in 8 runs for 7 factors (Table 4).

Table 4. Plackett – Burman experimental design matrix in 8 runs for 7 factors.

Run #	Factors*						
	A	B	C	D	E	F	G
1	1	1	1	-1	1	-1	-1
2	-1	1	1	1	-1	1	-1
3	-1	-1	1	1	1	-1	1
4	1	-1	-1	1	1	1	-1
5	-1	1	-1	-1	1	1	1
6	1	-1	1	-1	-1	1	1
7	1	1	-1	1	-1	-1	1
8	-1	-1	-1	-1	-1	-1	-1

*Factors (parameters used for optimization) are presented in Table 5.

The seven parameters used for optimization (factors) and their variation ranges are presented in Table 5.

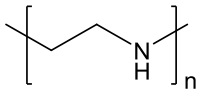
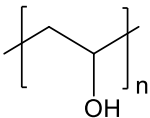
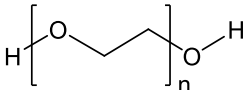
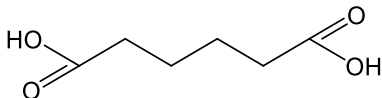
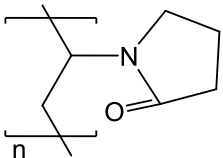
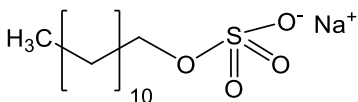
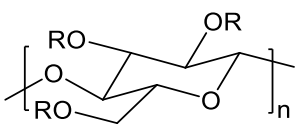
Table 5. Technological parameters used for optimization.

Factor	Corresponding technological parameter	Variation range	
		Top level (+1)	Bottom level (-1)
A	Side of PET substrate	Hydrophilic	Hydrophobic
B	Coating thickness	1200 nm	400 nm
C	Interlayer* thickness	2.0 μm	0.5 μm
D	Interlayer preparation	Dried at 80 °C	Dried at 20 °C
E	Transfer temperature	185 °C	155 °C
F	Transfer pressure	1.2 MPa	0.3 MPa
G	Solvent used to remove a PC membrane	CF	DMF

*Materials used for interlayers are enumerated in Table 6.

Transparent PET substrate – CG3360 (producer 3MTM) used in the transfer experiments was double-sided 0.1-mm thick film with different hydrophilic properties. Each side (both hydrophobic and hydrophilic) was tested for the optimization of the transfer operations. In PB testing two types of coatings were prepared: 1200 nm (“thick”) and 400 nm (“thin”). To improve the quality of adhesion, various types of interlayers were deposited onto the surface of the PET substrate by evaporating the aqueous solutions of appropriate concentrations. Materials used for the formation of interlayers are listed in Table 6. Interlayer thickness was maintained at two levels (2.0 and 0.5 μm). Another parameter used for optimization was the preparation of interlayer (dried at 80 and at 20 °C, respectively, for 4 h). Levels of the transfer temperature were taken 185 °C and 155 °C. The processing temperature ought not to extend beyond the top value due to the worsening of the optical properties: above 185 °C PET films develop a yellowish color [204]. The transfer pressure during the hot pressing varied between 1.2 and 0.3 MPa. The last optimization parameter was associated with the removal of PC membrane after the transfer procedure. Two types of solvents were used for this purpose: chloroform (CHCl_3 ; CF) and N,N-dimethylformamide ($\text{C}_3\text{H}_7\text{NO}$; DMF).

Table 6. Materials used in the formation of interlayers and their characteristics.

Material used for interlayer; abbreviation; manufacturer; grade	Structural formula	Melting point; °C	Molar mass; g · mol ⁻¹	Density; g · cm ⁻³
Marked structural characteristics in Fig. 39 e and f.	-	1	2	3
Polyethylenimine (branched); PEI; Sigma Aldrich 482595		10 ^a	1,200 ^a	1.08 ^a
Poly(vinyl alcohol); PVA; Sigma Aldrich 363138		200 ^a	40,000 ^a	1.27 ^a
Poly(ethylene oxide); PEO; Sigma Aldrich 81296		65 ^a	15,000 ^a	1.20 ^a
Adipic acid; AA; Fluka; puriss.		151	146	1.36
Polyvinylpyrrolidone; PVP; Roth 4606.2		165 ^a	24,000 ^a	1.20 ^a
Sodium dodecyl sulfate; SDS; Reachem; anal. grade		206	288	1.01
2-Hydroxyethyl cellulose; HEC; Sigma Aldrich 434965 ^b		140 ^a	90,000 ^a	0.60 ^a

^a manufacturer's data;^b R = -OH or (-CH₂-CH₂-O-)_x-H; extent of labeling 2.5 mol per mol cellulose.

To perform high-throughput mapping, samples for testing were prepared in the form of combinatorial libraries. The procedure of preparation is illustrated in Fig. 9.

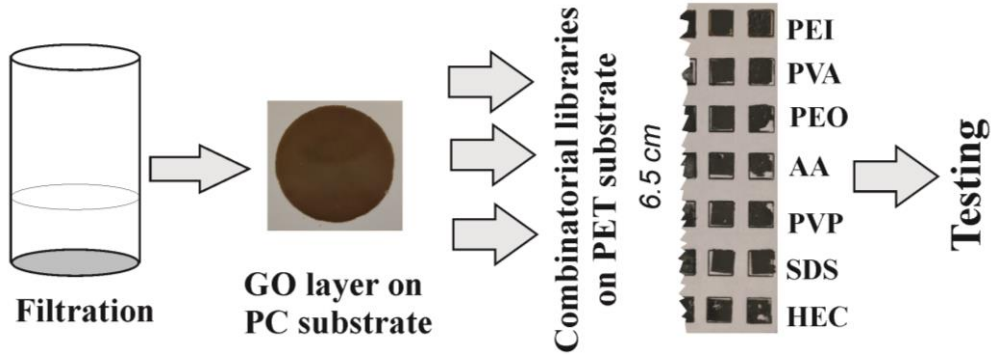


Fig. 9. Preparation of GO libraries for testing using a transfer procedure.

After deposition of GO coating of appropriate thickness onto a PC substrate and covering separate areas of the surface of the PET substrate with seven different types of interlayers, hot pressing technique was applied using a hydraulic press (Mestra M030350) to transfer the GO layer from PC to PET substrate. Prepared samples (combinatorial libraries on the base of PET sheets 1.7×6.5 cm) were used for further testing.

Data evaluation.

Data obtained in the screening experiments were used to build a linear regression model including all technological parameters of the general form [205]:

$$Y = b_0 + \sum_{i=1}^7 b_i x_i \quad (\text{Equation 1})$$

where, Y is the response signal, b_0 is the intercept, b_i are the slope parameters, and x_i are the factors included in the experiment. Values and significance of the intercepts as well as slope estimates were determined by the analysis of variance. Fisher's test was used to verify the adequacy of the model by comparing the F-value with F-critical value. F-value was determined as:

$$F = \frac{s_{res}^2}{s_{samp}^2} \quad (\text{Equation 2})$$

where s_{res}^2 stands for residual variance and s_{samp}^2 – for sample variance. Residual variance was determined as:

$$s_{res}^2 = \frac{\sum_{j=1}^8 (Y_j - \hat{Y}_j)^2}{N - l} \quad (\text{Equation 3})$$

where Y_j stands for the experimental response signal value, \hat{Y}_j – for the response signal calculated in Equation 1, N – number of runs in Plackett–Burman design matrix, and l – number of significant slope parameters. Those values of slope parameters below the significance level were set equal to zero. This means that all obtained models had the minimal amount of significant coefficients.

2.3. Characterization techniques

Fourier transform infrared spectroscopy (FTIR). FTIR measurements were carried out using a Frontier (PerkinElmer) FTIR spectrometer in the range 600 – 4000 cm^{-1} . The samples were prepared using KBr pellet technique. For this purpose sample powder (0.5% by wt.) was mixed with pure KBr powder. The mixtures were then pressed into transparent pellets for 5 minutes using PIKE CrushIR hydraulic press with a 8 ton $\cdot \text{cm}^{-2}$ pressure. Background correction was made using a reference blank KBr pellet. The spectral resolution of FTIR spectroscopes was set at 4 cm^{-1} and all spectra were acquired from 100 scans.

X-ray Powder Diffraction (XRD). The crystallographic information of the samples were characterized using a MiniFlex II (Rigaku) diffractometer with Cu K_α ($K_{\alpha 1} = 1.54056 \text{ \AA}$) radiation. XRD patterns of the powder samples were recorded for 2θ values from 5° to 55° . The characterization was done at 30 kV and 15 mA with a step size of 0.010° and a dwell time of 1.0 s. X-ray diffraction studies of TRGO fractions were performed using an X-ray diffractometer Bruker D8 Advance with Cu K_α radiation ($K_{\alpha 1} = 1.54056 \text{ \AA}$). XRD of the powder samples was recorded for 2θ values from 10° to 55° . The characterization was done at 40 keV and 40 mA with a step size of 0.040° and a dwell time of 1.0 s. The interlayer distance was calculated using the Bragg's equation:

$$n\lambda = 2d \times \sin\theta \quad (\text{Equation 4})$$

where, n is a positive integer, λ is the wavelength of the X-ray, d is the interlayer distance and θ is the scattering angle. Crystallite size was calculated using the Scherrer equation:

$$D = \frac{0.89 \times \lambda}{\beta \times \cos \theta} \quad (\text{Equation 5})$$

Where, λ is the wavelength of the X-ray, β – full width at half max (FWHM), θ is the scattering angle. From Scherrer's equation, the number of graphene (N_{GL}) layers can be determined using the following equation:

$$N_{GL} = D_{002}/d_{002} \quad (\text{Equation 6})$$

Scanning electron microscopy (SEM). Scanning electron microscope images were obtained using a Hitachi SU-70 microscope at an accelerating voltage of 5.0 kV at different magnifications. SEM images of GrO were generated using a 0.8 kV deceleration voltage.

Size exclusion chromatography (SEC). The molecular weight of polythiocyanogen ($(SCN)_n$) was determined by the size exclusion chromatography of a Viscotek GPCmax Chromatography system, using TSKgel GMHHR-M column. Tetrahydrofuran was used as the mobile phase at 30 °C with a 0.5 mL · min⁻¹ flow rate.

X-ray photoelectron spectroscopy (XPS). X-ray photoelectron spectroscopy analyses were performed in a VG Scientific ESCALAB 200A or ESCALAB MKII spectrometers using non-monochromatic Al K α radiation (1486.6 eV) and Mg K α radiation (1253.6 eV), respectively. The measurement was carried out using pellets of the materials. Binding energies were calibrated relative to the base C 1s peak at 285.0 eV or at 284.6 eV. The raw XPS spectra were deconvoluted by curve fitting peak components using the software CASAXPS or Avantage (5.962) with no preliminary smoothing. Symmetric Gaussian–Lorentzian product functions were used to approximate the line shapes of the fitting components after a Shirley-type background subtraction. Atomic ratios were calculated from experimental intensity ratios and normalized by atomic sensitivity factors.

Bulk density. The bulk density was determined by weighting and volume measurement of powder samples [206]. The weight of powder was determined by using electronic balance (KERN & Sohn GmbH). The bulk density is then obtained as the ratio of the sample weight in grams to the volume in cubic centimeters of the powder.

Blackness test of transferred GO coatings. Initially, digital images of PET sheets were made with a digital camera (Canon EOS 100D). The color intensity of selected zones, which is comparable to the transfer quality, was determined using the CorelDraw Graphics Suite version 12 (blackness test). The results of this test are in the range from 0 (least intensive black) to 10 (most intensive black).

Electrical resistance measurement of transferred GO coatings. The electrical resistance tests were carried out by measuring with an Agilent 34410A 6 1/2 digital multimeter. They served as an additional measure for the assessment of coating quality.

Contact angle measurement (CAM) of transferred GO coatings. A CAM 200 optical contact angle and surface tension goniometer (KSV Instruments) were used to assess surface wettability of nanocomposite coatings. A 1.0 μL drop of distilled water was dropped onto the surface of each sample in order to measure the static contact angle. Contact angle were calculated by KSV CAM software.

Adhesion test of transferred GO coatings. Adhesion test was performed in accordance with ASTM D3359-09e2 using a pressure-sensitive tape 3MTM 950 size 1/2 in [207].

Ash content determination. Ash content was determined by combustion of sample at 800 °C in a furnace in accordance with ASTM D3174 – 12 [208].

Raman spectroscopy. Raman spectroscopy of samples was carried out using a 633 nm He–Ne laser excitation with power restricted to 1 mW at the sample surface. The laser beam was focused into a 2 μm spot on the material surface. The integration time was 100 s. The spectra were recorded in a backscattering geometry with a confocal microscope Labram HR800, Horiba

Yvon Jobin, equipped with a diffraction grid of 600 grooves \cdot mm⁻¹ and a liquid nitrogen cooled CCD camera down to -132 °C working temperature.

CHNS Analysis. Quantitative elemental analysis CHNS was performed using a Thermo Scientific FLASH 2000 Series CHNS/O Analyser or Vario EL III analyser. Content of phosphorus was found using a Varian ICP-OES VISTA-MPX apparatus. The CHNS analyses were based on the Pregl-Dumas technique using a furnace temperature of 1100 °C. Samples were combusted completely in the presence of excess oxygen, and NO_x gases were reduced to N₂. Product gases (CO₂, H₂O, SO₂, and N₂) were captured in a mixing chamber and homogenized before being separated using gas chromatography with thermal conductivity detection. High purity helium was used as carrier gas. The results were reported as percent by weight of each element. The minimum sample size requirement for a CHNS analysis was 20 mg.

TG/DTG analysis. TG/DTG analysis was carried out using a Pyris 1, Clarus 600 TMS, Perkin-Elmer equipment. Dried samples of about 5–10 mg were heated from room temperature to 800 °C at a heating rate of 10 °C \cdot min⁻¹ in nitrogen atmosphere with a purge rate of 20 mL \cdot min⁻¹.

BET analysis. Textural properties of the carbon catalysts were determined on the basis of nitrogen adsorption at -196 °C, using Quantachrome Autosorb IQ analyser or Micromeritics TriStar II 3020 analyzer. Prior to the gas sorption measurements, all the samples (~ 0.10 g) were outgassed in vacuum at 150 °C (or in in N₂ atmosphere at 100 °C for 2 h). Total surface areas S_{BET} were calculated using the Brunauer-Emmett-Teller model, whereas the t-plot method was used to estimate the micropores volume (V_μ) and external surface area (of meso- and macropores) (S_{ext}) [209]. The total pore volume (V_{tot}) was obtained from N₂ amount adsorbed at a relative pressure close to unity.

Determination of total acidity and basicity. Total acidity/basicity of graphene-based catalysts was determined by potentiometric back-titration method using Cerko Lab System titrator. In a typical analysis, catalyst (100 mg) was added into an aqueous solution of sodium hydroxide (0.01 M, 50 mL). In case of basicity determination, catalyst (100 mg) was added into an aqueous

solution of hydrochloric acid (0.01 M, 50 mL). Then, the suspension was dispersed by shaking with a IKA KS 130 shaker for 20 h at room temperature. An excess of NaOH or HCl was used in order to completely neutralize all acidic or basic functional groups in the sample, respectively. After that the suspension was filtered and the filtrate (20 mL) was titrated with an aqueous solution of hydrochloric acid (0.05 M) or sodium hydroxide (0.05 M) solution. The total acidity/basicity was calculated as follow:

$$TA/TB = \frac{c \times (V_1 - V_0)}{m_{cat.}} \quad (\text{Equation 7})$$

where, TA/TB represents the total acidity or total basicity of the catalyst ($\text{mmol} \cdot \text{g}^{-1}$); c – represents the concentration of the NaOH or HCl standard solutions; V_1 and V_0 represent the volume of the NaOH or HCl standard solutions consumed in the titration of catalyst and blank test, respectively; and $m_{cat.}$ represents the mass of catalyst.

2.4. Activity studies

Transesterification reaction procedure. The transesterification reaction between rapeseed oil and methanol was investigated Fig. 3. Typical experiment was carried out using 50 mL of rapeseed oil and 24.4 mL of methanol. Then, 0.446 g of graphene-based catalyst was added and the reaction was carried out in a stainless steel autoclave. The transesterification process was conducted at 130 °C for 24 h in argon atmosphere under pressure of 1.3 MPa. During the reaction four samples of reaction mixture were collected (after 1, 3, 6 and 24 hours) and centrifuged at 10000 rpm for 5 min. Separated ester phase was washed with distilled water three times to remove the residual glycerol, methanol and catalyst. The product obtained was finally dried with anhydrous magnesium sulphate and analysed using a SRI 8610C Gas Chromatograph (GC) equipped with a flame ionization detector (FID) and a InertCap WAX capillary column (30m×0.51mm×1µm). Helium was used as a carrier gas at a flow rate of $4.6 \text{ mL} \cdot \text{min}^{-1}$, n-heptane as a solvent and methyl heptadecanoate as an internal standard. Temperature of GC oven was first kept at 180 °C for 4 min, then increased up to 210 °C with a heating rate of $10 \text{ }^\circ\text{C} \cdot \text{min}^{-1}$, and held at 210 °C

for 33 min. The yield of methyl esters (Fig. 10) for each sample (Y, %) was determined using the formula [210]:

$$Y, (\%) = \frac{\sum A - A_{IS}}{A_{IS}} \times \frac{c_{IS} \times V_{IS}}{W} \times 100\% \quad (\text{Equation 8})$$

where, $\sum A$ is the total peak area of methyl esters, A_{IS} – the peak area of methyl heptadecanoate, c_{IS} – the concentration ($\text{mg} \cdot \text{mL}^{-1}$) of standard solution (methyl heptadecanoate), V_{IS} – the volume (mL) of methyl heptadecanoate solution, W – the weight (mg) of the sample.

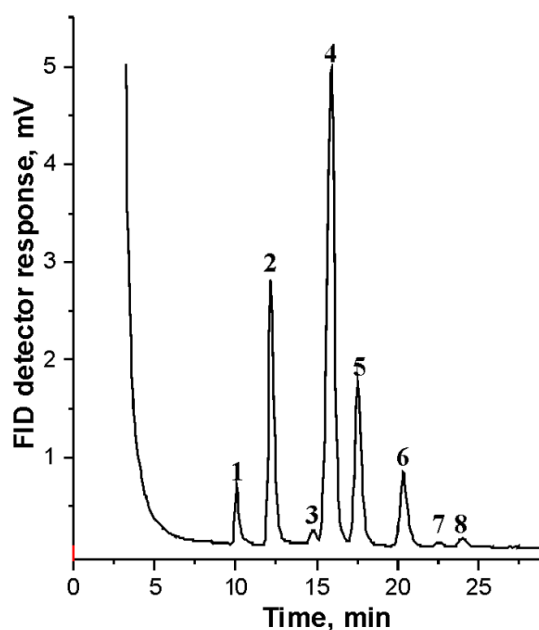


Fig. 10. The GC chromatogram of biodiesel sample obtained after 24 h by transesterification process using C_BDS catalyst. 1 – Methyl palmitate, 2 – Methyl heptadecanoate (internal standard), 3 – Methyl stearate, 4 – Methyl oleate, 5 – Methyl linoleate, 6 – Methyl linolenate, 7 – Methyl arachidate, 8 – Methyl eicosonate.

Electrochemical measurements. Electrochemical measurements of SS/G-60 nanocomposite material were performed using an electrochemical system “PARSTAT 2273” with a conventional three-electrode system composed of an auxiliary platinum plate electrode, a reference Ag/AgCl (KCl, 3 M) electrode, and a working graphite rod (\varnothing 3 mm) coated with graphene-based material electrode. Prior to surface modification, the bare graphite rod electrode

was polished with a thin abrasive paper and then subjected to ultrasonic treatment (60 Hz) for 10 minutes in distilled water. After that 9 μL of SS/G-60 nanocomposite material ink was deposited on electrode surface. Aiming to prepare the SS/G-60 nanocomposite material ink a slurry of 30 mg of SS/G-60, 50 μL of distilled water, 0.5 mL of absolute ethanol, and 10 μL of Nafion® (0.05 wt% in distilled water) were mixed. An aliquot (9 μL) of ink was deposited onto the graphite rod and dried at room temperature for 30 min. For control experiments the working graphite rod was coated with graphite ink similarly prepared as in a case of SS/G-60.

The electrocatalytic activity of prepared electrode towards ORR was examined using a linear sweep voltammetry (LSV). The LSV measurements were conducted by sweeping the potential from 1 V to -2.5 V in O_2 saturated 0.0005 M (pH = 3.00), 0.0025 M (pH = 2.30), 0.0035 M (pH = 2.15), 0.005 M (pH = 2.00), 0.025 M (pH = 1.30), 0.035 M (pH = 1.15), 0.05 M (pH = 1.00), 0.5 M (pH = 0), 0.75 M (pH = -0.18) and 1M (pH = -0.30) of H_2SO_4 at different scan rates (from 10 to 500 $\text{mV} \cdot \text{s}^{-1}$). Aiming to evaluate an efficiency of ORR the LSV measurements were also conducted by sweeping the potential from 1 V to -2.5 V in Ar saturated 0.5 M (pH = 0) of H_2SO_4 . All measurements were carried out at ambient temperature of 22 $^\circ\text{C}$.

3. RESULTS AND DISCUSSION

3.1. Graphene - based heterogeneous catalysts for transesterification process

In this part of dissertation the obtaining of biodiesel by transesterification process using different modified graphene-based materials as catalysts was studied. Solid acidic graphene-based catalysts were prepared by grafting – sulphonic or phosphate groups on the surface of thermally reduced graphene oxide by treating it with concentrated sulphuric acid, in situ generated diazonium salt of 4-aminobenzenesulphonic acid or concentrated phosphoric acid. To introduce basic sites, TRGO was modified with gaseous ammonia or melamine at different conditions.

3.1.1. Structural characterizations of graphene-based acidic catalysts

SEM analysis.

SEM micrographs of precursor, intermediate products and catalysts used in transesterification reaction are presented in Fig. 11. In Fig. 11 a the layered crystalline structure of graphite is clearly observable and it is distinctly different from the other samples. The structure of GrO (Fig. 11 b) changes dramatically. Oxidative treatment leads to the expansion of interplanar spacing of graphite and reduction of the number of stacked layers. The consequence of this process is the corrugated morphology of GrO. TRGO is consisting of stacked individual carbon sheets (Fig. 11 c). Thermal treatment of GrO results in obtaining of a typical "worm-like" turbostratic structure with low volume density. Further treatment of TRGO with acidic reagents is reflected by characteristic changes in the samples' morphology. Treatment with sulphuric acid had effect on the edge structure of graphene sheets (Fig. 11 d, e). Longer treatment time has caused more extensive separation of individual sheets. The morphology of samples functionalized with 4-aminobenzenesulphonic acid (Fig. 11 f) is similar to that of TRGO. The catalyst sample functionalized with phosphoric acid somewhat resembles samples functionalized with sulphuric acid as well as pristine TRGO

(Fig. 11 g). For the comparison, morphology of Amberlyst-15 (Fig. 11 h) is substantially different from the morphology of graphene-based catalysts and pristine materials.

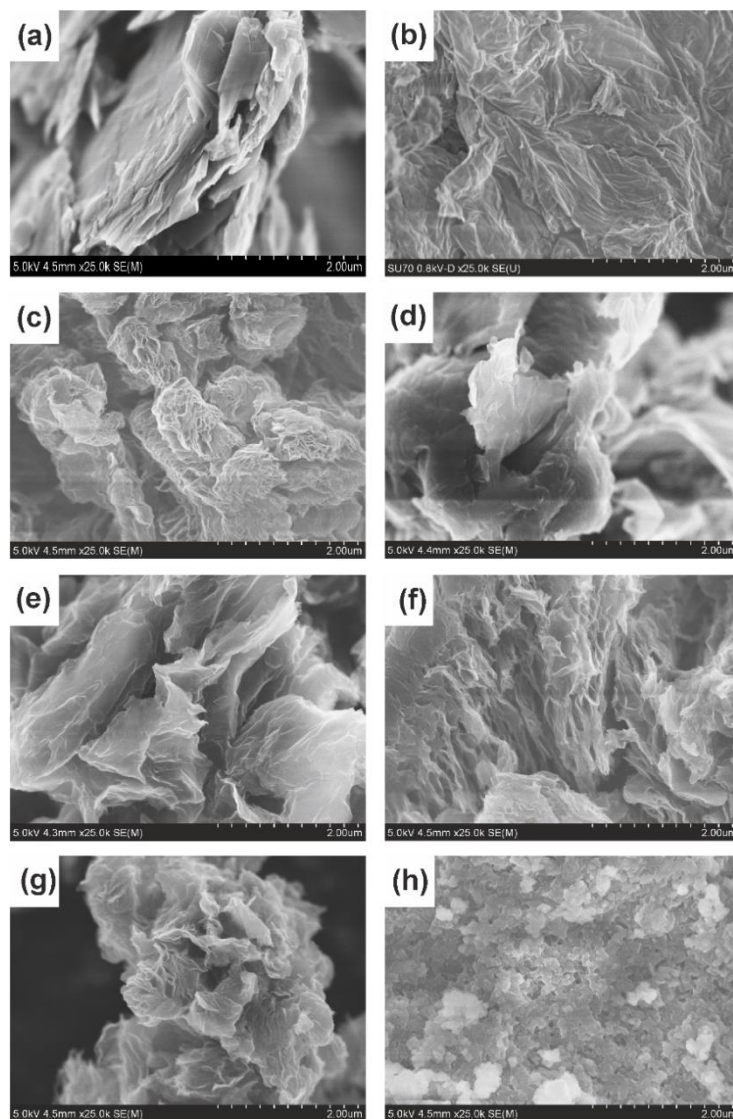


Fig. 11. SEM images of precursor, intermediate products and catalysts used in transesterification reaction: a – graphite, b – GrO, c – TRGO, d – C_SA_5, e – C_SA_20, f – C_BDS, g – C_PA, h – Amberlyst-15.

Powder X-ray diffraction analysis.

The above differences in the structure of the samples are reflected in their XRD diffractograms Fig. 12.

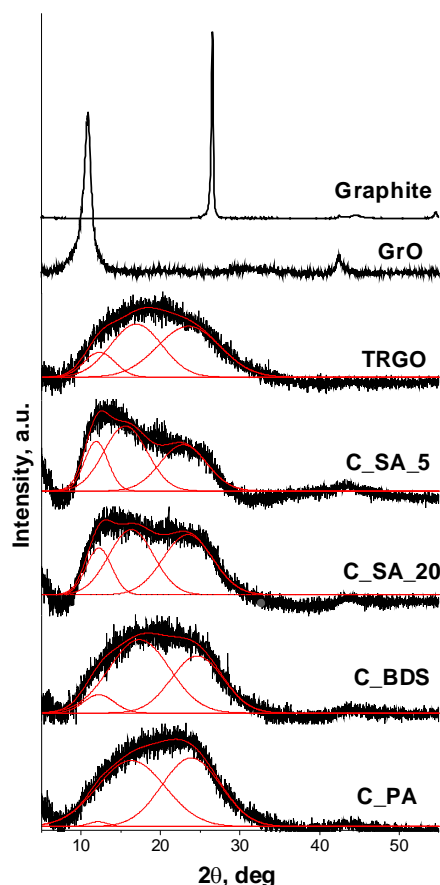


Fig. 12. XRD patterns of precursor, intermediate products and catalysts used in transesterification reaction.

Pristine graphite has a high degree of crystallinity and characteristic peak at $2\theta = 26.7^\circ$. The XRD pattern of GrO is consistent with the majority of the literature [211]. The peaks in the diffractogram of GrO ($2\theta = 10.35^\circ$ and $2\theta = 42.57^\circ$) correspond to the enlarged interlayer distance of 0.816 nm. The peaks in the XRD patterns of TRGO and catalyst samples have become broader because of the decrease of the crystallite size. For graphitic materials, the broadening of the (100) and the absence of (h0l) reflections indicate a turbostratic layer structure [212], while the graphene-like layers have a random orientation about the direction perpendicular to the layer [213]. This type of structure is presented in SEM micrographs (Fig. 11 c – g) of prepared samples. The Gaussian fitting curves of XRD peaks in TRGO and catalyst samples can be attributed to the peaks of graphite (002) and GrO (001). The main fitting parameters (peak position, FWHM and peak intensity) are presented in Table 7.

Table 7. The fitting results of XRD patterns performed for TRGO and catalyst samples.

Samples	Peak 1			Peak 2			Peak 3		
	2 θ ; deg	FWHM	Intensity; (a.u.)	2 θ ; deg	FWHM	Intensity; (a.u.)	2 θ ; deg	FWHM	Intensity; (a.u.)
TRGO	12.32	4.60	0.037	16.95	7.60	0.079	23.55	9.25	0.076
C_SA_5	11.92	6.87	0.091	15.59	6.40	0.127	22.87	3.47	0.097
C_SA_20	12.25	3.75	0.083	16.31	6.62	0.116	23.44	7.32	0.107
C_BDS	12.25	4.53	0.063	17.34	9.00	0.253	24.62	7.66	0.197
C_PA	12.16	2.87	0.022	16.31	10.00	0.290	23.87	8.65	0.301

The fitting curves have highlighted the similarities and differences between the TRGO and catalyst samples. The XRD pattern of C_BDS most closely resembles that of TRGO, similar results are found also in the micrographs. Another group includes the catalyst samples treated with sulphuric acid: the ratios of Gaussian fitting peaks as well as the shapes of XRD patterns are alike. The catalyst sample treated with phosphoric acid stands apart from the other in this set by crystallinity: the fitting curve at $2\theta = 12.16^\circ$ is almost extinct. Consequently, the increased interplanar spacing in hexagonal close-packed structure is no more characteristic to C_PA, while this type of crystallinity is present in the other catalyst samples and TRGO.

BET analysis.

The parameters calculated from nitrogen adsorption measurements are summarized in Table 8.

Table 8. Surface area and pore volume data obtained from nitrogen adsorption measurement.

Samples	S_{BET} ($\text{m}^2 \cdot \text{g}^{-1}$)	S_{ext} ($\text{m}^2 \cdot \text{g}^{-1}$)	V_{tot} ($\text{cm}^3 \cdot \text{g}^{-1}$)	V_{μ} ($\text{cm}^3 \cdot \text{g}^{-1}$)
Graphite	12	11	0.03	0.00
GrO	46	41	0.17	0.00
TRGO	617	617	3.82	0.00
C_SA_5	485	468	2.20	0.01
C_SA_20	513	511	2.29	0.00
C_BDS	422	413	2.76	0.00
C_PA	300	206	0.99	0.05
Amberlyst-15	53 ^a	-	0.40 ^a	-

^aManufacturer's data.

The results obtained prove that all samples studied are predominantly meso- and macroporous materials ($V_{\mu} \approx 0$). Total and external surface area (S_{BET} and S_{ext}) as well as total pore volume (V_{tot}) increase significantly after the thermal

treatment of GrO, what is a consequence of exfoliation and separation of particular graphene layers caused by decomposition of oxygen functionalities (see SEM and elemental analysis results). Subsequent functionalization leads to a reduction of these parameters. By comparing these results with the XRD fitting data (Table 7) a very good negative correlation with the peak intensity at $2\theta = 23.55^\circ$ can be found. This mutual reliance means that the samples with the higher graphite-like crystallinity degree (since peak 3 represents reflections from the (002) graphite plane) will be characterized by the lower surface area values. Simultaneously, a positive correlation can be found between S_{BET} and the fitted peak intensity for peak 1 at $2\theta = 12.32^\circ$. This peak represents reflections from the plane (001) in GrO. That is to say that the samples with the higher residual GrO-like crystallinity will be characterized by the higher surface area values. As well as in other cases, the sample C_PA stands out from the others: S_{BET} , S_{ext} and V_{tot} are reduced to the relatively small values, but the portion of micropores in it is the largest.

Elemental analysis and acid/base properties of the surface.

The elemental analysis data of the samples obtained by CHNS analyser (EA) and XPS, and data of total acidity/basicity measurements are given in Table 9. The ash content was determined as the residue after combustion. Thus, the origin of ash may be related to the presence of incombustible substances (chlorine, potassium, phosphorus compounds, etc.) that can be introduced during the chemical treatment of graphite and intermediate products (see Experimental). Exceptionally high ash content is present in C_PA (9.4%), which also has high phosphorus content (7.2%). It indicates that phosphorus after combustion accumulates mainly in the ash fraction. Further analysis of EA data presented in Table 9 proves that oxidation of graphite is very efficient (oxygen content increase from 0.2 to over 43 wt%). After thermal reduction of GrO some of the oxygen groups undergo decomposition and this is why the oxygen content substantially decrease. However, even such a drastic treatment (temperature of 800 °C) leads to the product which still contains a high oxygen level.

Table 9. Element contents of catalyst samples determined by EA and by XPS and total acidity/basicity results (dry basis).

Analysis	Sample	Element content (mass %)						Total acidity (mmol · g ⁻¹)	Total basicity (mmol · g ⁻¹)
		Ash (wt%)	C (wt%)	H (wt%)	N (wt%)	S, (P) (wt%)	O ^a (wt%)		
EA ^c	Graphite	0.0	99.7	0.1	0.0	0.0	0.2	0.04	0.06
	GrO	1.5	51.0	2.3	0.1	1.8	43.3	3.74	0.00
	TRGO	1.5	83.3	1.2	0.3	2.0	11.7	0.83	0.00
	C_SA_5	0.5	82.9	1.1	0.4	1.5	13.6	1.03	0.00
	C_SA_20	1.2	81.9	1.1	0.3	1.6	13.9	1.09	0.00
	C_BDS	1.3	73.8	2.1	0.8	4.7	17.3	1.46	0.00
	C_PA	9.4	75.4	1.4	0.3	1.3 (7.2)	5.0	1.38	0.00
	Amberlyst-15	-	-	-	-	-	-	4.70 ^b	-
XPS ^d	TRGO	-	82.6	-	0.0	2.6	14.8	-	-
	C_SA_20	-	83.0	-	0.0	2.9	14.1	-	-
	C_BDS	-	73.1	-	0.9	8.1	17.9	-	-
	C_PA	-	79.6	-	0.0	0.0 (7.6)	12.8	-	-

^a Calculated by difference; ^b Manufacturer's data; ^c Bulk element content determined by CHNS analyser; ^d Surface element content determined as mass percentages based on the areas of the respective peaks in the high-resolution XPS spectra (atomic contents) and the respective atomic masses.

It indicates that oxygen functionalities present in TRGO are very thermally stable (e.g. carbonyl, quinone or pyrone structures [214, 215]). Functionalization of TRGO with H_2SO_4 or BDS causes some increase in oxygen content, which is a consequence of introduction of oxygen-contained sulphonic groups into graphene structure. Furthermore, hot, concentrated sulphuric acid is a strong oxidizing agent that upon contact with the carbonaceous material generates carboxylic groups [216]. On the other hand, the reaction of TRGO with H_3PO_4 does not increase the oxygen content (calculated by difference), because, as already mentioned, the introduced phosphate groups have been accounted by the increase in the ash content. The nitrogen content is on similar level in most samples. The same applies to the sulphur content. This situation may occur when the nitrates and sulphates are not completely washed out from the bulk of GrO phase after oxidation step. The exception is the C_BDS sample for which a much higher nitrogen and sulphur contents are observed by both techniques, which is a consequence of the presence of these elements in the BDS. Accordingly, it can be concluded that the moieties of BDS are grafted to the graphene planes of TRGO. The sulphur content decreases slightly after treatment with H_2SO_4 or H_3PO_4 , which means that the residual sulphate ions can be removed in a strong acidic media. This result also indicates that for the samples modified with H_2SO_4 the above process dominate over the process of sulphonic groups formation. Moreover, the data presented in Table 9 clearly prove that sulphuric acid is rather weak sulphonating agent and much more sulphonic groups can be introduced into graphene structure using BDS (see the total acidity data).

The XPS mass percentages show differences relatively to EA results. The XPS data shows the absence of sulphur in C_PA and nitrogen in all catalyst samples (except C_BDS). This can be justified since XPS is a much more surface sensitive technique (covering 10 nm deep from the surface) while EA is a bulk analysis and functional groups can be selectively leached from the surface during the reaction and washing procedures. No essential differences are noted between the surface and the bulk content of carbon. As follows from analysis of the data, the mass % values of oxygen, sulphur, nitrogen and phosphorus

obtained by XPS are greater than those from elemental analysis. This fact shows that functional groups formation occurs predominantly on the edges of TRGO than in the bulk.

Thermal analysis.

The results of TG analysis are given in Fig. 13. A very good correlation between the data in Fig. 13 and Table 9 can be found, since the mass loss indicates the presence of the heteroatoms (H + O + N + S + P). The largest slope is observed for GrO and C_BDS, since these samples are the richest in heteroatoms. Insert in Fig. 13 shows the mass loss of graphite, TRGO and three catalyst samples (except C_BDS) up to 400 °C. There one can see that the C_PA sample stands out by the minimum slope next to graphite.

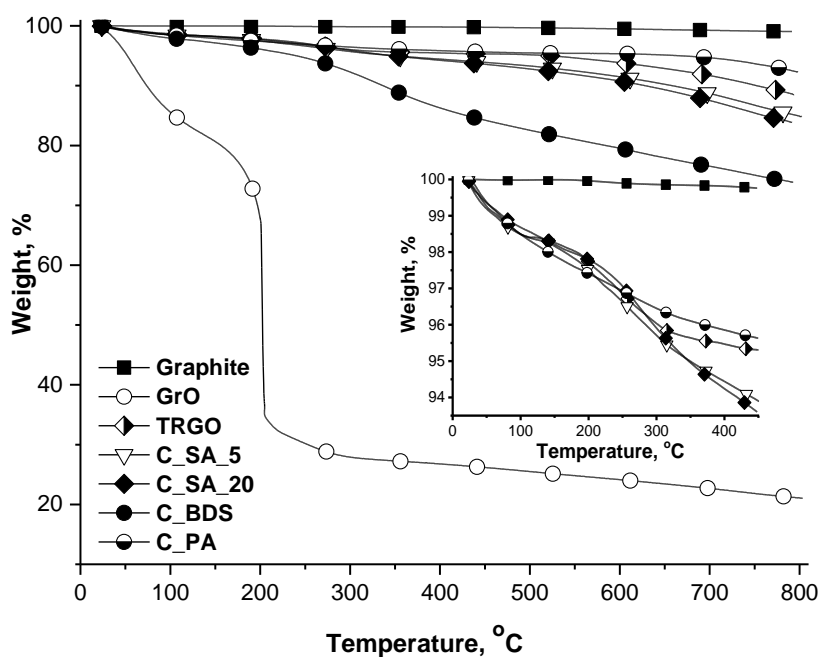


Fig. 13. TG analysis of graphite, intermediate products and catalyst samples.

FTIR spectroscopy.

In Fig. 14 the FTIR spectra of precursor, intermediate products and graphene-based catalysts are presented. FTIR spectrum of GrO sample is consistent with the spectra reported elsewhere [60, 217]. The most characteristic features are broad intense band at 3400 cm⁻¹ (O–H stretching vibrations) and the

bands at 1730 cm^{-1} (C=O stretching vibrations from carbonyl and carboxyl groups), 1560 cm^{-1} (skeletal vibrations from unoxidized graphitic domains), 1226 cm^{-1} (C–OH stretching vibrations), and 1055 cm^{-1} (C–O–C stretching vibrations). The majority of those peaks are present in the TRGO, C_SA_5, C_SA_20, C_PA and C_BDS samples.

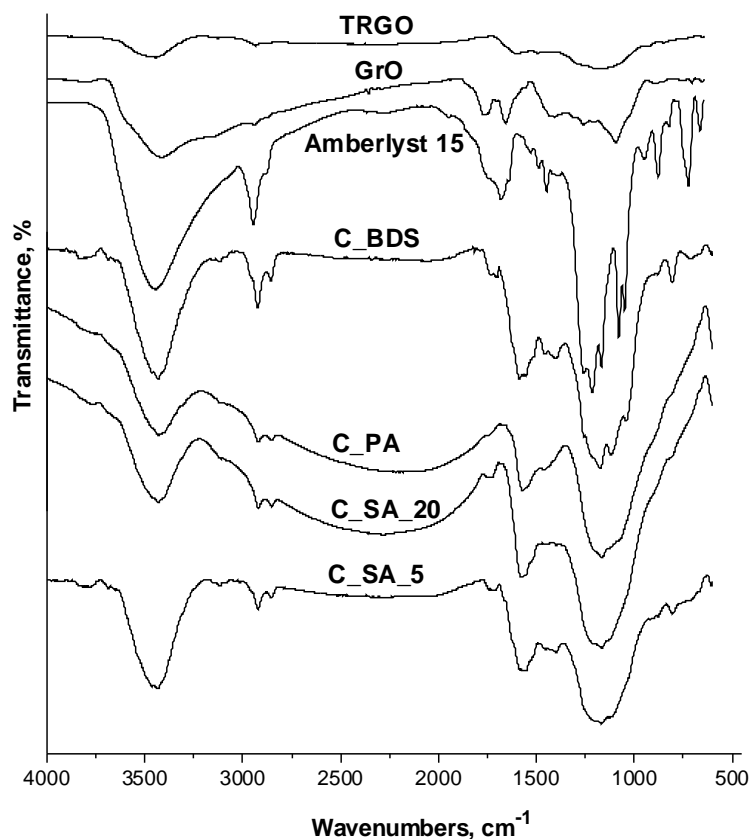


Fig. 14. FTIR spectra of intermediate products and catalysts used in transesterification reaction.

The FTIR spectrum recorded for Amberlyst-15 shows characteristic vibrations consistent with the presence of various functional groups. The peak corresponding to the uncoordinated water was found at 3433 cm^{-1} for asymmetric and symmetric O–H stretching modes and at 1646 cm^{-1} for H–O–H bending modes. The presence of $-\text{SO}_3-$ moiety is confirmed by the peaks at 1128 cm^{-1} , 1008 cm^{-1} , 834 cm^{-1} and 677 cm^{-1} [218]. To the same group may be assigned the peaks in C_BDS FTIR spectrum (1120 cm^{-1} , 1043 cm^{-1} , 804 cm^{-1} and 612 cm^{-1}), while in the spectra of TRGO, C_SA_5 and C_SA_20 these

peaks are not visible since they are being overlapped by the broad bands corresponding to oxygen linkages. Spectra of C_PA also contain broad bands, which make peak assignments somewhat more difficult. The peak at 1175 cm^{-1} , present both in Amberlyst-15 and C_BDS, reflects in-plane bending vibrations in 1,4 substituted aromatic rings.

XPS analysis

Further information about the oxygen, sulphur and phosphorus functionalities was provided by deconvolution of the C1s, O1s, S2p and P2p core-level XPS spectra (Fig. 15 and Table 10).

Analysis of the C1s spectra of the TRGO material (Fig. 15 a) shows a peak at binding energy (B.E.) 284.3 eV ascribed to carbon in the graphitic structure and aromatic rings (sp^2). The C=C component is the most intense peak among all the deconvoluted peaks, meaning that C=C is the main C bonding configuration, which creates the graphitic structure. The peak at 285.6 eV is assigned to C–C single bonds species in the carbon structure (sp^3). Other two peaks are associated with the presence of the oxygen containing groups: the peak at 287.2 eV is assigned to the hydroxyl and epoxy groups (C–O), the smaller peak at 288.4 eV attributed to the carbonyl or carboxylic groups (C=O). It should also be noted that the C1s profiles did not show a broad, weak component at around 291.0 eV, which comes from the $\pi \rightarrow \pi^*$ transition of carbon atoms in graphene structure [219, 220].

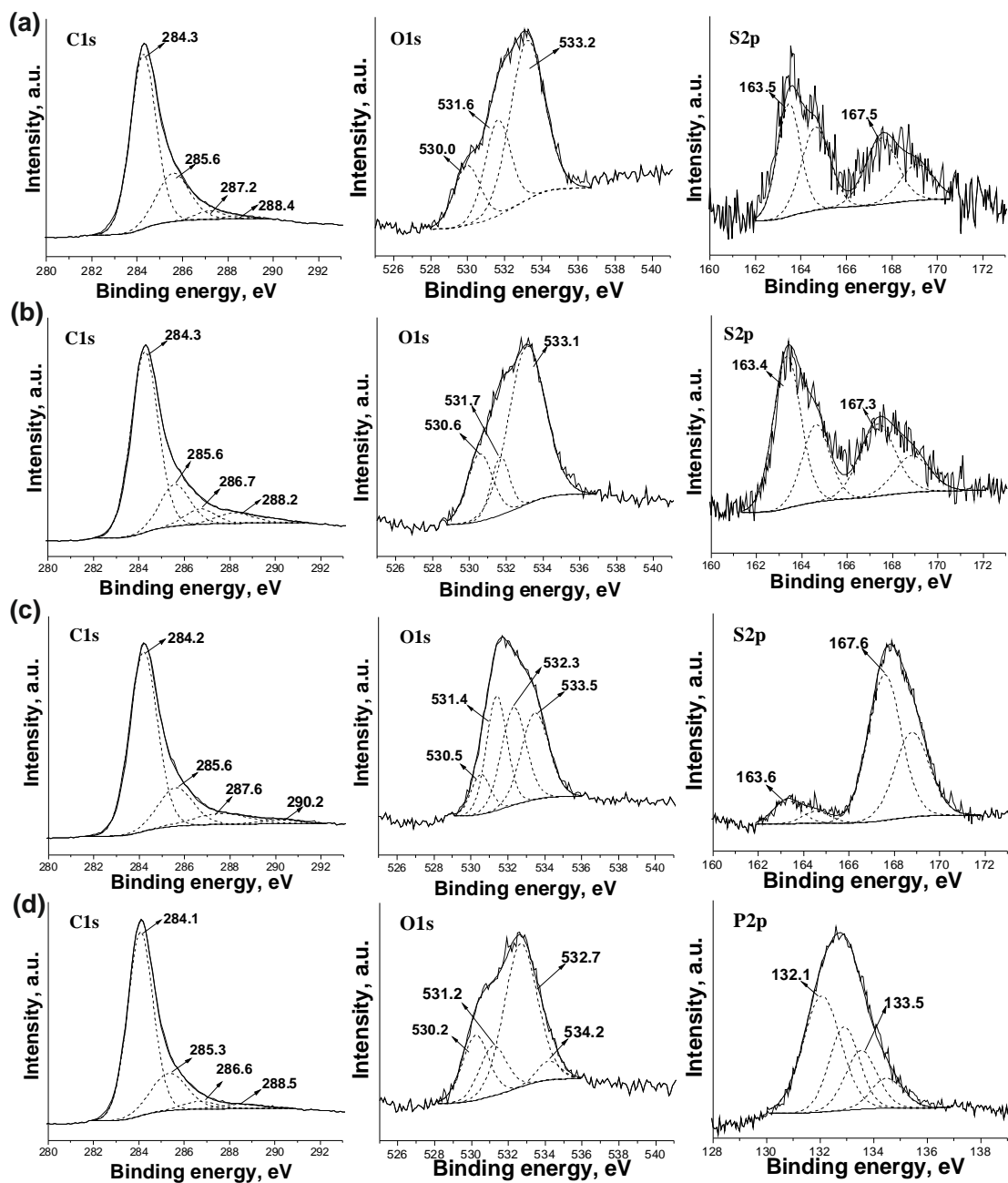


Fig. 15. C 1s, O 1s, S 2p and P 2p XPS spectra of TRGO (a), C_SA_20 (b), C_BDS (c) and C_PA (d).

Table 10. Analysis of high resolution XPS spectra of catalysts obtained.

Sample	BE, ^a eV (concentration of species, at %)												
	C 1s		O 1s				S 2p		P 2p		N 1s		
	C=C	C-C	C-O, C-S	C=O, O-C=O, C-P	C=O	O=P, O=C	S-O, O-P, P-OH	O-C, O-C=O,	C-S _n ^b	-SO _n	P-C, P-O	P=O	-N=N-
TRGO	284.3	285.6	287.2	288.4	530.0	531.6		533.2	163.5	167.5			
	(61.2)	(21.8)	(3.2)	(1.1)	(2.0)	(3.0)	-	(6.8)	(0.6)	(0.4)	-	-	-
C_SA_20	284.3	285.6	286.7	288.2	530.6	531.7		533.1	163.4	167.3			
	(61.4)	(15.6)	(5.9)	(4.8)	(2.2)	(1.4)	-	(7.5)	(0.8)	(0.3)	-	-	-
C_BDS	284.2	285.6	287.6	289.2	530.5	531.4	532.3	533.5	163.3	167.6			401.5
	(57.3)	(15.3)	(6.9)	(1.7)	(1.4)	(4.4)	(4.6)	(4.5)	(0.3)	(3.0)	-	-	(0.6)
C_PA	284.1	285.3	286.6	288.5	530.2	531.2	532.7	534.2			132.1	133.5	
	(62.6)	(17.9)	(3.5)	(2.4)	(2.2)	(1.7)	(6.0)	(0.6)	-	-	(2.2)	(0.9)	-

^a For 2p orbitals the B.E. of 2p_{3/2} orbital is presented; ^b n = 1 or 2.

After modifications (Fig. 15 b, c, d; C1s XPS spectrum) the peaks at 287.2 eV and 288.4 eV are slightly shifted. Moreover, the concentration of these bands is increased from 3.2 % to 5.9%, 6.9%, 3.5% and from 1.1% to 4.8%, 1.7%, 2.4%, respectively, which can be associated to the presence of C–S functionalities (in case of C_SA_20 and C_BDS) and C–P (in case of C_PA) [221-223].

In the O1s XPS spectrum of the TRGO material there are present a peaks at 530.0 eV, 531.6 eV assigned to O=C species, and a much more intense peak at 533.2 eV ascribed to O–C single bond or O–C=O functionalities (Fig. 15 a). This indicates that hydroxyl, epoxide or carboxylic acid groups are more abundant than the carbonyl or quinone groups [224-226]. These three peaks are also present in the XPS spectra of other catalysts (Fig. 15 b, c, d), however, a drastic reduction of the concentration of C-O/O-C=O species from 6.8% in TRGO to 4.5% in C_BDS and to 0.6% in C_PA materials is observed. Simultaneously a new two peaks at 532.3 eV assigned to S-O [227] and 532.7 eV ascribed to O-P, P-OH [221] appeared. The exception is the C_SA_20 sample (Fig. 15 b; O1s XPS spectrum) for which the content of O-C/O-C=O species slightly increases from 6.8% to 7.5%, which can be explained by formation of oxygen groups of acidic character, such as lactone or carboxylic groups, during acid treatment [216].

The S bands in S2p region appear in the form of doublets, due to the degeneration in the B.E. of $2p_{3/2}$ and $2p_{1/2}$ orbitals. Fig. 15 a shows S2p spectrum of TRGO. It is clearly seen that the high-resolution S2p XPS spectrum of TRGO is composed of two peaks: a lower energy doublet found at 164.6 eV ($S2p_{1/2}$) and 163.5 eV ($S2p_{3/2}$) is typical of sulphur in C-S_n- systems, and a higher energy doublet at 167.5 and 169.1 eV can be assigned to sulphonic acid/sulphate groups (-SO_n) [227]. The peak intensity of C-S_n- was higher than that of -SO_n, indicating that C-S_n- was the dominant state of sulphur in TRGO. The observation of -SO_n/C-S_n- species at the surface of TRGO is not surprising since GO employed to prepare TRGO contained residual intercalated sulphuric acid, which was not completely washed out after oxidation step (Table 9). According

to the literature, the products of H_2SO_4 thermal decomposition (SO , SO_2) can recombine with oxygen groups on the carbon surface to form the mentioned above species [228, 229].

In the case of C_SA_20, the amount of C-S_n- band increases from 0.6% to 0.8% and -SO_n band slightly decreases from 0.4% to 0.3%. This results correlate with EA analysis data, and prove, that the residual sulphate ions can be removed in a strong acidic media. For C_BDS sample, the amount of C-S_n- band decreases to 0.3%, and the amount of -SO_n band drastically increases to 3.0%. These results indicate that the surface density of -SO_n species strongly depends on the functionalization methodology applied. Indeed, TRGO functionalization via BDS seemed to be the most effective one, whereas TRGO and H_2SO_4 pretreatments afforded a very small density of -SO_n groups. Thus the results obtained are a confirmation of the analytical data presented in Table 3 and prove that sulphuric acid is weaker sulphonating agent than BDS.

The high-resolution P2p XPS spectrum of the C_PA sample is shown in Fig. 15 d. The deconvolution of the P2p region shows four peaks at 132.9 eV, 132.1 eV, 134.5 eV and 133.5 eV, corresponding to the B.Es of P2p_{1/2} and P2p_{3/2}. The values of B.E. presented always refer to the 2p_{3/2} orbital (Table 10). Both the phosphorus environments P2p_{3/2} at 132.1 eV (P-C, P-O-C) and P2p_{3/2} at 133.5 eV (P=O) are assigned to the presence of phosphate groups [221, 224].

The N1s region of C_BDS sample shows only one peak at 401.5 eV assigned to -N=N- species (Table 10). The presence of N1s emission for carbon modified with diazonium salts, proved that the dediazonation step is incomplete during the grafting process [230]. It can be concluded, that the aryl groups are bonded to the carbon via -N=N- bonds.

3.1.2. Activity of solid acidic catalysts

Finally, the modified graphene based catalysts were tested in transesterification reaction of rapeseed oil with methanol. The yields of fatty acid methyl esters obtained in the above process are given in Fig. 16.

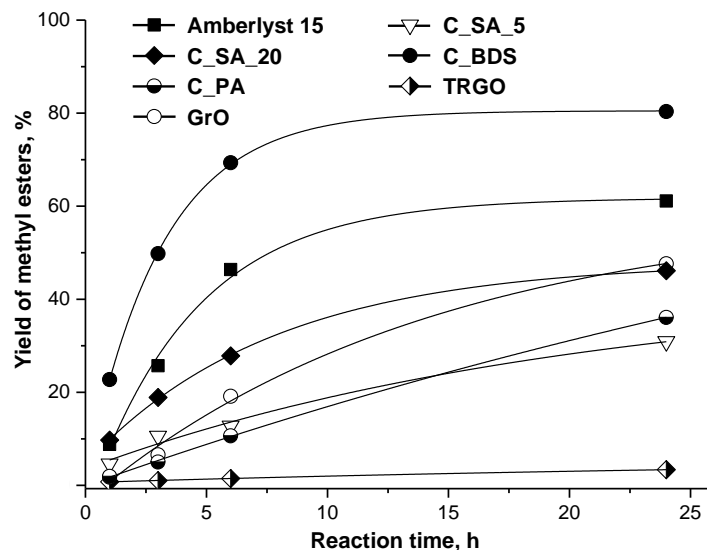


Fig. 16. Comparison of FAME yields obtained for the graphene-based catalysts and commercial catalyst.

For comparison purposes the yield obtained with the use of commercial catalyst Amberlyst-15 is also presented. As depicted in Fig. 16, the yield of FAME clearly increased with increasing reaction time and reached a plateau after 24 h, regardless of the used catalytic system (after this time the product yield increased only slightly). The results presented indicate that the catalysts investigated have the activity (which can be defined by FAME yield) in the range of 2 to 80%. It is clearly visible that the sample functionalized with 4-aminobenzenesulphonic acid (C_BDS) shows the best catalytic activity. After 24 h of reaction, the yield of FAME obtained using C_BDS was up to 80 %. This result is even better than that attained for commercial catalyst Amberlyst-15 (60% after 24 h), despite a much higher content of acidic groups on Amberlyst-15 surface ($4.66 \text{ mmol} \cdot \text{g}^{-1}$) than on C_BDS surface ($1.46 \text{ mmol} \cdot \text{g}^{-1}$). The higher catalytic activity of C_BDS over Amberlyst-15 may be associated with its unique two dimensional sheet structure, where most of the $-\text{SO}_3\text{H}$ groups are well dispersed and exposed to the reactants. On the other hand, Amberlyst-15 represents a porous structure with much lower S_{BET} than C_BDS (Table 8). As a consequence, some of the $-\text{SO}_3\text{H}$ groups on this

catalyst might not be accessible to reactants, which leads to a lower product yield.

For samples modified with sulphuric acid the activity grows with increasing total acidity (31% for C_SA_5 and 46% for C_SA_20 after 24 h of the reaction). GrO sample and sample modified with phosphoric acid show relatively low catalytic activity, although their acidity is high. For the C_PA sample this is a consequence of lower acid strength of the phosphate groups in comparison with the sulphonic ones. Similarly, the GrO acidity is associated with weak hydroxyl and carboxyl groups on the basal planes and external edges of the GrO nanosheet [55]. These results suggest that not only the concentration of acid sites, but also their strength is essential in FAME synthesis by transesterification reaction. The TRGO sample taken for comparison reaches only 3 % of FAME yield after 24 h of transesterification reaction, although its specific surface area is the largest ($617 \text{ m}^2 \cdot \text{g}^{-1}$). The main reason for such a poor result is the low content of acid sites (Table 9), which in addition are weak (they were created as a result of thermal decomposition of earlier mentioned oxygen groups contained in GrO).

In conclusion, all samples tested in this study showed some catalytic activity in the transesterification reaction of rapeseed oil with methanol. The best yield of biodiesel was obtained for the sample functionalized with 4-aminobenzenesulphonic acid. It can be concluded that a catalyst which shows high catalytic activity in the above process need to have a certain amount of surface acid functionalities. Furthermore, not only the concentration of acid sites, but also their strength is essential in FAME synthesis by transesterification reaction. The mesoporous pore structure and high surface area are also beneficial parameters in the process studied, however their importance is rather secondary. Simultaneously, a positive correlation between the degree of graphene-like crystallinity and the yield of product in transesterification reaction has been established. Supposedly, a synergistic effect of sulphonic groups and graphene-like crystallinity plays a crucial role in such efficient work of the catalyst modified with BDS. In view of the above, it can be supposed that further

study aimed at introduction of a larger number of strong acidic groups on the surface of graphene-based materials will bring catalysts ensuring higher yields of FAME in the reaction tested.

3.1.3. Structural characterizations of graphene-based basic catalyst

SEM analysis.

The microstructural characteristics of the nitrogen-doped graphene samples were analyzed by scanning electron microscopy. SEM micrographs are presented in Fig. 17.

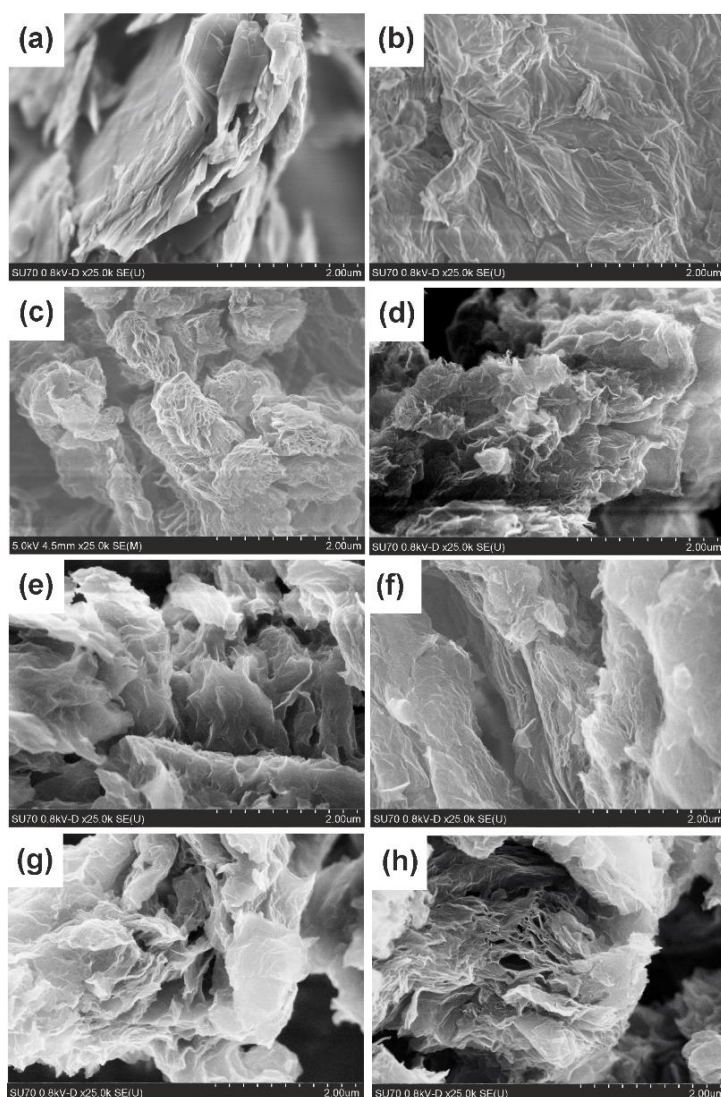


Fig. 17. SEM images of precursor, intermediate products and catalysts used in transesterification reaction: a – graphite, b – GrO, c – TRGO, d – C_Am_4_850, e – C_Am_8_850, f – C_Am_4_950, g – C_Am_8_950, h – C_Me_1_700.

For comparison, SEM image of graphite, GrO and TRGO is presented in Fig. 17 a, b, c. The change of morphologies of pristine materials were previously described in 3.1.1. section and shown in Fig. 11. The treatment of TRGO with ammonia (Fig. 17 d – g) is reflected by characteristic changes in the samples' morphology. As can be seen crumpled graphene nanosheets are randomly arranged and overlapped with each other, these could easily have formed a slit-shaped porous structure. The wrinkles observed in the graphene nanosheets are most likely due to the incorporation of heterogeneous nitrogen species into the graphitic network. Moreover higher modification temperature and longer treatment time has caused more extensive separation of individual sheets and increasing the degree of wrinkling (Fig. 17 e, g). The morphology of samples functionalized with melamine (Fig.17 h) is similar to that of TRGO.

Powder X-ray diffraction analysis.

The XRD patterns of graphite, GrO, TRGO, and prepared catalysts are shown in Fig. 18. The results obtained clearly show that, after thermal reduction and nitrogen doping, the peaks in the XRD patterns have become broader because of the decrease of the crystallite size. Obviously, in all cases, the diffraction peaks centered at approximately $2\theta = 22^\circ$ are asymmetric because of a mixed polycrystalline structure of graphitic and disordered domain. It can be seen that the XRD patterns can be fitted by using a Gaussian function into three separate peaks. The main fitting parameters (peak position, FWHM) and calculated interlayer distances are presented in Table 11. The Gaussian fitting curves of XRD peaks in TRGO and catalyst samples can be attributed to the peaks of graphite (002) and GrO (001). The fitting curves show the differences between TRGO and catalyst samples. A small characteristic diffraction peak of GrO (001) at approximately 12.32° still remained in the XRD pattern of TRGO, that corresponds to an interlayer spacing distance of 0.718 nm. These results confirmed the partial reduction of GrO to TRGO. Residual oxygen functional groups still remain on the surface of TRGO. After the repeated operation of

thermal treatment, which followed by modification with ammonia or melamine, it was observed that the (001) peak shifted from 12.32° to approximately $2\theta=16 - 18^\circ$, demonstrating the further reduction of TRGO. In addition, the peak of N-doped catalysts at $2\theta = 16 - 18^\circ$, which is characterized by broader width and weaker intensity than pristine GrO ($2\theta = 10.35^\circ$) is due to the defect produced by the introduction of nitrogen atom.

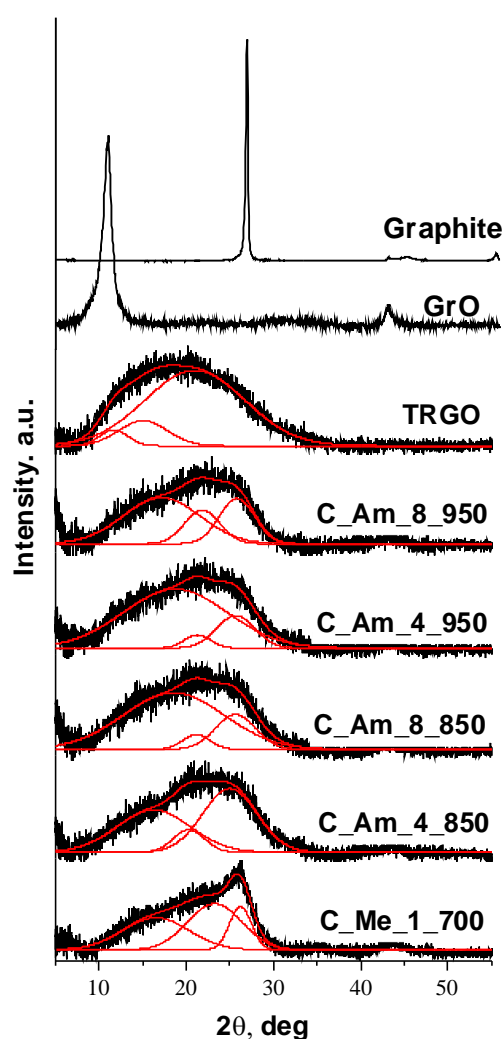


Fig. 18. XRD patterns of precursor, intermediate products and catalysts used in transesterification reaction.

The XRD pattern of TRGO also exhibits a characteristic (002) peak of graphite emerged at 23.55° . Compared with TRGO, it is found that for all catalyst samples the (002) peak moved to higher 2θ values, which indicates that

nitrogen atoms have inserted into TRGO surface structure and resulted the decrease in distance between the graphene layers. The reduction in the interlayer spacing, in this case might be due to ammonia corrosive processes [231] or to the defects in sheet structure [232]. However, considering that nitrogen may enter the graphene basal plane in different ways (graphitic, pyridinic, and pyrrolic) it is also possible that the unequal charges distribution in carbon sheet promote the emergence of attractive forces that increase their mutual interaction [232-234]. Calculated interlayer distance perpendicular to the (002) plane is very similar to that of ideal graphite. The prepared carbon materials are characterized by the low degree of crystallinity as might be suggested by the absence of distinct diffraction patterns. Moreover, the intensity of peaks decreased with increasing pre-treatment temperature suggesting an increase in irregularity of layer structures. This type of structures are presented in SEM micrographs (Fig. 17 d – g) of prepared samples. The only exception is the C_Me_1_700 sample for which the intensity of (002) peak is higher and FWHM is rather lower than that of others catalysts. This indicates the formation of better-ordered structures.

Table 11. The fitting results of XRD patterns performed for TRGO and catalyst samples.

Samples	Peak 1			Peak 2			Peak 3		
	2 θ ; deg	FWHM	Interlayer distance, nm	2 θ ; deg	FWHM	Interlayer distance, nm	2 θ ; deg	FWHM	Interlayer distance, nm
TRGO	12.32	4.60	0.718	16.95	7.60	0.523	23.55	9.25	0.377
C_Am_4_850	16.26	9.88	0.545	20.30	4.21	0.437	25.00	7.33	0.356
C_Am_8_850	18.57	13.61	0.477	21.16	3.68	0.420	25.65	5.46	0.347
C_Am_4_950	18.74	14.03	0.473	21.29	3.53	0.420	25.68	5.21	0.347
C_Am_8_950	17.17	10.33	0.516	21.85	4.78	0.406	25.83	4.75	0.345
C_Me_1_700	16.51	8.99	0.536	23.27	7.32	0.382	26.22	2.95	0.339

BET analysis.

All catalyst samples obtained were subjected to textural analysis whose results are presented in Table 12 and Fig. 19. In Fig. 19 are shown the N₂ adsorption-desorption isotherms and the corresponding pore size distribution curves of GrO, TRGO and catalyst samples. According to the IUPAC classification, the N₂ adsorption-desorption isotherms of the samples were type IV, with hysteresis loops type H3 [235]. A type IV adsorption-desorption isotherm indicates the presence of mesopores, while a type H3 hysteresis loop is correlated with slit-shaped pores, possibly between parallel layers. This result is consistent with the SEM observations.

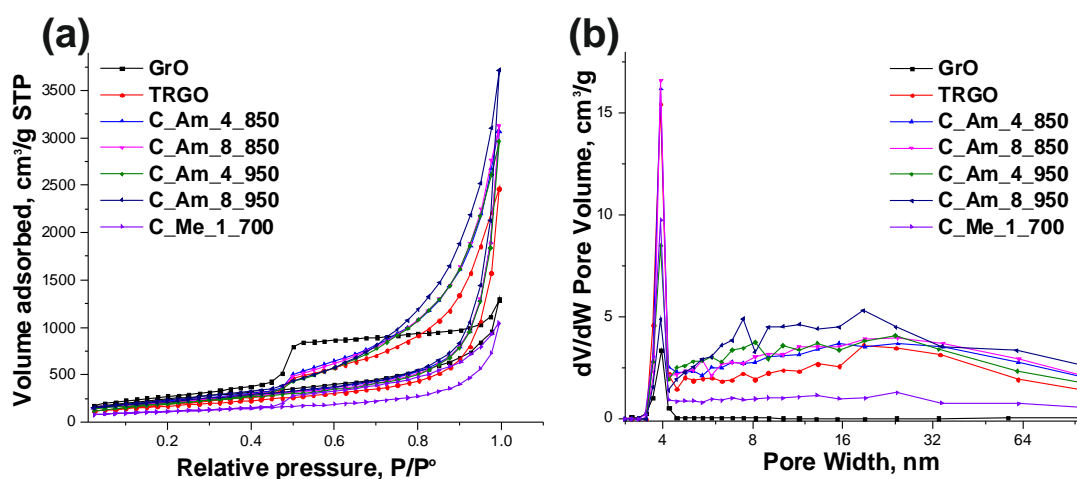


Fig. 19. Nitrogen adsorption-desorption isotherms (a) and the corresponding pore size distribution curves of catalysts used in transesterification reaction (b).

The pore size distribution curves determined by the Barrett–Joyner–Halenda method (Fig. 19 b) display that GrO mainly has a narrow pore-size distribution centered at 3.9 nm. By comparison, in TRGO and catalyst samples (C_Am_4_850, C_Am_8_850 and C_Am_4_950), besides well-developed mesopores centered at 3.9 nm, there is also a relatively broad distribution of pores from 4 nm up to 62 nm. In contrast, the C_Am_8_950 and C_Me_1_700 samples, show a much more narrow pore size distribution up to 35 nm. Moreover, in C_Am_8_950 case, are many pores with pore sizes of 3.94 nm, 7.41 nm and 18.80 nm.

The parameters calculated from nitrogen adsorption measurements are summarized in Table 12.

Table 12. Surface area and pore volume data obtained from nitrogen adsorption measurement.

Samples	S_{BET} ($\text{m}^2 \cdot \text{g}^{-1}$)	S_{ext} ($\text{m}^2 \cdot \text{g}^{-1}$)	V_{tot} ($\text{cm}^3 \cdot \text{g}^{-1}$)	V_{μ} ($\text{cm}^3 \cdot \text{g}^{-1}$)
Graphite	12	11	0.03	0.00
GrO	46	41	0.17	0.00
TRGO	617	617	3.82	0.00
C_Am_4_850	762	762	4.76	0.00
C_Am_8_850	751	751	4.84	0.00
C_Am_4_950	720	720	4.59	0.00
C_Am_8_950	789	789	5.75	0.00
C_Me_1_700	399	399	1.61	0.00

The results obtained prove that all samples studied are meso- and macroporous materials ($V_{\mu} = 0$). As follows from the data, it is clear that after NH_3 treatment at high temperatures, both BET surface area and pore volume of samples increase compared to the pristine carbon material TRGO. The observed increases in these parameters were primarily ascribed to the additional exfoliation from the secondary thermal decomposition of residual oxygen functional groups in TRGO, as supported by the apparent decrease in oxygen content from 11.7 wt % to 3.1 %, 3.3 %, 2.0 %, 1.6 %, respectively (Table 13). Apart from that, partial gasification of the studied catalysts with free radicals that were created during ammonia decomposition can also have a contribution to development of the porous system [236, 237]. It was also noticed that all samples modified with ammonia show similar surface areas and total pore volumes. The highest surface area ($S_{\text{BET}} = 789 \text{ m}^2 \cdot \text{g}^{-1}$), pore volume ($V_{\text{tot}} = 5.8 \text{ cm}^3 \cdot \text{g}^{-1}$) were observed for the C_Am_8_950 sample.

The exception is the C_Me_1_700 sample for which the surface area decrease to $399 \text{ m}^2 \cdot \text{g}^{-1}$. Most probably, such poor results follow from the fact

that the nitrogen groups introduced upon modification have blocked the smallest pores playing the most important role in the porous structure of the carbon samples. This conclusion can be supported by the results of elemental analysis, where it was found that for this sample the nitrogen content is the highest (Table 13).

Elemental analysis and acid/base properties of the surface.

The elemental analysis data of the samples obtained by CHNS analyser (EA) and XPS, and data of total acidity/basicity measurements are given in Table 13. The functionalizations of initial TRGO performed were effective as after each modification the increase in nitrogen content was confirmed by both techniques. Further analysis of EA data presented in Table 13 demonstrates that after pre-treatment TRGO with gaseous ammonia and melamine, the oxygen content has been reduced from 11.7% even up to 1.6%. The decreasing of O % and simultaneous increasing of N % indicate that a portion of residual oxygen sites and lattice defects on TRGO surface are substituted by N-containing functional groups during amination, while another amounts of oxygen species are temperately removed in the form of small molecules (e.g. H₂O, CO and CO₂) [238]. Comparison of the EA results obtained for the samples modified with ammonia at different conditions shows that with increasing temperature and time of treatment the amount of nitrogen incorporated into the carbon surface successively drops from 6.1% to 5.5%, 3.8% and 3.3%, respectively. The decrease in N content could be ascribed to the removal of some unstable N functional groups [234]. The highest nitrogen content (12.1%) was found in sample modified with melamine at 700 °C. The results of current study also showed that the ash content increase at all treatment temperatures, except for C_Me_1_700. The origin of ash may be related to the presence of incombustible substances that can be introduced during the chemical treatment of graphite. The sulphur content was progressively reduced, as the functionalization time and temperature increased and in most samples is on similar level, as detected by both analysis techniques.

Table 13. Element contents of catalyst samples determined by EA and by XPS and total acidity/basicity results (dry basis).

Analysis	Sample	Element content (mass %)							
		Ash (wt%)	C (wt%)	H (wt%)	N (wt%)	S (wt%)	O ^a (wt%)	Total acidity (mmol · g ⁻¹)	Total basicity (mmol · g ⁻¹)
EA ^b	Graphite	0.0	99.7	0.1	0.0	0.0	0.2	0.04	0.06
	GrO	1.5	51.0	2.3	0.1	1.8	43.3	3.74	0.00
	TRGO	1.5	83.3	1.2	0.3	2.0	11.7	0.83	0.00
	C_Am_4_850	2.2	87.8	0.7	6.1	0.1	3.1	0.06	0.72
	C_Am_8_850	2.2	87.8	1.1	5.5	0.1	3.3	0.04	0.75
	C_Am_4_950	3.2	90.0	0.9	3.8	0.1	2.0	0.00	0.69
	C_Am_8_950	3.9	90.5	0.6	3.3	0.1	1.6	0.02	0.77
	C_Me_1_700	1.5	81.3	0.8	12.1	0.5	3.8	0.22	0.21
XPS ^c	TRGO	-	82.6	-	0.0	2.6	14.8	-	-
	C_Am_4_850	-	92.5	-	3.4	0.0	4.1	-	-
	C_Am_8_850	-	90.6	-	3.6	0.0	5.8	-	-
	C_Am_4_950	-	84.8	-	2.0	0.0	13.2	-	-
	C_Am_8_950	-	90.8	-	1.9	0.0	7.2	-	-
	C_Me_1_700	-	85.5	-	9.5	0.0	5.0	-	-

^a Calculated by difference; ^b Bulk element content determined by CHNS analyser; ^c Surface element content determined as mass percentages based on the areas of the respective peaks in the high-resolution XPS spectra (atomic contents) and the respective atomic masses.

The XPS mass percentages show differences relatively to EA results. The significantly lower N% in XPS relatively to EA can be justified since XPS is a much more surface sensitive technique (covering 10 nm deep from the surface) while EA is a bulk analysis. No essential differences are noted between the surface and the bulk content of carbon. As follows from analysis of the data, the mass % values of oxygen, obtained by XPS are greater than those from elemental analysis. This fact shows that residual oxygen functional groups are predominantly on the edges of TRGO than in the bulk.

The acid/basic character of the catalysts, assessed by the potentiometric titration, show that pre-treatment with ammonia changed the acidic character of TRGO to basic ones. It was also noticed that for most samples the longer time and higher the temperature of treatment used, the greater amount of the surface functional groups of basic character was introduced. By comparing the catalyst samples one can see that the C_Me_1_700 stands out from the others. The basicity of the catalyst treated with melamine is more than 3 times lower than in the case of other. This is surprising, as the nitrogen content is four times (compare with C_Am_8_950) and twice (compare with C_Am_4_850) as high as in melamine treated sample. Moreover, some acidic groups are formed, possibly of pyrrole type (see XPS data).

Thermal analysis.

The thermal stability of the prepared catalysts, graphite, GrO and TRGO was evaluated by TG analysis and is depicted in Fig. 20. As shown in Fig. 20 a, the graphite powder exhibited a high thermal stability with a lower weight loss of 1% up to 700 °C. However, the thermal stability of GrO was decreased due to the labile oxygen functional groups. The TG analysis curve of GrO shows two sharp weight losses, one around 100 °C and the other around 200 °C, which are attributed to the evaporation of water and the decomposition of labile oxygen containing functional groups, yielding CO, CO₂, and steam [239]. The gradual weight loss above 250 °C is attributed to the removal of more stable oxygen functionalities (such as phenol, carbonyl and quinone), which usually

decompose at higher temperatures [240]. After the reduction, most of the oxygen containing groups on the GrO surface were removed, so the derived TRGO had less weight loss.

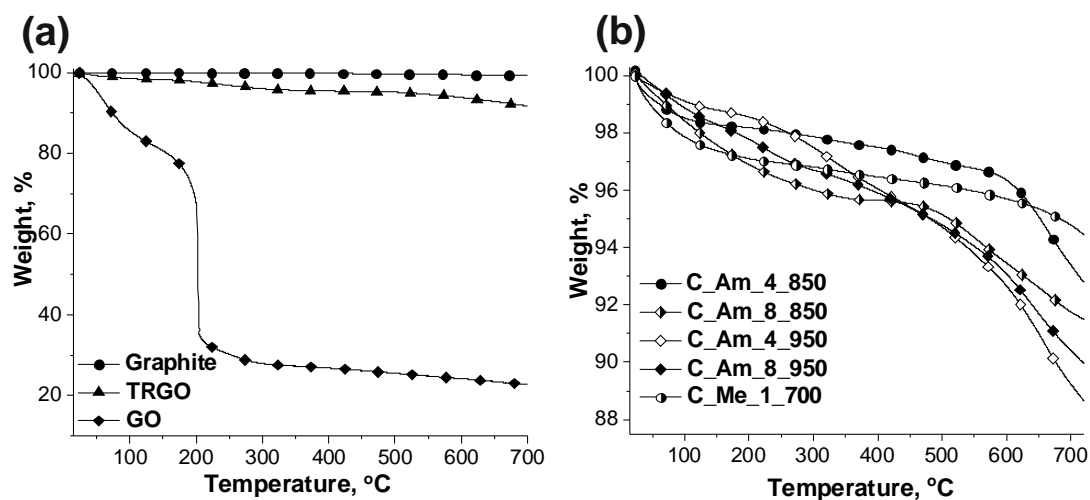


Fig. 20. TG analysis of graphite, intermediate products and catalyst samples.

The TG analysis results of catalyst samples are shown in Fig. 20 b. The decomposition processes of different functionalized TRGO occurred through two main weight loss stages. The first stage ($\sim 100^\circ\text{C}$) can be assigned to the removal of moisture, and the second stage in the temperature range of $100\text{--}700^\circ\text{C}$ may be ascribed to the pyrolysis of covalently-bonded functional groups on the TRGO surface. Moreover, the C_Me_1_700 sample exhibited the greatest thermal stability up to 700°C with slightly lower weight loss ($\sim 5\text{ wt}\%$) than other catalysts.

FTIR spectroscopy.

Fig. 21 shows the FT-IR spectra of graphene-based catalysts. The spectra of GrO and TRGO, which were already discussed in 3.1.1. section, are also shown for comparison. It should be mentioned that graphene-based catalysts exhibit similar spectra, which may reflect similar surface composition of these materials. Two main peaks were detected in the spectra of all catalysts samples and TRGO. The broad band centered at 1200 cm^{-1} can be mainly assigned to aromatic C–N and/or C–O stretch vibrations, while the broad band around

1573 cm^{-1} are assigned to aromatic C=N bonds or C=C stretching [241-243]. The relative weak signal centered at 3430 cm^{-1} can be ascribed to either -OH, -NH₂ or =NH groups in the aromatic ring [244]. These results suggest that a certain amount of N-containing functional groups should be present in graphene-based catalysts.

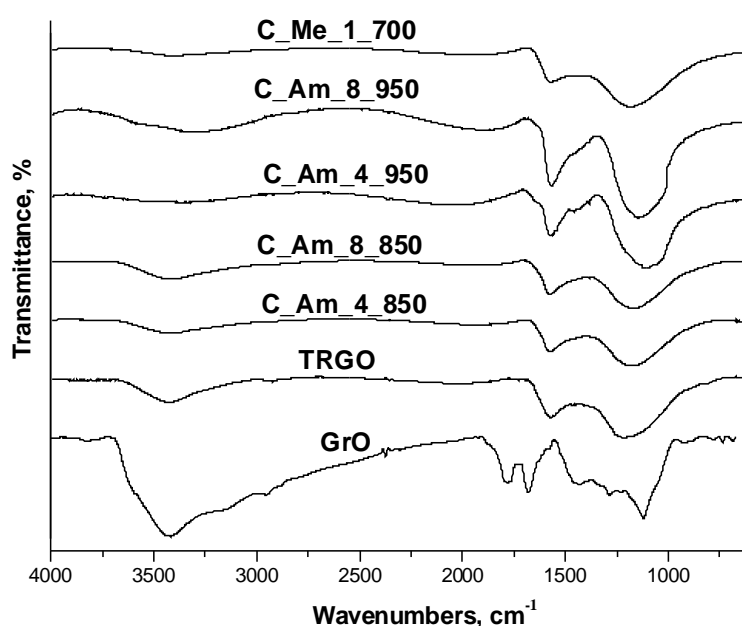


Fig. 21. FTIR spectra of intermediate products and catalysts used in transesterification reaction.

XPS analysis.

Further information about the nitrogen functionalities was provided by deconvolution of the C1s, and N1s core-level XPS spectra (Fig. 22, Fig. 23 and Table 14). Peak fitting of C1s high resolution spectra reveals the various carbon components in catalysts framework. As shown in Fig. 22 a, the C1s XPS spectrum of TRGO is consisted of four types of carbon: the C=C (284.3 eV), C-C (285.6 eV), C-O (287.2 eV), C=O/O-C=O (288.4 eV) [219, 220]. After pre-treatment of TRGO with NH₃ or melamine, all samples obtained exhibit the same graphitic C=C peak whose concentration decreases due to the appearance of new bands. Notably, a new peak was formed at 286.9 eV (in case of C_Am_4_850), 286.5 eV (in case of C_Am_8_850), 286.4 eV (in cases of

C_Am_4_950 and C_Am_8_950), 286.7 eV (in case of C_Me_1_700), which would be caused by the new C=N interaction [245]. Moreover, when nitrogen is introduced, the bonds at 287.2 eV and 288.4 eV are slightly shifted and the concentration of these bands is increased from 3.2 % to 7.7%, 4.9%, 4.2% and from 1.1% to 3.5%, 5.2%, 2.4%, respectively. These peaks are ascribed both to C-O/C-N and C=O/O-C=O/C=N bonds, respectively, and are generally considered as evidence that nitrogen is successfully incorporated into the carbon framework [246]. This shift is also in agreement with increased structural disorder due to the disruptions in the sp^2 carbon framework from the incorporation of nitrogen. In addition, the disappearance of C-O peak in C_Am_4_850 and C_Am_8_850 samples and C=O/O-C=O species in the cases of C_Am_4_950 and C_Am_8_950 suggests selective replacement of the hydroxyl, epoxy, carbonyl or carboxyl groups with a nitrogen functional groups. Moreover, the shake-up satellite peak due to $\pi-\pi^*$ transitions in aromatic rings are observed in prepared samples whereas no $\pi-\pi^*$ interactions are observed in TRGO [247].

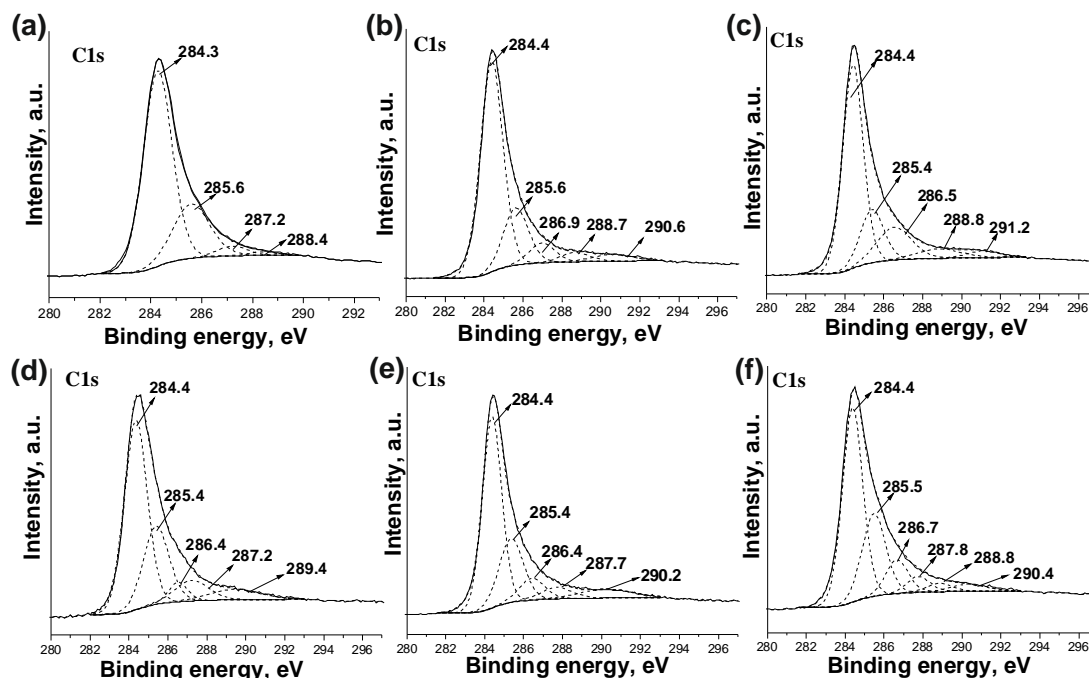


Fig. 22. C1s XPS spectra of TRGO and catalyst samples. a – TRGO, b – C_Am_4_850, c – C_Am_8_850, d – C_Am_4_950, e – C_Am_8_950, f – C_Me_1_700.

Table 14. Analysis of high resolution XPS spectra of catalysts obtained.

Sample	BE, eV (concentration of species, at %)										
	C 1s				N1s						
	C=C	C-C	C=N	C-O, C-N	C=O, C=N, O-C=O	π - π^*	N-C sp ³	C-N=C	C-NH ₂ , C-N-C (pyridone type)	C-NH-C	C-N-C (graphitic type)
TRGO	284.3 (61.2)	285.6 (21.8)	-	287.2 (3.2)	288.4 (1.1)	-	-	-	-	-	-
C_Am_4_850	284.4 (60.9)	285.6 (18.5)	286.9 (6.6)	-	288.7 (3.5)	290.6 (3.5)	397.9 (1.3)	398.8 (0.5)	399.5 (0.4)	400.5 (0.8)	-
C_Am_8_850	284.4 (52.9)	285.4 (16.0)	286.5 (14.5)	-	288.8 (5.2)	291.2 (1.8)	397.4 (0.4)	398.2 (1.4)	399.5 (0.6)	400.6 (0.8)	-
C_Am_4_950	284.4 (47.1)	285.4 (21.9)	286.4 (4.6)	287.2 (7.7)	-	289.4 (5.6)	397.3 (0.4)	398.2 (0.8)	399.5 (0.3)	400.9 (0.4)	-
C_Am_8_950	284.4 (50.1)	285.4 (21.2)	286.4 (7.6)	287.7 (4.9)	-	290.2 (6.3)	397.4 (0.1)	398.3 (0.7)	-	400.0 (0.5)	402.1 (0.3)
C_Me_1_700	284.4 (46.1)	285.5 (22.6)	286.7 (8.8)	287.8 (4.2)	288.8 (2.4)	290.4 (3.1)	397.6 (0.7)	398.3 (4.1)	399.5 (0.7)	400.5 (2.9)	-

Careful analysis done by deconvolution of the N1s spectra in Fig. 23 shows the presence of several different nitrogen containing groups in all catalysts.

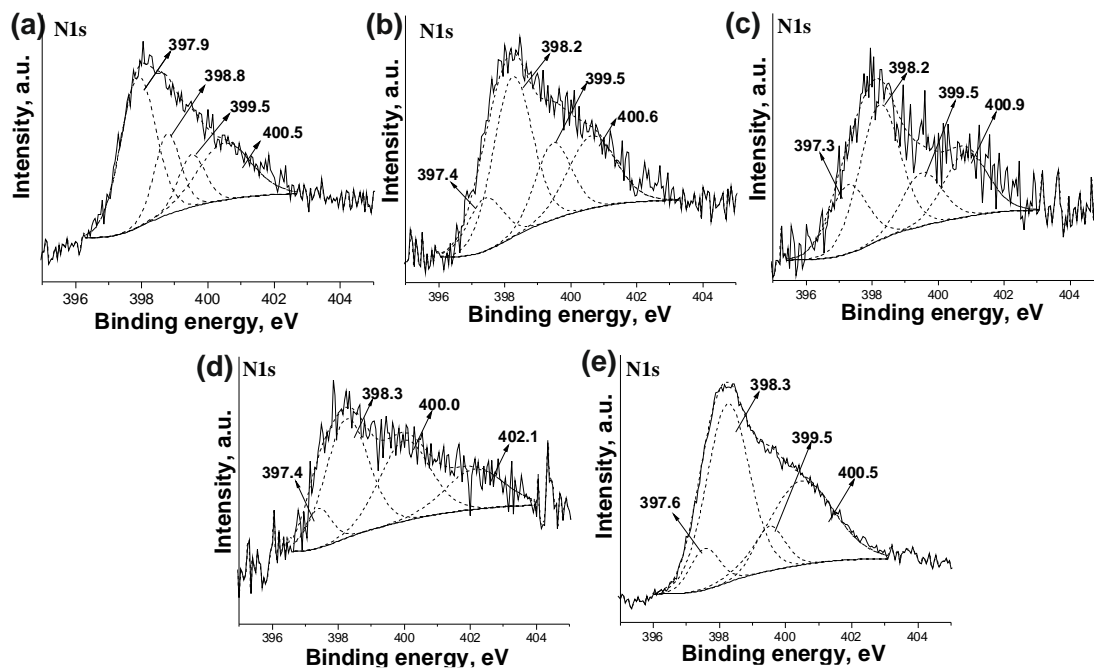


Fig. 23. N1s XPS spectra of catalysts samples: a – C_Am_4_850, b – C_Am_8_850, c – C_Am_4_950, d – C_Am_8_950, e – C_Me_1_700.

According to the existing literature data, the high resolution N1s spectra of C_Am_4_850 (Fig. 23 a) can be deconvoluted into four peaks at binding energies of 397.9 eV, 398.8 eV, 399.5 eV and 400.5 eV, corresponding to N-C sp^3 , pyridinic N, aminic or pyridone N and pyrrolic N respectively [248-250]. It seems that some nitrogen atoms enter the inner layer of C_Am_4_850 through the defects of the outer layer and bond with the sp^3 carbon [248]. These four peaks are also present in the XPS spectra of other catalysts (Fig. 23 b, c, d, e). The exception are C_Am_8_950 (Fig. 23 d) for which aminic or pyridone N completely disappeared and new peak at 402.1 eV assigned to graphitic N appeared [247]. Moreover, the results show that, the most pronounced peaks in all catalysts (except C_Am_4_850) is attributed to pyridinic-N and pyrrolic-N. These functionalities are responsible for the more pronounced basic character of the nitrogen functionalized carbon. Whereas N-C sp^3 is the dominant peak in C_Am_4_850. The different concentrations of the N-configurations indicate that

the formation of nitrogen doped catalysts rich in one N-configuration can be controlled by adjusting the functionalization time and temperature. Reasonably, at relatively high treatment temperature, the distribution of nitrogen in graphene sheets was governed by the balance between nitrogen removal/doping due to the high temperature treatment and/or the reconstruction of nitrogen among different sites.

3.1.4. Activity of solid basic catalysts

The modified graphene based catalysts were tested in transesterification reaction of rapeseed oil with methanol. The yields of fatty acid methyl esters (FAME) obtained in the above process are given in Fig. 24.

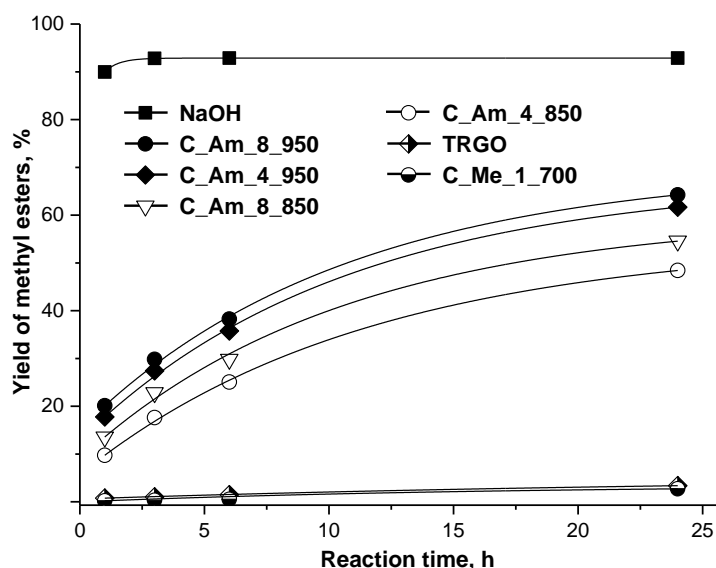


Fig. 24. Comparison of FAME yields obtained for the graphene-based catalysts and commercial catalyst.

For comparison purposes the yield obtained with the use of commercial basic catalyst NaOH is also presented. As depicted in Fig. 24, the yield of FAME clearly increased with increasing reaction time and reached a plateau after 24 h, regardless of the used catalytic system (after this time the product yield increased only slightly). The results presented indicate that the catalysts investigated have the activity (which can be defined by FAME yield) in the range of 2 to 65%. It is clearly visible that the sample functionalized with ammonia at 950 °C for 8 h

(C_Am_8_950) shows the best catalytic activity. After 24 h of reaction, the yield of FAME obtained using this catalyst was up to 65%. However, this result is worse than that attained for commercial catalyst NaOH (93% after 24 h). For other samples modified with ammonia the activity generally grows with increase in amination temperature and time (48% for C_Am_4_850, 55% for C_Am_8_850 and 62% for C_Am_4_950). It is also important to note that catalytic activity of samples is not directly associated with total nitrogen content of the carbon materials but is dependent on the kind of nitrogen moieties and their basicity. Consequently FAME yield of C_Am_8_950 is higher than that of other catalysts although there is decrease in total nitrogen content with increasing modification temperature (but this sample shows the highest basicity, see Table 13). However, more work is still required in order to clarify the concrete role of nitrogen containing functional groups for the transesterification reaction. The surface properties of catalysts such as specific surface area and pore volume are also quite important. As shown in Table 12, C_Am_8_950 has a larger surface area ($789 \text{ m}^2 \cdot \text{g}^{-1}$) and higher total pore volume ($5.75 \text{ cm}^3 \cdot \text{g}^{-1}$) than those of others catalysts, which may be more convenient for reactants to adsorb on the catalyst surface and approach to the active basic sites. The lowest yield of FAME (2.7%) was obtained for the sample modified with melamine. According to the literature [91] and [251], transesterification reactions are catalyzed both by acids and bases. However, the content of both remaining acidic oxygen-containing groups and basic nitrogen functional groups in this sample is very low, as observed by acid–base titration (Table 13). This result demonstrates that the synthetic route used for the covalent grafting of nitrogen functional groups plays a key role in the catalytic activity of the synthesized material. It should be pointed out that the basic catalysts were in general less active than the acidic ones (see Fig. 16). The main reason could be attributed to the parallel reaction between FFA and the basic catalysts, where the FFA in the raw oil (6.4 g/100 mL) predominantly react with the basic catalysts to form soap and water. According to the literature, acidic catalysts are less sensitive to FFA [92].

3.2. Graphene-based nanocomposite material containing (SCN)_n as highly efficient electrocatalyst for ORR

The second part of experimental work was devoted to prepare a novel graphene-based nanocomposite material in order to fabricate superior metal-free catalyst for oxygen reduction. The nanocomposite was synthesized by a facile and cost-effective solid-solid reaction between GrO and KSCN, where the thiocyanate fragments undergo polymerization. The structure of polythiocyanogen (SCN)_n in this nanocomposite was compared to the structure of (SCN)_n prepared by different routes: in solid-solid reaction between KSCN and (NH₄)₂S₂O₈ and during the thermal polymerization of thiocyanogen (SCN)₂.

3.2.1. Structural characterizations

Size exclusion chromatography.

The molecular weight of polythiocyanogen synthesized as AS/A product was determined by size exclusion chromatography to find the mean number average molecular weight (M_n), mean weight average molecular weight (M_w) and polydispersity index of (SCN)_n. An elugram of SEC for the (SCN)_n is shown in Fig. 25.

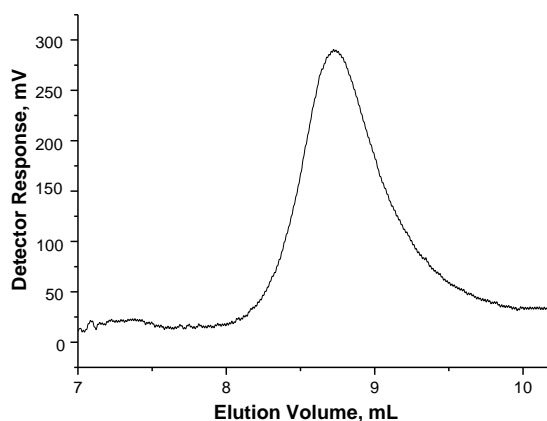


Fig. 25. SEC chromatogram of polythiocyanogen SS/A.

The main fraction of the (SCN)_n is eluted between 8 and 10 mL with a maximum at 8.73 mL. This maximum is attributed to high amounts of long chain polythiocyanogen. The elugram of (SCN)_n is converted to a distribution of

molecular weights along with the rankings of the various average molecular weights in Fig. 26.

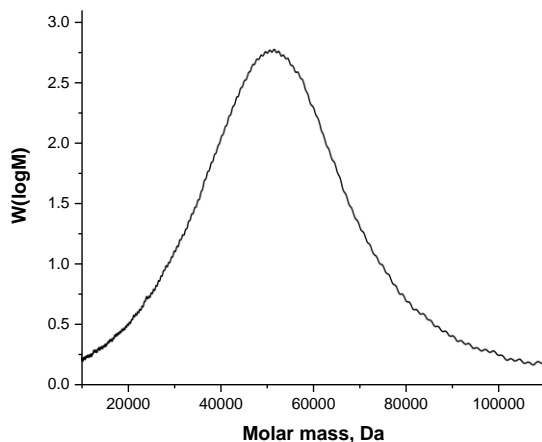


Fig. 26. A distribution of molecular weight of $(\text{SCN})_n$ along with the rankings of the various average molecular weight.

It is possible to observe that the molecular weight distribution ranges from approximately 20000 Da to 90000 Da, with maximum peak intensity at 53198 Da, coincident with polythiocyanogen fractions. The molecular masses of $(\text{SCN})_n$ computed by the SEC software were $M_n = 53759$ and $M_w = 56384$ with a polydispersity index $M_w/M_n = 1.049$. The results of SEC analysis demonstrates that the polythiocyanogen is monodisperse and polymer nature, containing narrow unimodal peak.

Powder X-ray diffraction analysis.

XRD patterns have been customarily used to characterize the phases present in the reactant mixture and provide a means of identification of products, solid reactants and intermediates, as well as to assess the crystalline order of the solid sample. Polythiocyanogen synthesized by different methods, as well as pure reactants and their mixtures were examined using a powder XRD method. The XRD patterns of initial reactants are compared using data from JCPDS database. The XRD patterns of SS/A samples and their precursors are presented in Fig. 27 a.

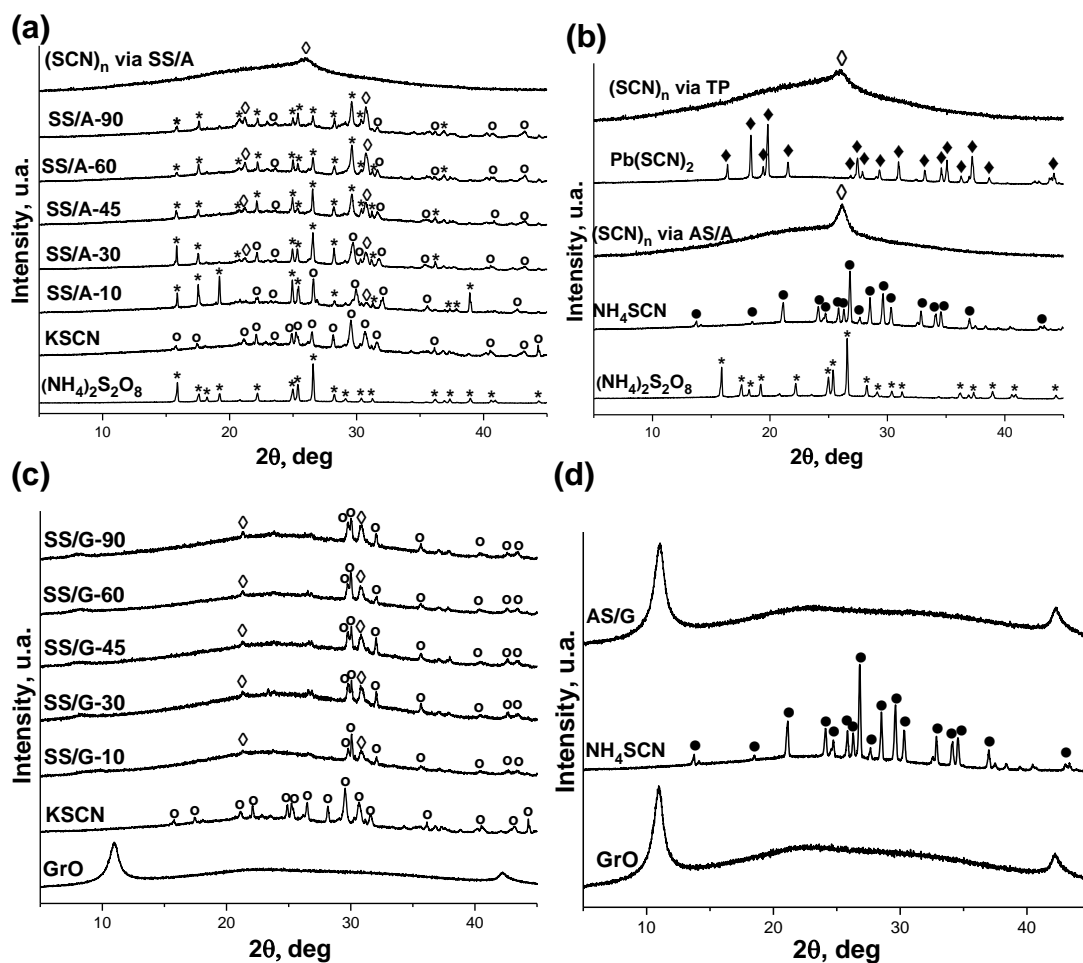


Fig. 27. X-ray powder diffraction pattern of ammonium peroxodisulfate (*) (a, b), potassium thiocyanate (o) (c), $(\text{SCN})_n$ produced via SS/A reaction (\diamond) (a), ammonium thiocyanate (\bullet) (b, d), lead thiocyanate (\blacklozenge) (b), and $(\text{SCN})_n$ produced via AS/A and TP reactions (\diamond) (b). X-ray powder diffraction pattern of GrO, KSCN (o), and SS/G products (c). New-appeared peaks of graphite (002) (*) and $(\text{SCN})_n$ (\diamond) are also marked. X-ray powder diffraction pattern of GrO, ammonium thiocyanate (\bullet), and AS/G product (d).

Fig. 27 a reveals that at the start of the reactions the pattern composed of a combination of KSCN and $(\text{NH}_4)_2\text{S}_2\text{O}_8$ is obtained. After some time, the intensity of the reflections of precursors' decreases, and a new set of reflections appear. The new-appeared reflections can be assigned to the crystalline structure of polymerized trithiocyanuric acid [197] (Fig. 7 d, structure 1). Finally, the only set of reflections remaining with a broad diffraction peak position at about $2\theta = 26.42^\circ$ is that of the product (Fig. 27 a). A broad diffraction peak at this

position characteristic to amorphous structure of $(\text{SCN})_n$ is confirmed by the other authors [197, 198, 201]. Hence, an assumption can be made that either changes occur in the structure of $(\text{SCN})_n$ during the washing procedure, or some of the existing phases obtained in SS/A are stable only in the contact with the precursor crystals.

The XRD patterns of samples AS/A and TP and their precursors respectively are presented in Fig. 27 b. Fig. 27 b demonstrates that the XRD pattern of $(\text{SCN})_n$ obtained from different precursors and by different routes are very similar and are characterized by unique broad reflection at about $2\theta = 26.42^\circ$, as well as in the case of the synthesis of SS/A.

The XRD patterns of SS/G samples and their precursors are presented in Fig. 27 c. The pristine GrO powder showed a characteristic peak at $2\theta = 10.97^\circ$, corresponding to a d-spacing of 0.806 nm. After the grinding for 10 min GrO with KSCN (Fig. 27 c), the characteristic peak of GrO at $2\theta = 10.4^\circ$ disappeared while three peaks at 21.3° , 26.5° and 30.8° appeared. The peak at 26.5° was attributed to the graphite lattice plane (002) (JCPDS, No. 00-056-0159). The two remaining peaks coincide with these of $(\text{SCN})_n$ in Fig. 27 c respectively. The obtained results evidence the reaction between GrO and KSCN which leads to the reduction of GrO and formation of polythiocyanogen. Fig. 27 d shows the result of reaction between GrO and NH_4SCN in aqueous solution. Analyzing the XRD pattern a conclusion could be done that under these conditions the reaction between GrO and NH_4SCN does not occur.

SEM analysis.

The morphology of prepared composite samples was examined by SEM technique (Fig. 28).

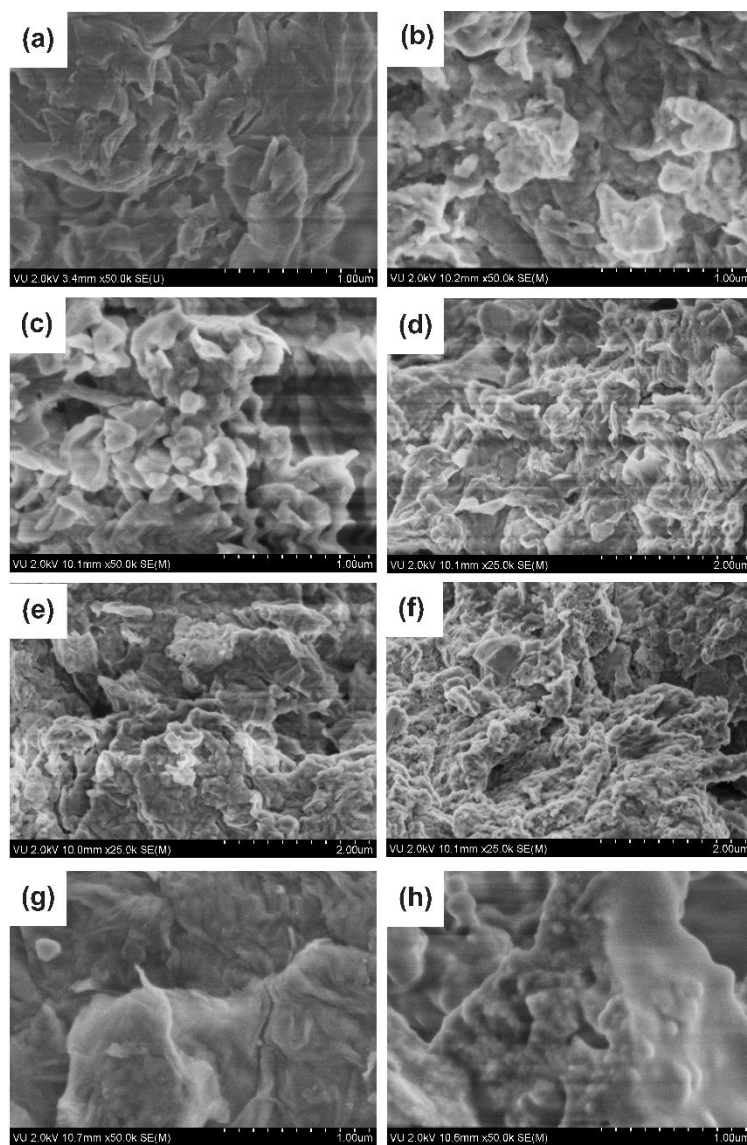


Fig. 28. SEM micrographs of GrO (a), SS/G samples: SS/G-10 (b), SS/G-30 (c), SS/G-45 (d), SS/G-60 (e), SS/G-90 (f), SS/A-90 (g) and (SCN)_n via TP (h).

SEM images reveal characteristic platelet structure of GrO (Fig. 28 a). During the solid-solid reaction between KSCN and GrO, the morphology is changed to a more curled structure (Fig. 28 b, c, d, e). The longer is the solid-solid reaction time, the more irregular and curled structure is obtained. A possible explanation of this might be that the solid-solid reaction occurs on the edges of GrO sheets leading to a formation of the wrinkles on the edges of GrO platelets. The SEM results are in line with the XRD study of SS/G samples (Fig. 28 c), because the SEM images of SS/A and TP samples confirm the absence of crystallinity, as it was stated from the XRD data (Fig. 28 g, h and Fig. 27 a, b).

FTIR spectroscopy.

FTIR spectroscopy has been used to assess the changes in the reaction mixtures and evaluate the formation of new chemical bonds (Fig. 29).

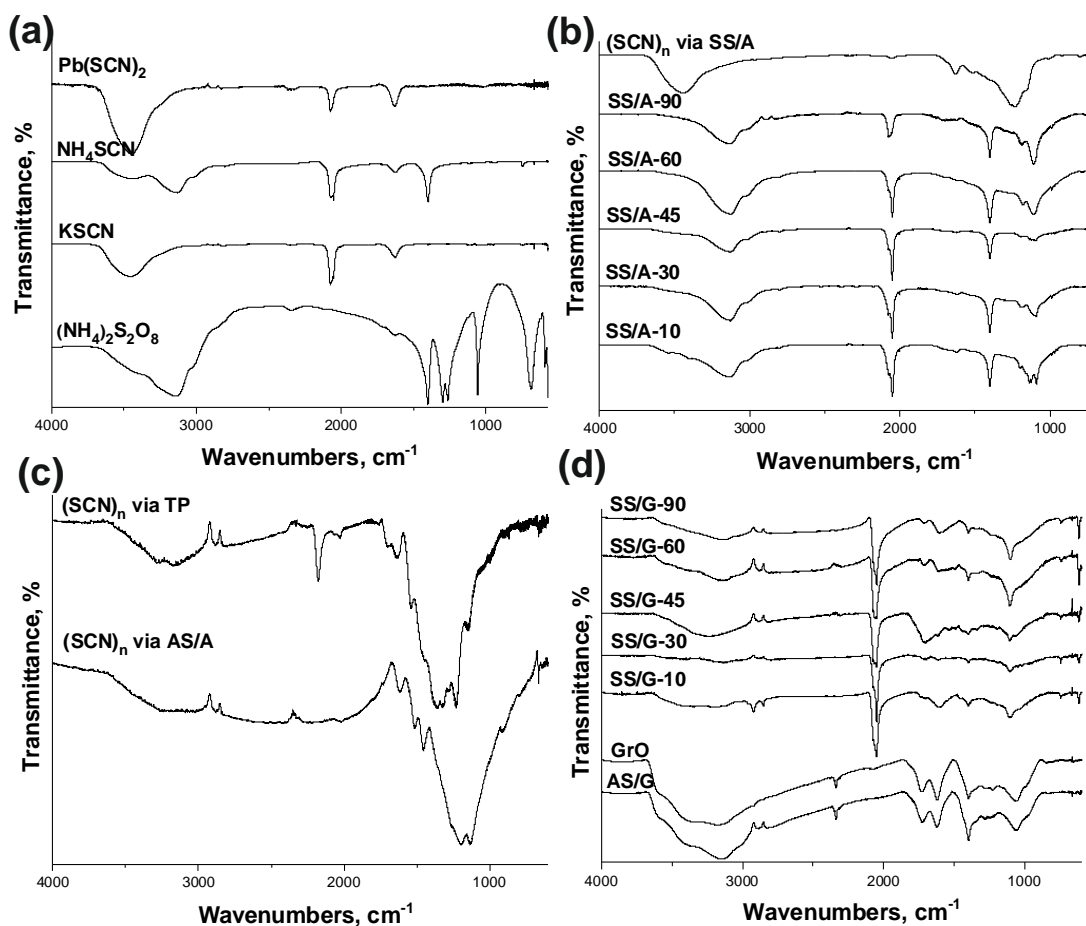


Fig. 29. FTIR spectra of precursor materials (a), and products obtained via synthesis of SS/A (b). FTIR spectra of (SCN)_n obtained via synthesis of AS/A (c) and via synthesis of TP (c). FTIR spectra of products obtained via synthesis of SS/G (d) and AS/G (d).

Fig. 29 a illustrates the FTIR spectra of precursors ((NH₄)₂S₂O₈, KSCN, NH₄SCN and Pb(SCN)₂). The spectrum of KSCN is characterized by the strong absorption peak at 2065 cm⁻¹ due to the C≡N stretching vibration of SCN⁻ ions; the same peaks are observed for NH₄SCN and Pb(SCN)₂. The FTIR spectrum of (NH₄)₂S₂O₈ displays a broad peak at 3043 – 3369 cm⁻¹ corresponding to the stretching frequency of NH₄⁺. The same peak is observed for NH₄SCN. The

strong absorption peaks at 1400 cm^{-1} , $1298 - 1264\text{ cm}^{-1}$, 1056 cm^{-1} and 690 cm^{-1} are attributed to the stretching frequency of the $\text{S}_2\text{O}_8^{2-}$ ions [252].

Fig. 29 b shows the FTIR spectra of SS/A products. Obviously, in the SS/A product washed free from precursor ions, the $\text{C}\equiv\text{N}$ stretching band at 2065 cm^{-1} is disappeared and very broad strong band centered at 1243 cm^{-1} is appeared. The spectrum closely matched the FTIR spectrum reported for $(\text{SCN})_n$ in the literature [198]. The strong, broad band around 1243 cm^{-1} is due to $-\text{C}-\text{N}=\text{}$ stretching, the band at 1516 cm^{-1} is due to $=\text{C}=\text{N}-$ conjugated vibration, and signal at 1630 cm^{-1} is due to symmetric and asymmetric stretching of the $=\text{C}=\text{N}-$ group.

FTIR spectra of polythiocyanogen obtained via the thermal polymerization (TP) and oxidation of NH_4SCN with $(\text{NH}_4)_2\text{S}_2\text{O}_8$ in aqueous media (AS/A) are presented in Fig. 29 c. The broad band centered in the spectrum of $(\text{SCN})_n$ obtained via AS/A at $\sim 1290\text{ cm}^{-1}$ together with peaks at 1550 cm^{-1} and 1650 cm^{-1} are similar to those observed in Fig. 29 b for $(\text{SCN})_n$ (SS/A) washed free from precursor ions. Apparently, the FTIR spectra of $(\text{SCN})_n$ obtained by different ways have similar features but do not coincide, indicating some structural differences. Nevertheless, the constant presence of $-\text{C}=\text{N}$ and $=\text{C}=\text{N}-$ bonds and thus of polyazomethine chains is evident in all cases.

The FTIR spectra of GrO, SS/G and AS/G products are shown in Fig. 29 d. The characteristic GrO bands are observed at 1061 cm^{-1} (C–O stretching vibrations of epoxy groups), 1230 cm^{-1} (C–O stretching vibrations of phenolic C–OH), 1405 cm^{-1} (O–H deformation vibrations of tertiary C–OH) and 1726 cm^{-1} (C=O stretching vibrations of COOH groups). The peak at 1621 cm^{-1} is related to the C=O stretching mode in quinone group and C=C stretching in small size conjugated domains. The broad peak at 3237 cm^{-1} corresponds to O–H stretch [253].

In Fig. 29 d, the FTIR spectrum for AS/G product, which results from the reaction between GrO and NH_4SCN in aqueous solution (AS/G), is very similar to the spectrum of GrO, confirming that this reaction does not occur, as previously observed by XRD (Fig. 27 d). The FTIR spectra of SS/G products

(Fig. 29 d) show that dependent on the duration of solid-solid reaction between KSCN and GrO, some peaks disappear or decrease in intensity, while other peaks appear. Thus, in the region $\sim 1100\text{ cm}^{-1}$ a peak of epoxy group in GrO disappears, and after the reaction with KSCN appears a new peak at 1170 cm^{-1} . Similarly, the peaks at 1621 cm^{-1} (quinone) and 1726 cm^{-1} ($-\text{C}=\text{O}$ in carboxyl-group) disappear, and new peaks appear at 1530 and 1630 cm^{-1} . All these new-appeared peaks can be attributed to the vibrations in $-\text{C}=\text{N}-$ conjugated group. The appearance of the peak at 1530 cm^{-1} can also be ascribed to the presence of $\text{C}=\text{C}$ stretching in extended conjugated bonds in accordance with the reduction of GrO to graphite structures and confirming the XRD results [240].

Thermal analysis.

The TG/DTG analysis of GrO and SS/G samples was performed to elucidate their thermal stability and chemical composition. The results are shown in Fig. 30. Little differences is observed between the thermal behaviour of different SS/G samples. Mass loss of GrO is $\sim 75\%$ at $800\text{ }^\circ\text{C}$, while for SS/G products this parameter reaches $\sim 55\%$. These results support previous assumption about the reduction of GrO during the solid-solid reaction with KSCN. Another interesting finding is a much more pronounced peak in DTG curves of SS/G products in comparison with GrO at $\sim 50\text{ }^\circ\text{C}$, which is usually attributed to the loss of adsorbed water [60]. The peak at $50\text{ }^\circ\text{C}$ decreases slightly with the increasing the duration of solid-solid reaction. The solid-solid reaction between GrO and KSCN should be of topological nature. During the short time the reaction takes place on the edges of GrO sheets, but the reduction of GrO occurs in only a small extent. The extent of reduction increases with an increase of the reaction time. Most probably, the SS/G products with short fragments of $(\text{SCN})_n$ on the edges of the sheets are highly favorable for the adsorption of water. It can thus be suggested that such relatively loose layered structure should be favorable for the adsorption of ions and gaseous products during the ORR reaction.

The second mass loss at near 200°C can be ascribed to the release of CO₂ from carboxylic acid groups and CO from the decomposition of epoxide and alcohol groups. Phenolic or quinone groups decompose at higher temperatures, above 800 °C and occur out of the monitored temperature range [240]. Studies on GrO based materials by Temperature Programed Desorption, with identification of mass fragments by mass spectrometry, showed mass loses corresponding to release of CO₂ and CO groups at near 250°C or at lower temperatures depending on the functionalization or on the interlayer distance [240].

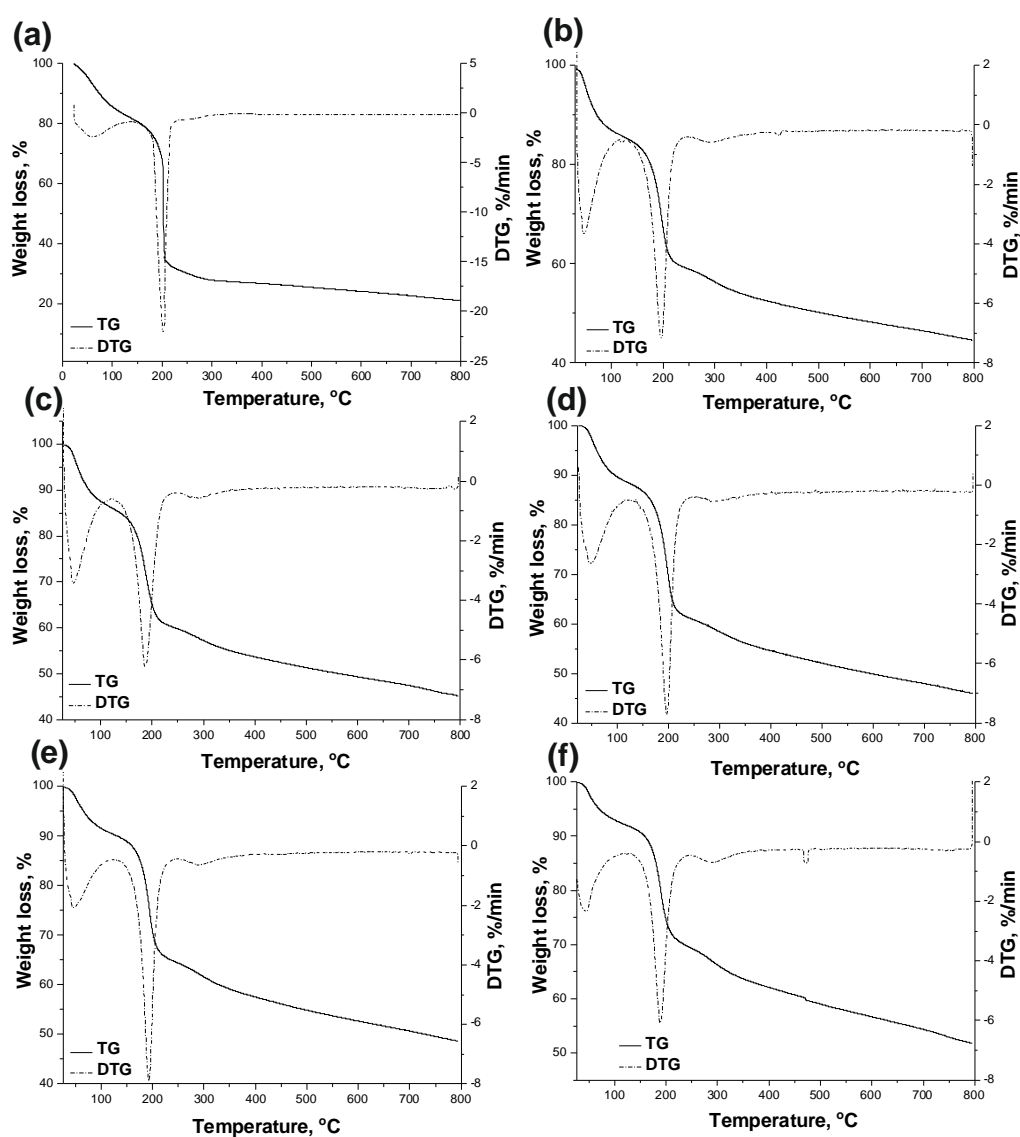


Fig. 30. TG and DTG curves of GrO (a) and SS/G samples: SS/G-10 (b); SS/G-30 (c); SS/G-45 (d); SS/G-60 (e) and SS/G-90 (f).

XPS and elemental analysis.

The element contents (mass %) of GrO and SS/G products by obtained by CHNS/O EA and XPS are given in Table 15.

Table 15. Element contents of GrO and SS/G nanocomposites obtained by EA and by XPS.

Analysis	Sample	Element content (mass %)					
		C	O	N	S	H	K
EA ^a	GrO	45.8	49.8	0.0	1.6	2.7	
	SS/G-10	45.0	48.8	0.8	2.7	2.7	
	SS/G-30	44.9	49.3	0.7	2.4	2.7	
	SS/G-45	45.0	49.0	0.8	2.5	2.6	
	SS/G-60	44.8	49.2	0.8	2.6	2.7	
	SS/G-90	44.6	49.3	0.8	2.6	2.7	
XPS ^b	GrO	63.9	31.2	1.5	3.4		n.d.
	SS/G-60	61.7	30.1	0.9	1.6		5.7

^a Bulk element content determined by CHNS/O analyser;

^b Surface element content determined as mass percentages based on the areas of the respective peaks in the high-resolution XPS spectra (atomic contents) and the respective atomic masses;

n.d. – not detected.

The EA mass percentages show differences relative to XPS results. The significantly lower O% in XPS relatively to EA can be justified by the typical presence of water interlocked between the sheets of GrO, in amounts of ~20% [63], whereas the samples for XPS analysis were submitted to vacuum degassing for long periods until achievement of ultra-high vacuum conditions required for analysis. Thus the release of interstitial water is obtained and consequently the O% observed by XPS is lower and the percentages of the other elements (C, N, S) are higher.

The presence of N and S elements in the pristine GrO material is ascribed to the use of sulphuric acid and sodium nitrate during the GrO preparation and related groups can remain retained at the surface. After solid-solid reaction, the mass % of N and S increase in EA analysis and decrease in XPS analysis. This can be justified since XPS is a surface analysis (covering 10 nm deep from the surface) while EA is a bulk analysis and functional groups can be selectively leached from the surface during the solid-solid reaction and washing procedures.

After solid-solid reaction, the mass % of N and S elements are identical for both techniques: EA (0.8% and 1.1%, for N and S respectively, after subtraction of the S% from pristine GrO) and XPS (0.9% and 1.6%, for N and S respectively). This fact, as well as, the relative low loadings of these elements confirm the idea that the reaction of $(\text{SCN})_n$ formation should occur basically on the edges of GrO [219]. The N:S atomic ratio is ~ 1 .

One other observation from the EA analysis of materials resulting from different reaction times is that during the first 10 min of solid-solid reaction between GrO and KSCN, the amounts of N and S elements increases rapidly but are nearly maintained for longer reaction times. It can be concluded that this reaction is fast.

From both techniques, it can also be observed that the O% slightly decreases upon solid-solid reaction, this confirms the reduction of GrO to graphite, previously pointed-out.

The XPS survey spectra of the material SS/G-60 indicated the presence of potassium (5.7%), which probably remains deposited as counter-ion in deprotonated oxygen groups. The XPS analysis of a PTC film formed over a platinum electrode from a KSCN solution also showed the presence of potassium [254].

Data obtained from the high resolution spectra in the relevant regions are presented in Fig. 31 and Table 16.

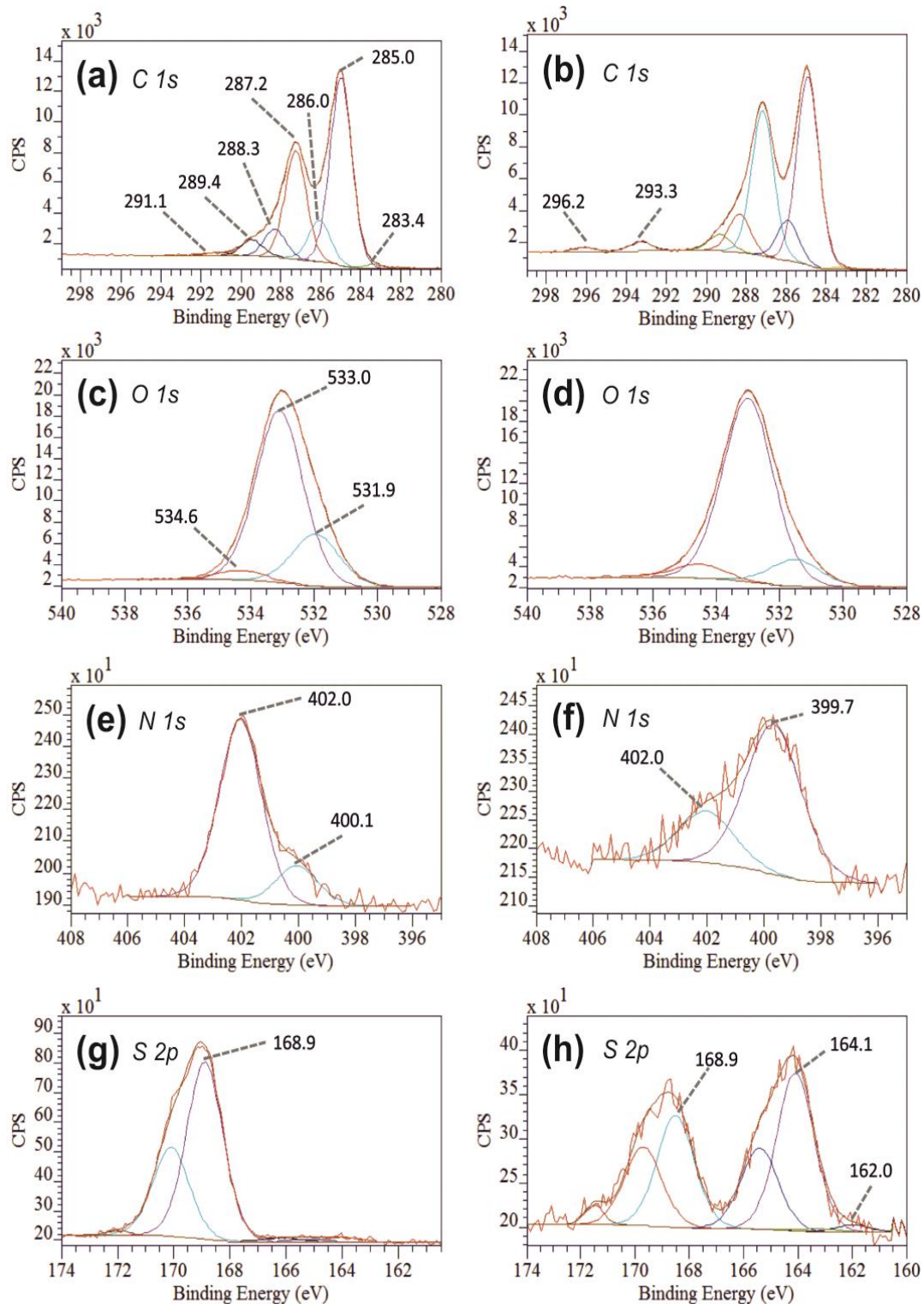


Fig. 31. High resolution XPS spectra of pristine GrO and SS/G-60 nanocomposite material: C1s region of GrO (a); C1s region of SS/G-60 (b); O1s region of GrO (c), O1s region of SS/G-60 (d); N1s region of GrO (e); N1s region of SS/G-60 (f); S2p region of GrO (g); S2p region of SS/G-60 (h).

Table 16. XPS analysis results obtained from high resolution spectra of pristine GrO and SS/G-60 nanocomposite.

Material	BE, ^a eV (Relative area, %) ^b							
	C 1s							K 2p
	C-Si	C=C	C-C	C-O, S-C	C=O, C=N	COO	π - π^*	K ⁺
GrO	283.4 (0.9)	285.0 (48.3)	286.0 (10.7)	287.2 (27.8)	288.3 (7.2)	289.4 (4.2)	291.1 (0.9)	n.d.
SS/G- 60	283.4 (0.5)	285.0 (43.7)	286.0 (9.3)	287.2 (33.8)	288.3 (8.8)	289.4 (3.8)	n.q.	293.3 (100)
	O 1s			N 1s		S 2p		
	O=C	O-C	H ₂ O _{Ads}	N=C	-NO _n	SH	C-S _n ^c	-SO _n
	GrO	531.9 (22.1)	533.1 (73.7)	534.3 (4.1)	400.1 (17.8)	402.0 (82.1)	n.d.	164.1 (2.5)
SS/G- 60	531.9 (11.7)	533.1 (82.1)	534.3 (6.1)	399.7 (74.3)	402.0 (25.7)	162.0 (2.5)	164.1 (60.0)	168.5 (6.1)

^a For 2p orbitals the B.E. of 2p_{3/2} orbital is presented;

^b Area of each component relative to the total core level peak area in percentage;

^c n = 1 or 2; n.d. – not detected; n.q. – not quantified.

Analysis of the C1s spectra of the original GrO material shows a peak at binding energy (B.E.) 285.0 eV ascribed to carbon in the graphitic structure and aromatic rings (sp²); the peak at 286.0 eV is assigned to carbon–carbon single bonds in the carbon structure (sp³). Other three peaks are associated with the presence of the oxygen containing groups: the peak at 287.2 eV ascribed to the hydroxyl and epoxy groups (C–O), the smaller peak at 288.3 eV to the carbonyl groups (C=O) and the peak at 289.4 eV to carboxylic groups (COO). The peak at 291.1 eV is the satellite of sp² aromatic bonds due to π - π^* shake-up [240, 255]. Upon solid-solid reaction, the relative amount of bands at 287.2 and

288.3 eV increase from 27.8% to 33.8% and from 7.2% to 8.8%, respectively, which can be associated to the overlapping of peaks from groups C-S (287.2 eV) and C=N (288.3 eV). These groups confirm the presence of polythiocyanogen in the nanocomposite. For SS/G-60 material the π - π^* bands are overlapped by potassium bands. The potassium signal for K $2p_{3/2}$ at 293.3 eV is typical of K^+ ions [256]. A small peak ascribed to C-Si is also observed, confirmed by the presence of a trace amount of Si in the survey spectra of both GrO and SS/G-60 materials.

In the O1s region spectrum of the original GrO material are present a small peak at 531.9 eV assigned to O=C bonds and a much more intense peak at 533.1 eV due to O-C single bonds. This indicates that hydroxyl or epoxide groups are more abundant than the carbonyl and carboxylic acid groups [240]. An additional peak at higher B.E. is ascribed to water that remained intrinsically adsorbed between the GrO sheets [240, 255]. It can be observed that the nanocomposite material is able to adsorb water in higher extension than the pristine GrO. A reduction of the relative amount of C=O bonds from 22.1% in GrO to 11.7% in SS/G-60 material is observed. Supposedly, carbonyl or carboxylic groups act as oxidative centers initiating the polymerization of SCN^- and anchoring the $(SCN)_n$ chains [202].

In the SS/G-60 nanocomposite material, the band at 402 eV in N1s region, ascribed to the presence $-NO_n$ groups resulting from the GrO preparation process decreases relatively to the one in pristine GrO confirming the leaching during the functionalization procedure. On the other side, a novel band at 399.7 eV is observed after solid-solid reaction and confirms the introduction of $-C=N-$ groups. It is worth to remark that the slightly different B.E. relatively to the original material, indicates that the introduced chemical groups are different from the ones present in the pristine GrO.

The S bands in S2p region appear in the form of doublets, due to the degeneration in the B.E. of $2p_{3/2}$ and $2p_{1/2}$ orbitals. The values of B.E. presented always refer to the $2p_{3/2}$ orbital (Table 16). The S2p signal in the pristine GrO is deconvoluted into a main doublet with S $2p_{3/2}$ at 168.9 eV in accordance with the

presence of sulphate ions in the material's surface. After solid-solid reaction and work-up procedures this peak decreases and two other doublets are introduced with B.E. from $S2p_{3/2}$ orbitals at 164.1 eV (the major band) and 162.0 eV (a minor band). A B.E. of 164.1 eV is typical of sulphur in S-S or C-S- bonds, while a binding energy of 162.0 eV can be ascribed to SH groups [257]. The peak at 172 eV is ascribed to sulphide ions.

The results of XPS analysis fairly match with the results obtained by the other methods. The presence of polyazomethine chains ($-C=N-$) is confirmed. As in the case of DTG analysis, a tendency of SS/G-60 to adsorb water has been reaffirmed. The presence of $-S-S-$ and $-C-S-$ bonds suggest that the polyazomethine chains can be attached to the graphene sheets via the sulphur atoms [258].

Based on the results obtained by the applied methods of analysis, a representative structure of SS/G nanocomposite material was proposed. In summary, characteristic features of the SS/G nanocomposite structure can be defined as follows: (i) small amounts of SCN groups are introduced on the edges of basal graphene planes; (ii) the graphene edges after solid-solid reaction of GrO with KSCN become curled; (iii) the chains of polymer (oligomer) are rather short; (iv) curled edges of graphene facilitate the insertion of H_2O (and supposedly other molecules) between the graphene layers (Fig. 32).

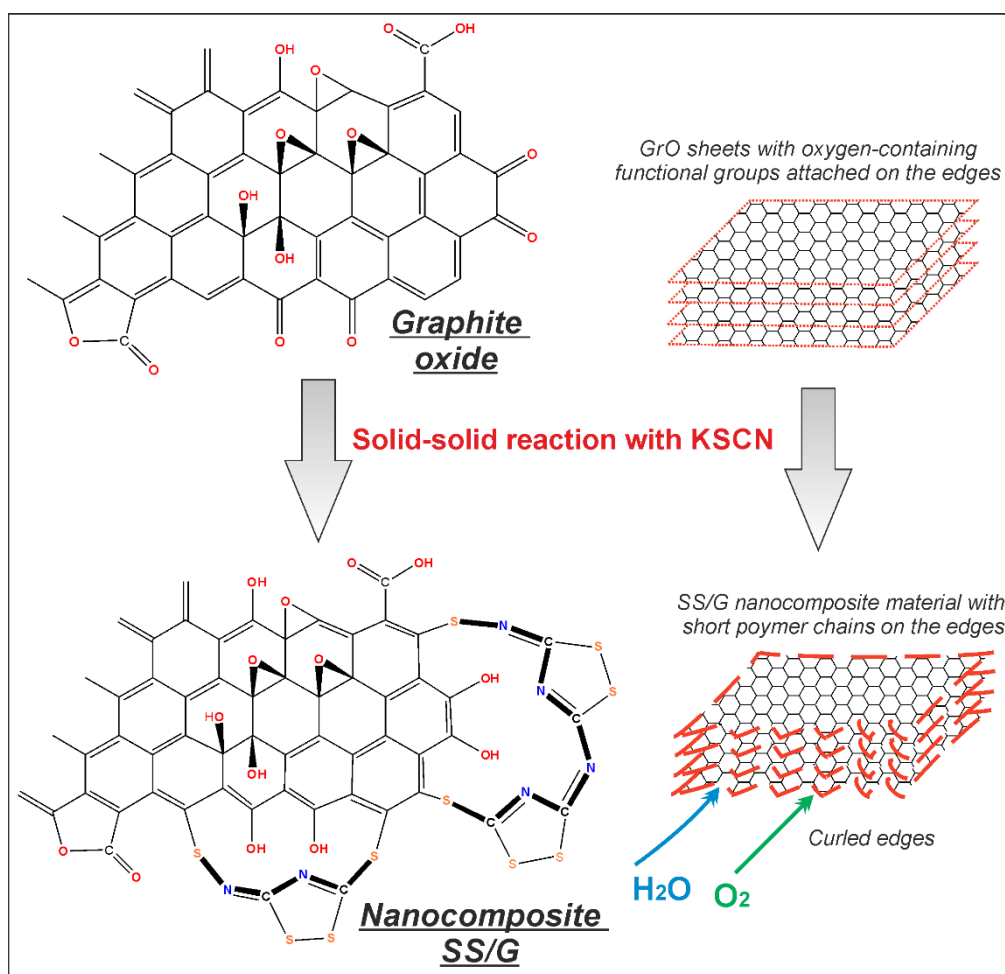


Fig. 32. Representative structure of nanocomposite SS/G material obtained from GrO via solid-solid reaction with KSCN.

3.2.2. Electrochemical study

The electrocatalytic activity of graphene-based materials has lately attracted the attention of researchers. The activity of SCN-doped GrO in ORR, crucial for the efficient operation of cathode in fuel cells, has been reported recently [132]. Among the main advantages of this material stability, high activity and operation in the absence of noble metals are mentioned. In this work the particular attention was paid on studies of the electrocatalytic activity of SS/G products by ORR in acidic media. LSV measurements revealed the highest electrocatalytic activity of product SS/G-60 among other SS/Gs. The electrochemical performance of SS/G-60 nanocomposite modified electrode in 0.5 M H_2SO_4 in Ar and O_2 saturated solutions is presented in Fig. 33 a.

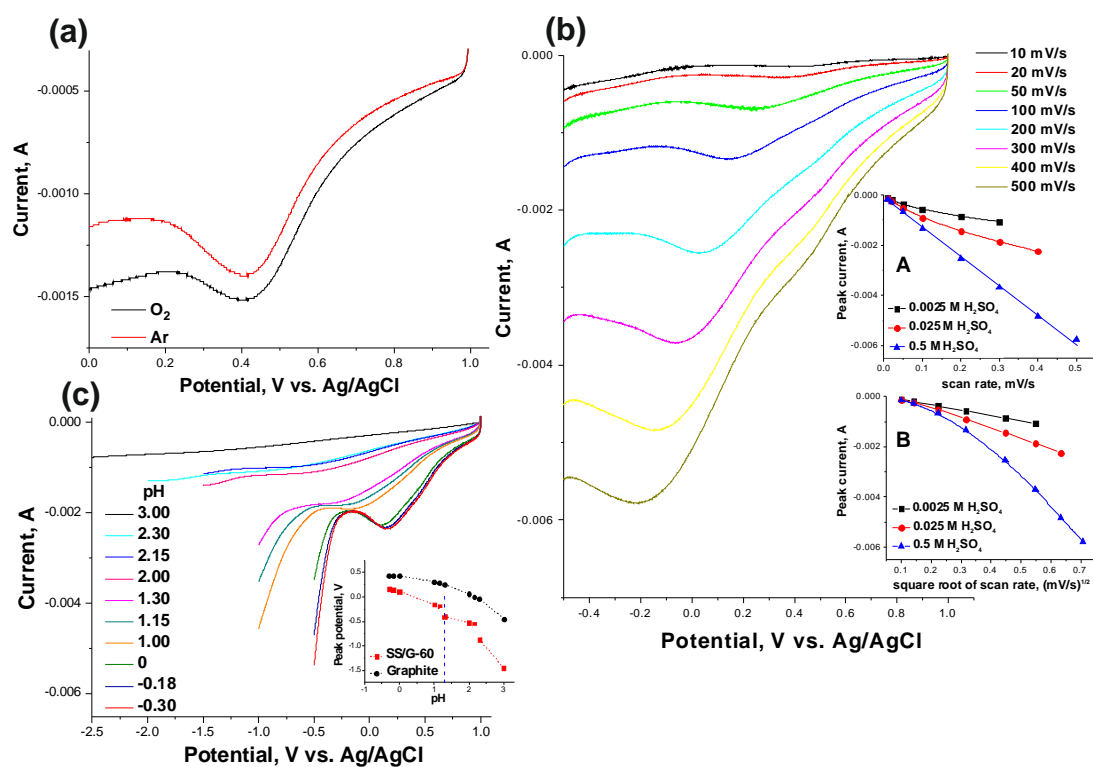


Fig. 33. Linear sweep voltammograms of SS/G-60 nanocomposite material at different potential scan rates and H₂SO₄ concentrations. (a): Linear sweep voltammograms for ORR at SS/G-60 nanocomposite in 0.5 M H₂SO₄ solution saturated with Ar and O₂. Potential scan rate of 50 mV · s⁻¹. (b): Linear sweep voltammograms for ORR at SS/G-60 nanocomposite in 0.5 M H₂SO₄ solution saturated with O₂ recorded using different potential scan rates. Insets show the plots of the peak currents vs. scan rate (A); vs. square root of scan rate coordinate (B). Effect of pH on the potential of peak. Linear sweep voltammograms obtained at different concentrations of H₂SO₄ (c). Inset: dependence of the ORR peak potential on pH of bare graphite electrode (black) and of SS/G-60 nanocomposite material (red).

As shown, the ORR current increased with the potential decrease and the current maximum was attained between 0.34 and 0.55 V. Apparently, ORR current at SS/G-60 nanocomposite modified electrode observed at 0.4 V in O₂ saturated 0.5 M H₂SO₄ solution was much higher as compared to the value of ORR current generated under Ar pretreatment. Moreover, ORR current is doubling if double the amount of SS/G-60 applied onto the bare graphite rod

electrode (data not shown). These facts evidently demonstrated the electrocatalytic activity of SS/G-60 nanocomposite material for ORR in acidic media. It should be noted that the current density of $21.4 \text{ mA} \cdot \text{cm}^{-2}$ obtained for ORR by using the SS/G-60 as electrode material in H_2SO_4 media is ~ 5 times higher as compared to the commercial catalyst ($4.2 \text{ mA} \cdot \text{cm}^{-2}$) [132] and the other recently reviewed catalysts [259], where the latest advances in the field over the past eight years are summarized. The electrocatalytic activity for the ORR in acidic medium was examined, with a particular focus on metal-free, low- and non-platinum electrocatalysts. The specific activity varied from 0.03 to $10.1 \text{ mA} \cdot \text{cm}^{-2}$ for the catalysts presented herein. The above results indicate that SS/G-60 nanocomposite material holds great potential for oxygen reduction in acidic media in practical fuel cells. The stability of catalyst SS/G-60 in H_2SO_4 media was investigated under potential scanning from 1.0 to 0.0 V . Only the insignificant decrease in catalyst's specific activity was noted after 100 min of scanning (Fig. 34).

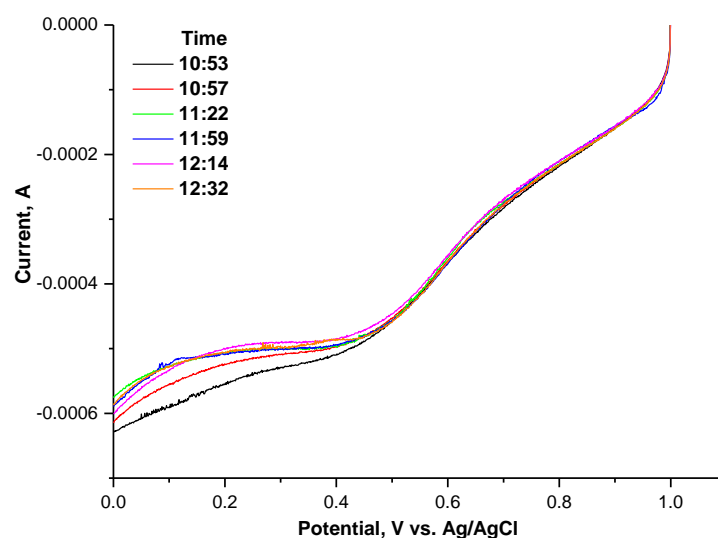
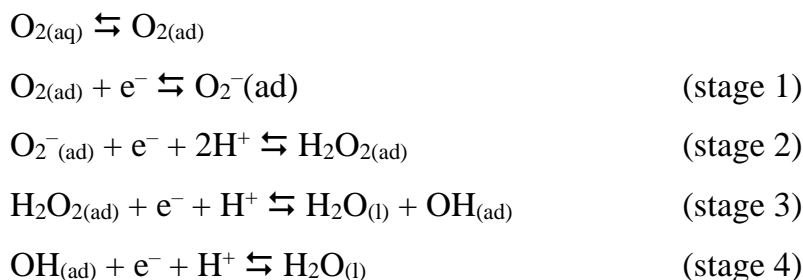


Fig. 34. Stability of SS/G-60 catalyst in $0.5 \text{ M H}_2\text{SO}_4$ obtained by LSV at different time ($0, 5, 30, 70, 85$ and 100 min) under potential scanning from 1 V to 0 V . Scan rate $50 \text{ mV} \cdot \text{s}^{-1}$.

According to the principle of electrochemistry, the process of oxygen reduction occurs via a 4-electron transfer pathway that includes several

subsequent steps [260]. The proton transfer takes place in the electrode reactions in acidic media:



The adsorbed oxygen reduction (stage 1/ stage 2) and hydrogen peroxide reduction (stage 3) stages are reported to be the rate-determining steps of the whole process [260].

The voltammograms obtained by LSV can provide information about the mechanism of electrode reactions in the presence of SS/G-60 nanocomposite material. The experiments were performed in the solutions with three different concentrations of sulphuric acid (0.0025 M; 0.025 M and 0.5 M) at different scan rates. A typical linear sweep voltammograms at different scan rates for the electrode of SS/G-60 nanocomposite in 0.5 M H₂SO₄ solution saturated by oxygen are presented in Fig. 33 b.

Two successive reduction waves can be distinguished in the voltammograms obtained in 0.5 M H₂SO₄ solution. The first wave is present in all voltammograms obtained in 0.0025 M; 0.025 M and 0.5 M H₂SO₄ solutions (Fig. 33 b). Obviously this wave changes its position on the voltage axis in the potential range of 0.4 - -0.2 V dependently on the scan rate. The second wave appears approximately at 0.5 V only in the solution of 0.5 M H₂SO₄ by applying scan rate higher than 100 mV · s⁻¹. The position of this wave on the voltage axis is independent on potential scan rate. The fundamental aspects of electrochemical kinetics state that the peak position is influenced by the scan rate in the cases, when the process is slow and can be defined as a limiting stage [261].

A plot of the peak current vs scan rate gives more detailed information about the mechanism of the process (Fig. 33 b, inset A and B). The theoretical basis of this part is discussed in the textbooks of chemical kinetics and

electrochemistry [262]. In the case when the data give a linear plot using a scan rate coordinate (Fig. 33 b, inset A), an assumption can be made that adsorption is the limiting condition of the process. Meanwhile, when the linear plot is obtained using a coordinate square root of scan rate (Fig. 33 b, inset B), the process is limited by diffusion. These results would seem to suggest that in the case when the concentration of H^+ ions in solution is high, the total process is determined by adsorption. Meanwhile, at higher pH values, the total process is limited by diffusion of H^+ ions (stage 4). In the complex sequence of consecutive reactions, presented above, stage 1 (reduction of the adsorbed O_2 up to O_2^- ion) ought to be ascribed to the limited by adsorption, due to the nature of the previous steps. This stage does not include the transfer of H^+ ions; therefore it should be insensitive to the pH of solution. In the stage 4 the reduction of OH up to H_2O occurs. It includes the transfer of H^+ ions and becomes a limiting stage at higher pH values. These findings suggest that the most effective work of the ORR cathode should be reached in acidic solutions where the H^+ concentration is higher than 1 M.

The effect of pH on the potential of peak is presented in Fig. 33 c. There are also presented the results obtained using a bare graphite electrode (Fig. 33 c, in inset black line). The constant slope obtained in Fig. 33 c, red line, suggests that the electrocatalytic activity using SS/G-60 composite should occur from the Brønsted/Lewis acidic sites on the electrocatalyst surface. The break of a straight line at $pK_a \approx 1.1$ indicate that the electrochemical reduction of oxygen occurs via active functional groups, which according to the pK_a value should be rather strong acidic functional groups. Similar pK_a values are reported for the protonation of secondary aromatic amines and nitrogen in thiazole or polyazomethine [263]. Apparently, electrochemical activity of SS/G-60 nanocomposite is due to the presence of polyazomethine chains and/or dithiazole rings in the structure of $(SCN)_n$ polymer. Meanwhile, the electrochemical reaction that occurs on pure graphite is not associated with acidic or basic functional groups. Continuous change of the slope points to the conclusion that the whole surface of graphite takes place in an electrochemical process. At

higher pH values the electrochemical reaction that occurs on the surface of nanocomposite become of the same nature as that on graphite.

In conclusion, LSV measurements revealed remarkable electrocatalytic activity of product SS/G-60 in acidic media, which current density ($21.4 \text{ mA} \cdot \text{cm}^{-2}$) is 5 times higher compared to that of commercial catalyst. It was found that the mechanism of ORR in acidic media in the presence of SS/G nanocomposite material is dependent on the concentration of H^+ ions. At higher H^+ concentrations the process of electrochemical reduction is limited adsorption of O_2 . Meanwhile, at higher pH values ($\text{pH} > 1.0 \div 1.5$) the process moves to the limited by the diffusion of H^+ ions. Whereas this transition coincides with the step of the protonation of nitrogen in secondary aromatic amines, thiazole, or polyazomethine it is likely that the protonated nitrogen atom sites in SS/G nanocomposite material act as a catalyst in the ORR reaction.

3.3. Thermally reduced graphene oxide as support material for D-fructose biosensor

This part of experimental work was devoted to create reagentless amperometric D-fructose biosensor based on graphene nanomaterials. For this purpose graphene based electrode materials have been synthesized by newly proposed thermal reduction of graphite oxide. The method allowed to separate and collect different fractions of thermally reduced graphene oxide (TRGO) with different physicochemical properties. Aiming to select and apply the fraction of TRGO possessing beneficial properties for D-fructose biosensor operating on effective direct electron transfer (DET), the study and characterization of all TRGO fractions were performed thoroughly.

3.3.1. Examination of TRGO fractions

SEM analysis.

SEM images of graphite, GrO and TRGO fractions are shown in Fig. 35 a – e. The sites with typical morphology features are shown in inserts at higher magnification.

The characteristic change of morphology during the process of thermal reduction of GrO is observed. In the case of graphite, crystalline lamellar structure is clearly visible. Much less crystallinity is observed in GrO, nevertheless, the structure of GrO should be considered to be compact. The SEM results also show the change in morphology of TRGO fractions. Graphene layers in the case of TRGO are stacked in a random fashion, with turbostratic defects. The process of thermal reduction is accompanied by a pronounced decrease in the structure compactness; bulk density data of graphite, GrO and TRGO fractions are presented in Fig. 35 f. Bulk density data are consistent with the SEM results: decrease in the bulk density of TRGO fractions is associated with a random distribution of separate graphene sheets.

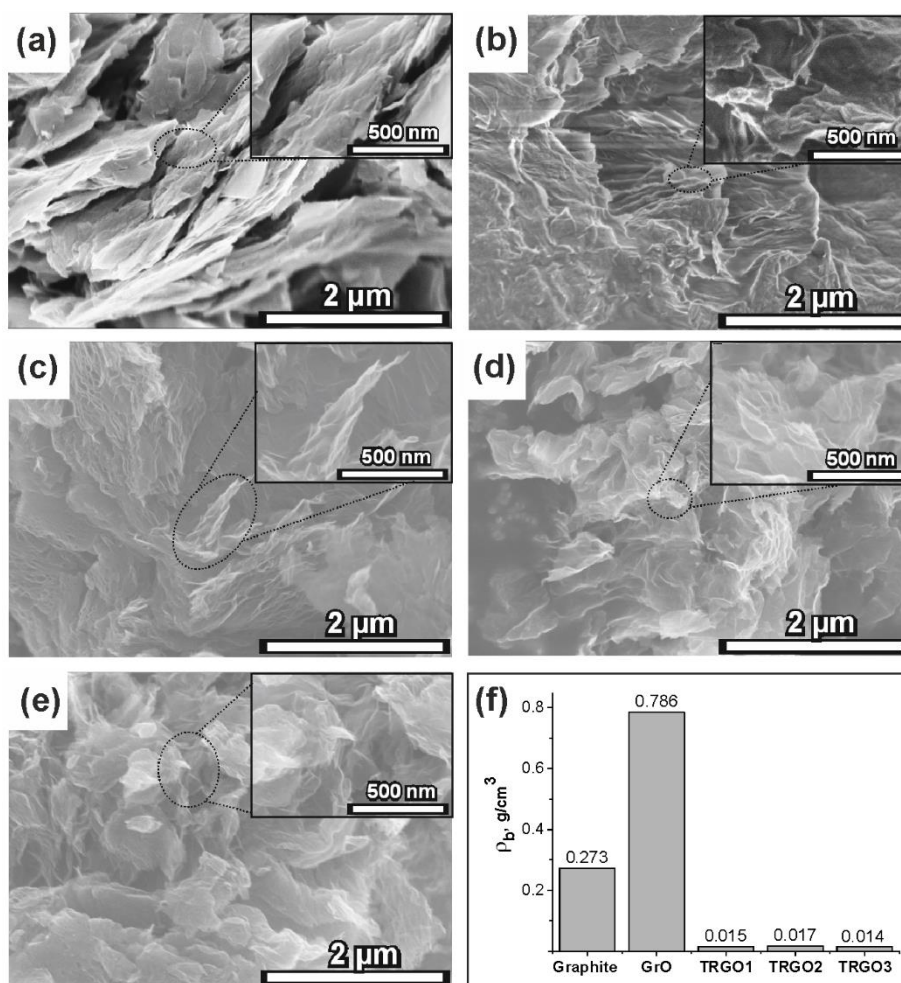


Fig. 35. SEM images of graphite (a), GrO (b) and TRGO (TRGO1 – (c); TRGO2 – (d); TRGO3 – (e)) fractions. Bulk densities of graphite, GrO and TRGO fractions (f).

Powder X-ray diffraction analysis.

The XRD patterns of graphite, GrO and TRGO fractions are presented in Fig. 36.

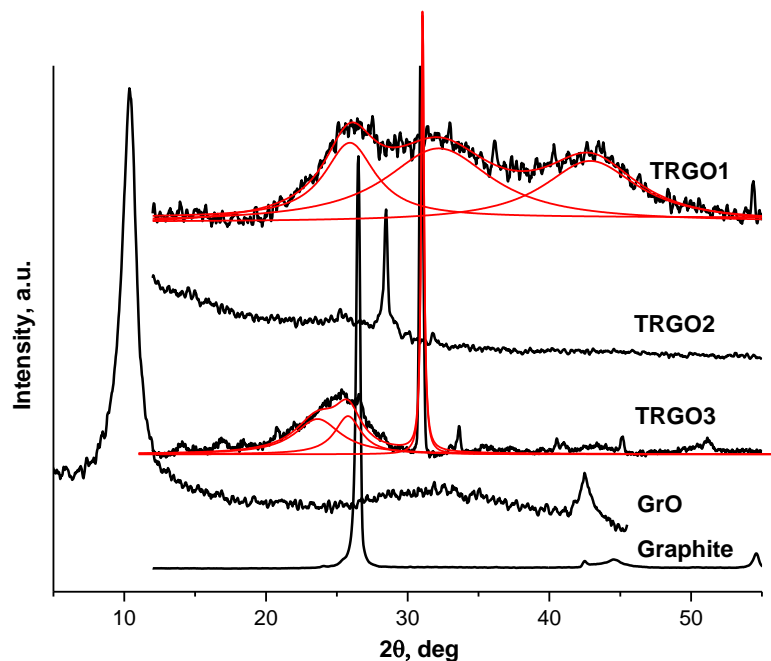


Fig. 36. XRD data of graphite, graphite oxide and TRGO fractions (supplemented with fitting curves).

The XRD pattern of graphite is compared to that in the PDF card 00-056-0159. A sharp peak at $2\theta = 26.54^\circ$ (002) and less intensive peaks at $2\theta = 42.36^\circ$ (100), $2\theta = 44.56^\circ$ (101) and $2\theta = 55.66^\circ$ (004) are present in the diffractogram of graphite. The interlayer distance d_{002} in graphite powder samples determined from the peak at 26.54° equals 0.336 nm; the crystallite size reaches a value of about 31.94 nm. Likewise, the XRD pattern of GrO is consistent with the majority of literature [264]. The peaks in the diffractogram of GrO ($2\theta = 10.35^\circ$ and $2\theta = 42.57^\circ$) correspond to the enlarged interlayer distance of 0.855 nm and the crystallite size of 7.2 nm. The XRD patterns of TRGO fractions indicate that certain ordered structure exists in the case of TRGO2 and TRGO3, while amorphous structure prevails in the case of TRGO1. At this point, we do not have the complete information to explain the origin of pronounced crystalline structures in the TRGO2 and TRGO3 fractions. Taking into account the design of equipment for the thermal reduction of GrO, we can find that the distance, which the particle travels is directly proportional to the electrical charge and inversely proportional to the mass of the particle.

Consequently, the TRGO2 and TRGO3 fractions should consist of small particles with relatively high electrostatic charge. The yield of these fractions is insignificant (TRGO2 - 1.9 %; TRGO3 – 0.4 %). The peaks of crystalline phase in XRD patterns of TRGO2 and TRGO3 ($2\theta = 28.49^\circ$ and $2\theta = 30.95^\circ$ respectively) do not coincide with these of pure graphite and GrO. In both cases the peaks are shifted to higher angles indicating the contraction of the interlayer distance (0.313 nm for TRGO2 and 0.289 nm for TRGO3). Among the reasons that may cause a contraction, defect formation in graphene layer and graphite structure should be mentioned [265]. The defects are formed via the loss of the oxygen-containing functional groups at higher temperatures accompanied by the formation of the vacancies and pentagonal/heptagonal/octagonal ring systems in a graphene layer. In the final stage, the graphene layers are interconnected via covalent bonds. Such changes in the structure lead to the local destruction of sp^2 conjugated system. Presumably, the TRGO particles with higher concentration of defects can act as capacitors having the ability to store an electrical charge. For that reason they can be moved further from the reaction zone in comparison to the particles without defects. A broad peak in the XRD pattern of TRGO3 fraction ($2\theta = 26.07^\circ$) should indicate the increase in size of the π -conjugated system in comparison with the TRGO2. Supposedly, the particles in this fraction are composed of sequential conducting and insulating domains, similar to the structure of an electric capacitor able to accumulate a large amount of electrostatic charges. Fitting curves in this part of the XRD pattern we can assume that the particles in TRGO3 consist of ~10 graphene layers.

The broad peaks in the XRD pattern of TRGO1 fraction indicate that the particles are amorphous and small. The fitting curves of broad peaks are also shown in Fig. 36; they coincide with the peaks of graphite (002), (100) and (101) as well as with the broad peak of pure GrO at $2\theta = 32.23^\circ$. Assuming that the interlayer distance in TRGO1 fraction is the same as in pristine graphite, we can speculate that the particles in this fraction consist of ~5 graphene layers.

Thermal analysis.

TG analysis curves of graphite, GrO and TRGO fractions (Fig. 37 a) show a weight loss between 35 °C and 500 °C.

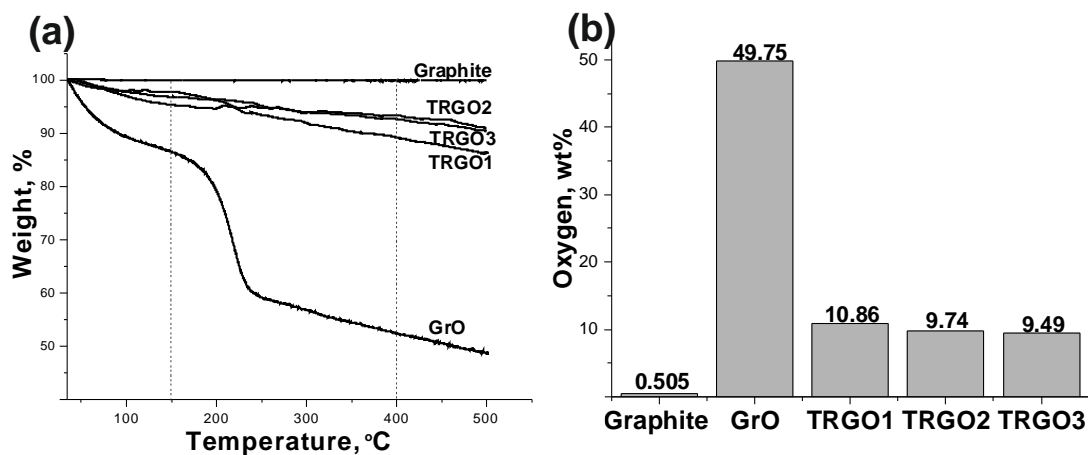


Fig. 37. Data of TG (a) and elemental analysis (b) of graphite, GrO and TRGO fractions.

Up to 150 °C the weight loss occurs due to the removal of water (in the form of adsorbed moisture and intercalated H₂O) [266]. Maximal values in this interval are reached for GrO (13 %); for TRGO fractions this parameter is significantly less (up to 5 %), and no weight loss for graphite is observed. In the temperature interval 150 – 400 °C weight loss of carbonaceous materials occurs due to the changes in their chemical structure: elimination of labile functional groups (carboxy, lactone, epoxy, phenolic) in the form of CO₂ or CO [267]. The most pronounced weight loss is for the GrO (34 %) and TRGO1 (8 %) samples. The maximum rate this process reaches at c.a. 275 °C for both types of carbonaceous materials; the circumstance which proves the similarity of the processes that occur in both materials. Supposedly, remains of GrO structure in the TRGO1 fraction are responsible for the similarities of both processes. The mass change for TRGO2 and TRGO3 occurs evenly in the temperature interval 150 – 500 °C; so, we can conclude that these fractions include less oxygen-containing functional groups in comparison with these in TRGO1. This conclusion is consistent with the data obtained from elemental analysis (see Fig. 37 b).

Raman spectroscopy.

Raman spectra of graphite, GrO and TRGO fractions are shown in Fig. 38 a. Two peaks (D and G) are dominant in the spectra of all samples. The G band has E_{2g} symmetry. Its eigenvector involves the in-plane bond-stretching motion of pairs of sp^2 carbon atoms. This mode occurs at all sp^2 sites and always lies in the range $1500\text{--}1630\text{ cm}^{-1}$. This mode does not require the presence of sixfold ring. The disorder induced bands (D and D') are observed in defective structures. The D band is a breathing mode of A_{1g} symmetry involving phonons near the K zone boundary. This mode is forbidden in perfect graphene and only becomes active in the presence of disorder. The intensity of D mode is specific to the presence of sixfold aromatic rings. The D' band is related to the double resonance Raman process and presents the graphite edge imperfection [268, 269].

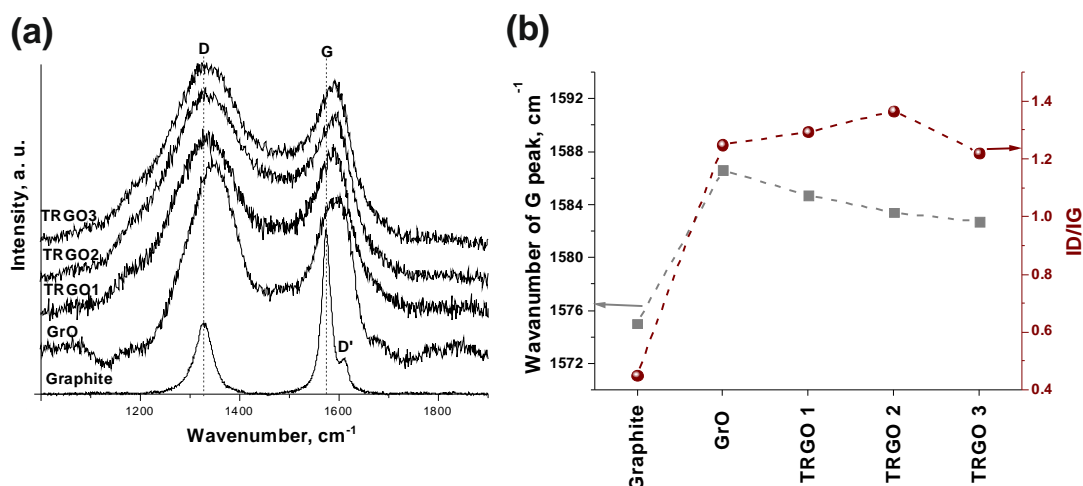


Fig. 38. Raman spectra (excitation wavelength 633 nm) of graphite, GrO and TRGO fractions (a), (b) – shows the G peak position and intensity ratio ID/IG.

In Fig. 38 a, the Raman spectrum of the pristine graphite shows a G peak of high intensity at 1575 cm^{-1} , a D peak at 1328 cm^{-1} , and a weak D' peak at 1612 cm^{-1} . The G band in GrO is shifted to higher frequencies (1587 cm^{-1}) compared to the pristine graphite (Fig. 38 a and Fig. 38 b). We suggest that this shift is mostly affected by the isolated double bonds in the structure of GrO, which resonate at higher frequencies[270]. In TRGO fractions the positions of

G band are shifted slightly to the values more close to that of pristine graphite (Fig. 38 b) indicating that in-plane sp^2 bonding network was restored during the thermal reduction process. However, thermal reduction of GrO involve the removal of oxygen-containing functional groups, thus, creating defects within the graphene basal plane. Additionally, it has been suggested that TRGO exhibits a mixture of sp^2 and sp^3 bonds that depends on the degree of reduction. Furthermore, the electrical transport behavior changes from insulator-hopping-like to semimetal-band-like as the number of localized π states increases [271]. D and G band intensity (I_D/I_G) ratio (Fig. 38 b) shows the level of disorder in graphene [55]. According to this parameter, all TRGO fractions contain approximately the same amount of defects, while the highest concentration is present in TRGO2.

BET analysis.

Specific surface area is one of the most important characteristics for graphene based materials. These materials with high surface area are promising candidates for biosensors [157, 272]. The specific surface area and average pore width of all samples was evaluated using the BET method. The data are shown in Table 17.

Table 17. BET data of graphite, GrO and TGRO fractions.

Materials	BET Surface Area, $m^2 \cdot g^{-1}$	Average pore width, \AA
Graphite	13	107.9
GrO	11	42.3
TRGO1	317	142.3
TRGO2	690	148.8
TRGO3	503	146.3

The BET surface area data of graphite, GrO and TRGO were obtained from the N_2 adsorption–desorption isotherms. It was found that all isotherms of

samples are characterized by an H3 hysteresis loop, which is typical for plate-like particles [273, 274].

Going from graphite to the thermally reduced fractions of GrO, up to TRGO2, the BET surface area and average pore width was increasing. The TRGO2 powder is characterized by the highest surface area ($690 \text{ m}^2 \cdot \text{g}^{-1}$), however it is significantly lower than the theoretical surface area ($2630 \text{ m}^2 \cdot \text{g}^{-1}$) reported for an individual graphene sheet [275]. BET surface area of TRGO2 was increased almost sixty times compared to that of GrO and more than two times compared to that of TRGO1. The surface area and average pore width of TRGO3 were slightly smaller than that of TRGO2. As can be seen in Fig. 38 b the concentration of defects of TRGO3 is lower compared to that of TRGO2. This could explain the smaller BET surface area of TRGO3.

It is known that during the oxidation process the graphite crystallites are reduced in size [55, 276]; simultaneously amount of defects is considerably increased (Fig. 38 b). However, as can be seen in Table 17, BET surface area and average pore width of GrO have the smallest values. This divergence could be explained by the fact that the N_2 molecules are unable to penetrate the interlamellar space of GrO [277]. Also, we can assume that the main reason of the different sedimentation path length between TRGO2 and TRGO3 is the electrostatic charge of the particle, since the surface area data of both fractions is approximately the same.

All three fractions of TRGO were applicable for design of amperometric D-fructose biosensors acting on direct electron transfer principles. More electrochemical measurements are described in [278]. In conclusion, the achieved high values of the sensitivity are the same order as for other D-fructose sensors based on synergistic mediated processes. The electrode based on TRGO1 exhibited the highest sensitivity of $14.5 \mu\text{A} \cdot \text{mM}^{-1} \cdot \text{cm}^{-2}$. After a period of 5 days the sensitivity biosensor was decreased less by than 20%, therefore, it displays a good stability for D-fructose determination. The biosensor can be used for D-fructose measurements in fresh and heat treated apple and orange juices.

3.4. Optimization of the transfer process of graphene oxide coatings

One of the most promising applications of graphene-based materials is their use as transparent, conductive thin films. For this purpose they must be transferred onto arbitrary insulating substrates. Therefore, the last part of experimental work was devoted to optimize the process of transfer of GO coatings prepared by filtration on the transparent polyethylene terephthalate substrate. The two-stage optimization procedure was chosen for this study.

Plackett-Burman optimization.

Parameter estimates using various testing protocols were determined from a PB design for the linear regression models (Equation 1). Results obtained from the blackness tests (before and after adhesion tests; see Fig. 39 a and b are shown in Fig. 39 c and d. Intercept values are shown next to the relevant parameter on the interlayer coordinates. Certain regularities can be found analysing these models. It is worth noting that according to the blackness test results, the influence of the interlayer is much less significant in comparison with that of the optimization parameters used in a PB design. The slightly more significant effect has a PEI interlayer. The best adhesion is obtained using an AA interlayer. The similar conclusion can be done by comparing the intercept values in both models. Adhesion test reduces the intercept values in all cases, because the blackness of the samples after this procedure is reduced. Meanwhile, slope values after the adhesion test change in a less orderly manner. In general, the amount of significant coefficients increases from 24 to 35, which means that the chosen optimization parameters have a significant impact on the adhesive strength of the GO coatings after the transfer. In some cases (preferably, for slopes corresponding the side of PET substrate (A) and interlayer thickness (C)), the values tend to maintain their positive or negative signs. In other cases, these values turn from insignificant to significant (for the coating thickness (B) and transfer temperature (E)), and vice versa (the interlayer preparation (D), and solvent (G)).

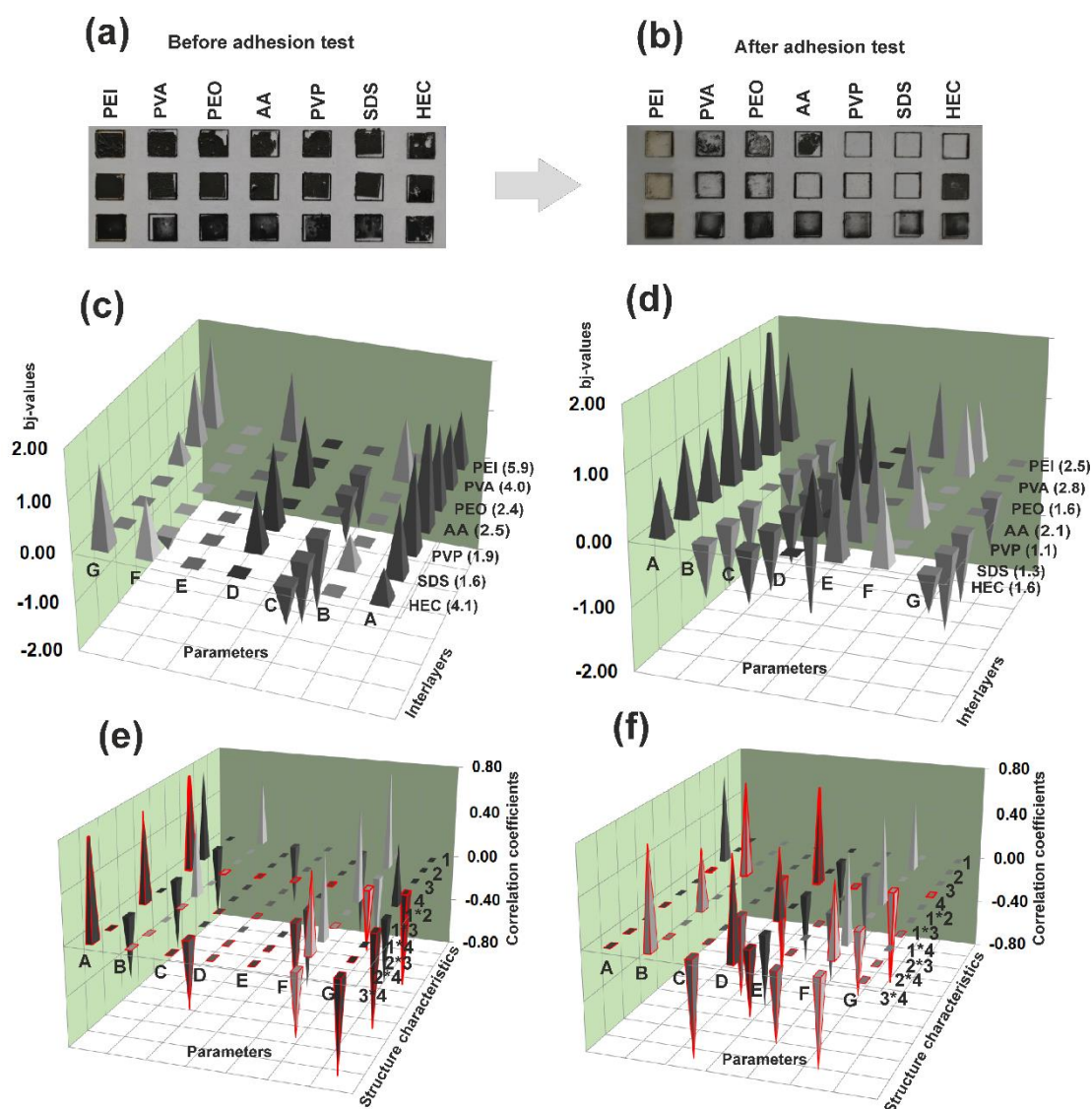


Fig. 39. Quality evaluation of GO coatings after the transfer using PB experimental design and blackness tests. Samples prepared for the analysis before (a) and after (b) adhesion tests. Values of parameter estimates, evaluating blackness before (c) and after (d) adhesion tests. Correlation diagrams representing relations between the optimization parameters and structural characteristics of the interlayer material before (e) and after (f) adhesion tests. For marked correlating values, see Table 6.

To elucidate the relationship between the properties of interlayer materials and their effect on the transfer procedure, a correlation analysis was performed. The correlation was sought between the values of the coefficients in regression models and the parameters related to the structure of organic molecules used in

interlayers (melting point, molar mass, density; Table 6). Additionally, a complex trinomial linear function (Equation 9) was applied in the correlation analysis using a Quantitative Structure Property Relationship (QSPR) strategy [279].

$$F = F_1 - F_2 - F_3 \quad (\text{Equation 9})$$

First term in this function was a parameter inversely proportional to the mass of the molecule:

$$F_1 = 10 + \log_{10}(1/M) \quad (\text{Equation 10})$$

The second term in the F-function was a parameter dependent on the ratio between the number of aliphatic fragments ($-\text{CH}_2-$) and the number of heteroatoms (functional groups) in organic/polymer molecule (F_R):

$$F_2 = F_R/4 \quad (\text{equation 11})$$

Third term F_3 was defined as a deviation not including any a priori information associated with the structure of the molecule and determined using a least square fit. The estimated values of the F-function and its terms are presented in Table 18.

Table 18. Correlation between the quality of GO coatings transfer and the structural parameters of the interlayer.

Interlayer	Terms of structure function F			F
	F_1	F_2	F_3	
PEI	6.92	0.50	4.0	2.4
PVA	5.40	0.50	2.0	2.9
PEO	5.82	0.25	0.0	5.6
AA	7.84	0.50	0.0	7.3
PVP	5.62	0.75	0.0	4.9
SDS	7.54	3.00	0.0	4.5
HEC	5.05	0.45	3.0	1.6

The results of the correlation analysis are given in the diagrams (Fig. 39 e and f). Structural characteristics are presented according to their numbers in

Table 6. Correlation with F-function is labeled as the number 4. Correlation assessment was performed both with the individual structural characteristics and with their products. In the cases of using F-function and its products, bars of the correlation coefficients are marked with red rims.

In Fig. 39 e and f, only those coefficients, whose absolute values are larger than 0.5 are shown. The correlation was conducted with the results from blackness tests performed before and after the adhesion test. There is an apparent difference between these two sets of results. Analyzing the location of significant coefficients in the lines of structure characteristics, the nature of their random distribution can be stated. Meanwhile, the lines of parameters reveal the uneven distribution of these coefficients. Thus, significant values of the correlation coefficients before the adhesion test are observed for the parameters A (side of PET substrate), F (transfer pressure), and G (solvent). After the adhesion test, higher values stand for D (interlayer preparation) and F (transfer pressure).

When using F-function, as well as its products with other parameters, a strong correlation is observed. This implies that if one can find the relationship between the term F_3 in F-function and the structure of organic/polymer molecules used in the interlayer formation, it will be possible to find a closer connection between the structure of interlayer molecules and the quality of GO transfer. It can be seen (Table 18) that the more significant F_3 -values are obtained in the case of three polymers: $F_3(\text{PEI}) > F_3(2\text{HEC}) > F_3(\text{PVA})$, while for the other group of polymers, $F_3(\text{PEO}) = F_3(\text{PVP}) = 0$. As mentioned above, a set of transfer operations is carried out at higher temperatures (above 155 °C). Under these conditions, it is likely that the interaction between functional groups (PET, interlayer material and GO) takes place [280]. The critical role of hydrogen bonds in this type of interactions is reported [281]. The ability of hydrogen-bond formation is a key difference between these two polymer groups with different F_3 -values. Molecules of PEI, HEC, and PVA can readily form hydrogen bonds with PET molecules and GO fragments [282-285]. Similar kind of interactions in the PEO and PVP molecules occurs much more reluctantly in comparison

with the former group [286]. In the case of PVP, the main obstacle to form a hydrogen bond there should be a steric hindrance due to the triple $-\text{CH}_2-$ fragment in the pyrrolidone ring [287]. Thus, one can conclude that the term F_3 can be attributed to the ability of polymer chain to form the hydrogen bonds. F_3 refers the strength of interaction between the molecules of interlayer and GO nanosheets. This term is more significant only in the case of long-chain molecules. For $F_3(\text{AA}) = F_3(\text{SDS}) = 0$; this means that even in the case of strong interaction between small molecules and GO nanosheets (this is essential considering the structure of both molecules, see Table 6), it has no significant effect on the term F_3 . The effect of small molecules used in the interlayer is expressed via terms F_1 and F_2 in F-function; it is not so closely connected with the formation of hydrogen bonds. To summarize, if a molecule is sufficiently big and is able to form strong hydrogen bonds, a significant part of its effect on the quality of GO transfer is expressed via the term F_3 in the structure correlation function F . It is worth noting that a significant correlation between F-function and technological parameters is observed in the cases where these parameters indicate the technological operations related to the hydrophilic/hydrophobic properties of materials: hydrophilic/ hydrophobic side of the PET substrate (A), interlayer preparation temperature (D), and solvent used to remove a PC substrate (G). This evidence strengthens the hypothesis about the crucial role of hydrogen bonds in the quality of GO transfer. The impact of hydrogen bond on the properties of GO paper reinforced with polymers is discussed by other authors as well [281].

Parameter estimates determined for the linear regression models in CAM and ER tests are presented in Fig. 40. Intercept values are shown next to the relevant parameter on the interlayer coordinates. The results of CAM test (Fig. 40 a) reflect the state of the GO layer after the transfer. They are consistent with the results of correlation analysis for the blackness test reported previously (Fig. 39).

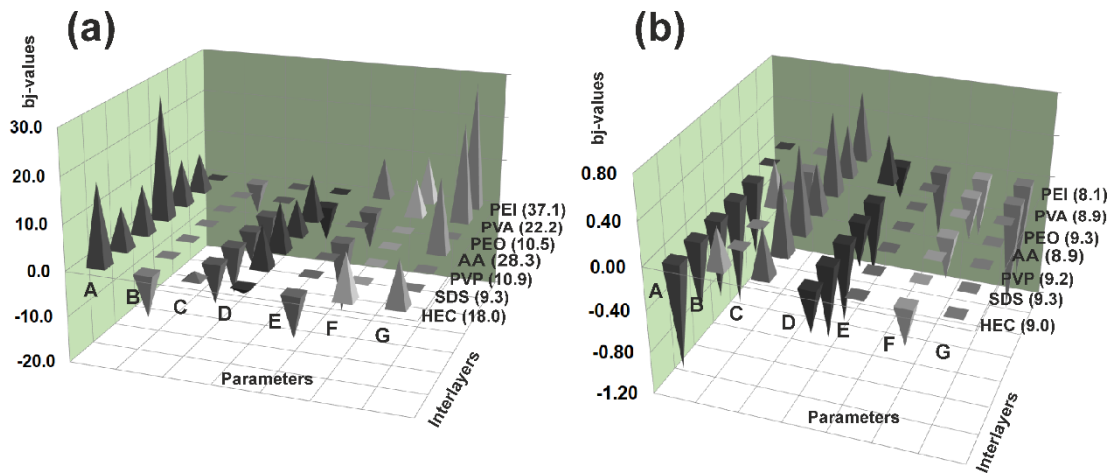


Fig. 40. Values of parameter estimates obtained in linear regression models from: (a) CAM test and (b) ER test.

The most significant parameters in CAM test (A, C, D, and G) generally coincide with these in correlation analysis (A, B, C, D, and G). Physical sense of this coincidence can be found analysing the role of hydrogen bond in the transfer procedure of GO layer on the PET substrate. CAM results are sensitive to the hydrophobic/hydrophilic properties of the surface. Thus, one can conclude that results of CAM test confirm the hypothesis about the crucial role of hydrogen-bond formation on the quality of GO coatings after the transfer.

The results of the ER test (Fig. 40 b) show the most significant parameters as follows: side of the PET substrate (A), interlayer thickness (C), and interlayer preparation (D), and do not match with the results of blackness tests. The reason behind this might be explained as follows: GO layer is characterized by high resistivity. Additionally, the resistivity of GO significantly decreases at higher temperatures in the process of converting it to graphene [188]. So, even though the resistivity of GO layer can be regarded as a quality measure, it has a pronounced non-linear character. Therefore, ER test results were used as a supplementary tool to assess the quality of GO coatings.

Several SEM images are presented in Fig. 41. Micrographs at lower magnification (Fig. 41 a – c) demonstrate the coating quality and morphology changes after the adhesion test. Coatings that show good, poor, and medium adhesion properties are taken for comparison. Before the adhesion test, almost

all GO coatings that met sufficient blackness intensity maintained a smooth morphology. This morphology did not change after the adhesion test for the samples with high adhesion strength. Adhesion test in the cases shown in Fig. 41 b and c reveals a typical morphology showing the profile of layered paper-like structure. In most cases, changes in the coating morphology coincide with the results obtained in adhesion tests.

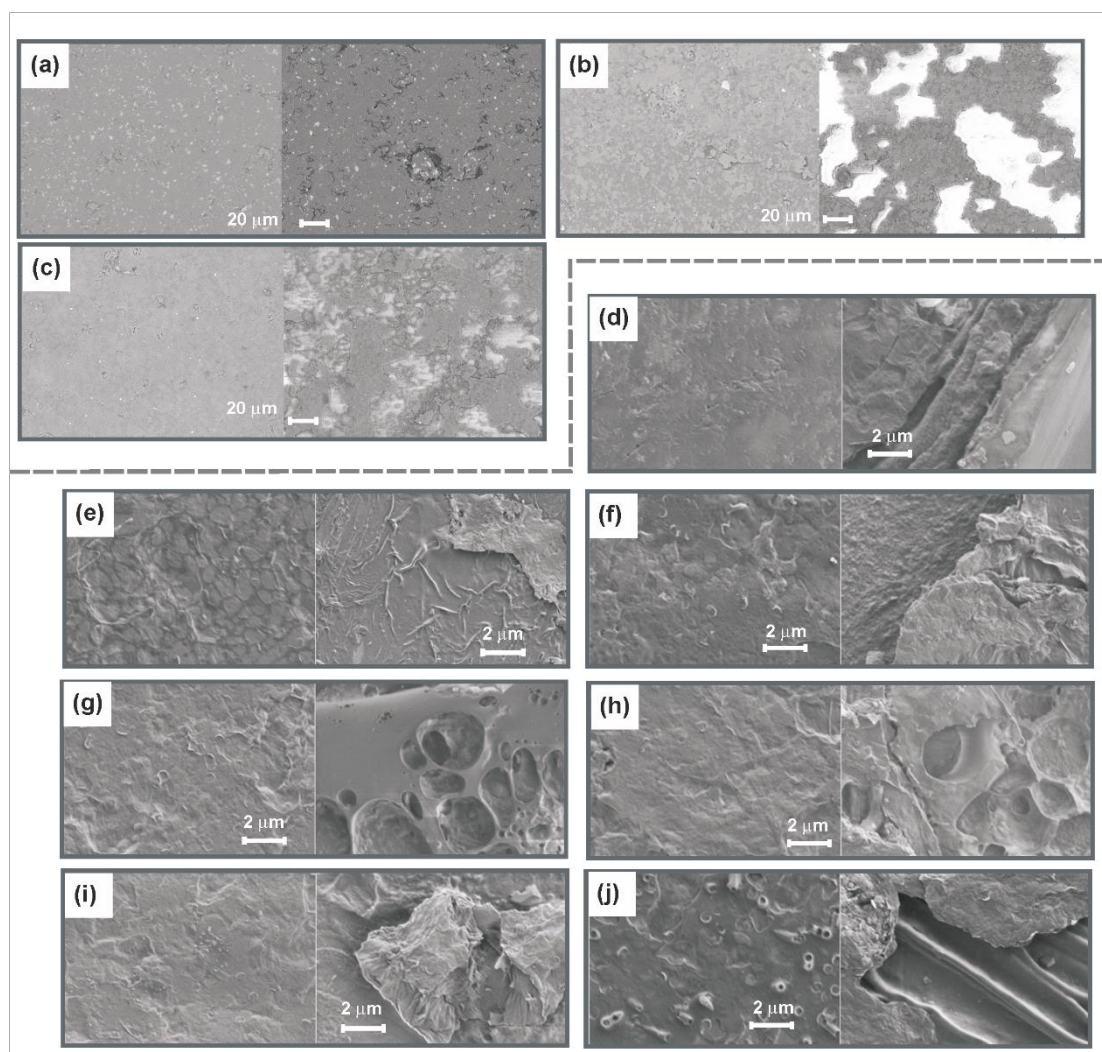


Fig. 41. SEM images of GO-transferred coatings. Micrographs taken at a lower (a, b, and c) and higher (d–j) magnification. Left side of each micrograph – GO coating before adhesion test; right side – after adhesion test. Preparation conditions (number of PB run (Table 4), interlayer (Table 6)): 7, AA (a); 4, PVP (b); 6, SDS (c); 3, PEI (d); 3, PVA (e); 3, PEO (f); 3, AA (g); 3, PVP (h); 3, SDS (i); 3, HEC (j).

Close-up view of the GO coating structure at higher magnification is given in Fig. 41 d – j. Characteristic coating morphology is observed in each case of different interlayers. Characteristic features become more apparent after the adhesion test. Several morphological features can be distinguished in this set of images: paper-like fracture (observed in most cases after the adhesion test), pleat-like structure (Fig. 41 e and j after adhesion test), and fragments of spongy structure (Fig. 41 g, h and j)). The emergence of paper-like fracture is essential taking into account the layered structure of GO. The pleats should occur through the interaction of GO sheets and interlayer polymer molecules penetrating the interlayer space of GO [288]. Voids in the structure can appear by the same mechanism as in the case of GO foam formation [289]. Pleats and voids in the structure, usually appear after the adhesion test, when the outer layers are removed. Among the many factors having the influence on the morphology of GO layer, swelling during the removal of PC layer should be mentioned [290]. We have done experiments examining the swelling of pristine PET membranes and their melts with interlayer materials by weighing (ASTM D2765), and found that the most significant values of swelling degree reaches 2.23% (with SDS interlayer in DMF). In most cases (including pristine PET membranes), swelling did not occur at any degree. However, being in contact with a GO layer, percentage of PET in the mixture is likely to be significantly lower, and swelling may occur much more intensively. It is evident that the structure of GO layer can be controlled using different interlayer materials and transfer conditions, though this question will be researched in more detail in further studies.

Raman spectroscopy.

Raman spectra of GO coatings on a PET substrate are presented in Fig. 42 for different interlayer materials.

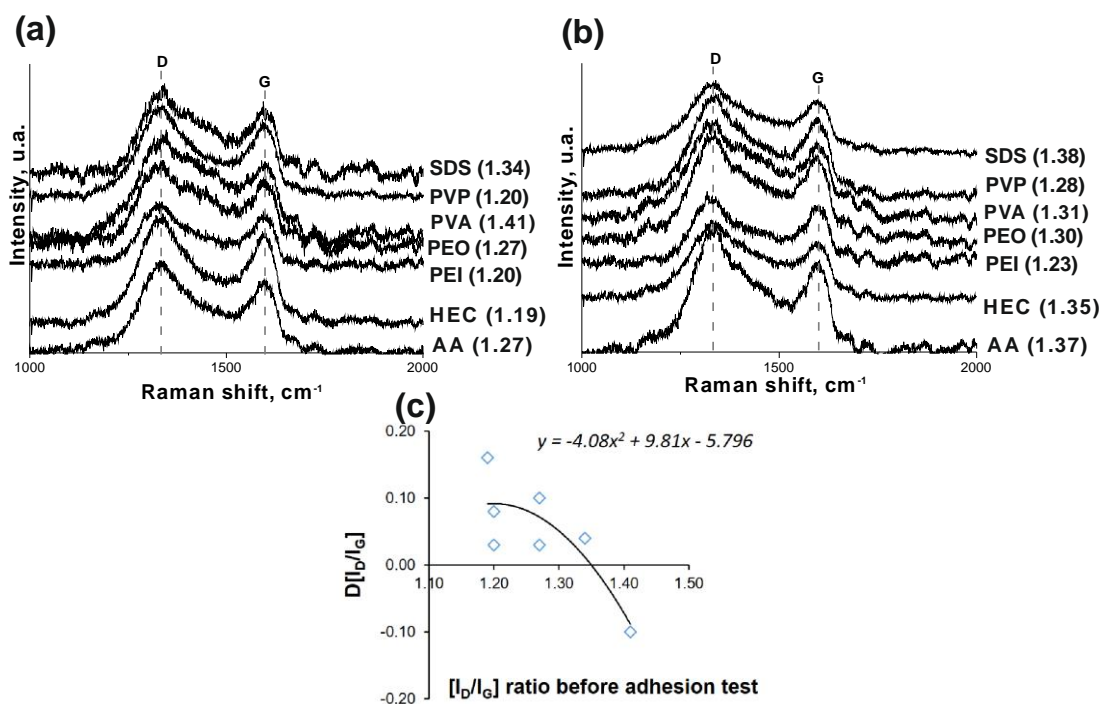


Fig. 42. Raman spectra of GO coatings before (a) and after (b) adhesion test and correlation between the ID/IG ratio before adhesion and the difference between ID/IG ratios before and after adhesion test Δ [ID/IG] (c). Interlayer material is indicated next to the corresponding Raman shift curve. The ID/IG ratio is given in brackets. All coatings are prepared corresponding to PB run 3 (Table 6).

Two main peaks assigned to D ($1310\text{--}1430\text{ cm}^{-1}$) and G (1580 cm^{-1}) bands, which are A_{1g} breathing mode and E_{2g} vibrational mode in-plane, respectively, are prominent in all samples. ID/IG ratio shows disorder of layered GO structure; in Fig. 42, it is given in brackets next to the corresponding curve. According to this parameter, the effect of interlayer material on the fine structure of GO is different. In most cases, before the adhesion test, the ID/IG ratio remains in the range 1.19–1.27. Only in two cases (SDS and PVA), the ID/IG ratio reaches the maximum values of 1.34–1.41. This may be related to the high surface activity of these substances. After the adhesion test, the ID/IG ratio increases in all cases except PVA interlayer. The correlation coefficient between ID/IG ratio before adhesion and the difference between ID/IG ratios before and after adhesion reaches -0.785 (Fig. 42 c). Even a better correlation is obtained to a quadratic equation. It means that the more ordered layered GO structure is obtained before

adhesion, relatively less ordered structure results after the adhesion test and vice versa. Most probably, the upper part of the GO layer after the transfer, which is peeled-up during the adhesion test, has more ordered structure. In the case of PVA, adhesion force leads to the formation of pleat-like structure (see Fig. 41 e). One might conjecture that such a structure is the evidence of weak forces between the GO layers resulting from the PVA adsorption.

Taking everything into account, it can be concluded that the quality of GO coatings mainly is influenced by the optimization parameters as follows: side of the PET substrate (A), interlayer thickness (C), coating thickness (B), and transfer temperature (E). Going into details, only three of these (C, B, and E) are appropriate for further investigation. Parameter A (categorizing hydrophobic/hydrophilic properties of the PET substrate) is inappropriate for further optimization procedures, because this parameter takes on only two possible values without intermediates. Since all the b_A values in Equation 1 are positive, hydrophilic side of the PET substrate was chosen for further optimization using a simplex method.

Simplex optimization.

Based on the results obtained from PB design, initial point in three-parameter simplex optimization was chosen with start coordinates: interlayer a thickness 0.50 μm , coating thickness 400 nm, and transfer temperature 185 $^{\circ}\text{C}$ (Table 19). Coordinates of subsequent simplex points obtained after iterations are presented in the same table. Their arrangement in 3D space of variables is shown in Fig. 43 a.

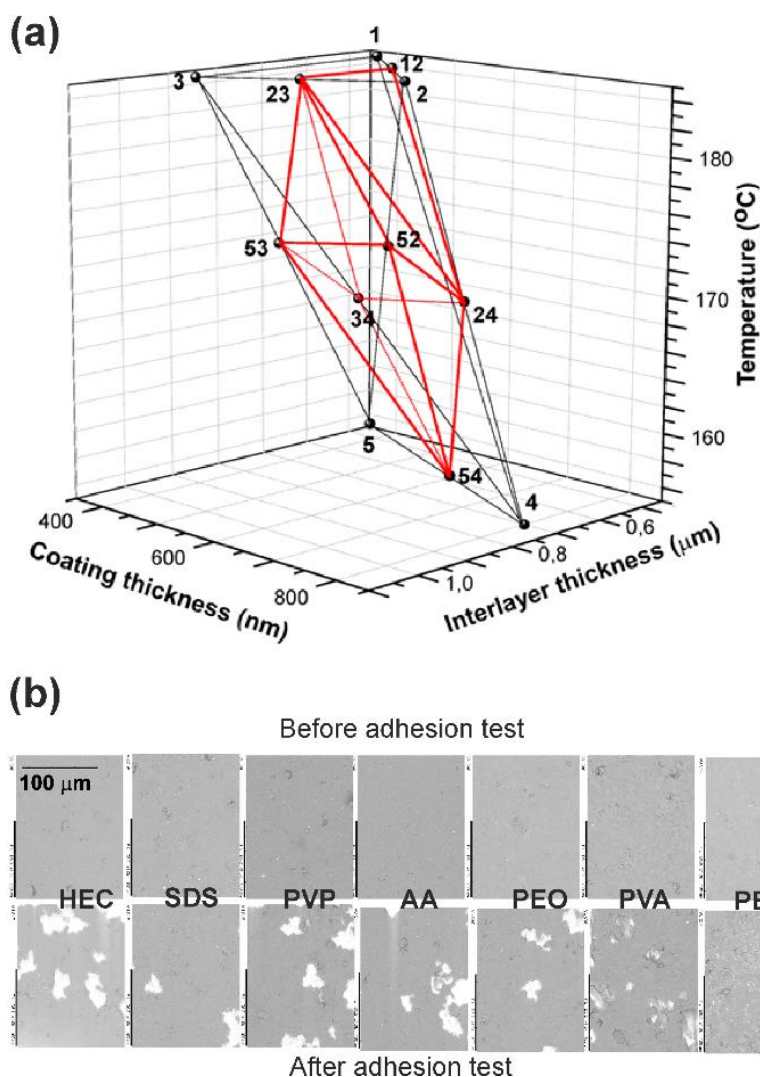


Fig. 43. Simplex optimization of the procedure of the transfer of GO coating. Simplex points in the 3D space of variables (a). SEM images of GO coatings after the transfer at optimal conditions before and after the adhesion test (b).

Blackness values after the adhesion test were used as a parameter for the optimization. When after the iterations, a simplex was transformed into its initial coordinates, new coordinates were generated at the centers of the tetrahedral edges. Additionally, a boundary condition $T < 185\text{ }^{\circ}\text{C}$, was applied in the process of optimization since above $185\text{ }^{\circ}\text{C}$ the PET films begin to develop a yellowish color. After a complete optimization procedure, optimal coordinates for the transfer of GO layer were determined as follows: temperature – $185\text{ }^{\circ}\text{C}$, thickness of GO coating – 500 nm and thickness of the interlayer – $0,80\text{ }\mu\text{m}$. They matched the coordinates of a point 23, obtained in the middle of the

tetrahedral edge between points 2 and 3. There was no need for further subdivision of the tetrahedral edges, since in this case, a length of new edge would be less than the experimental error. SEM images of GO coatings before and after the adhesion test are presented in Fig. 43 b. One can see that under the optimal conditions, the quality and adhesion strength of GO coatings should be considered as good or very good. Although the interlayer material at these conditions has a minimal impact on the quality parameters, the best results are achieved using a PEI interlayer.

Table 19. Simplex coordinates and appropriate blackness values after the adhesion test.

Point No	Coordinates			Interlayer							
	Interlayer thickness (μm)	Coating thickness (nm)	Temperature ($^{\circ}\text{C}$)	PEI	PVA	PEO	AA	PVP	SDS	HEC	Average
1	0.50	400	185	6.41 \pm 0.22	4.37 \pm 0.43	7.35 \pm 0.62	5.92 \pm 0.35	3.87 \pm 0.54	4.09 \pm 0.16	5.12 \pm 0.15	5.30 \pm 0.24
2	0.70	600	185	4.24 \pm 0.98	9.14 \pm 1.49	9.66 \pm 1.40	9.21 \pm 1.24	4.98 \pm 0.27	6.11 \pm 0.26	8.82 \pm 1.49	7.45 \pm 0.56
3	0.90	400	185	5.03 \pm 1.00	5.44 \pm 1.34	8.06 \pm 1.37	6.34 \pm 0.57	4.19 \pm 0.59	5.63 \pm 0.65	6.97 \pm 0.17	5.95 \pm 0.53
4	0.70	800	155	6.80 \pm 0.18	5.78 \pm 0.53	5.74 \pm 0.87	7.61 \pm 1.40	5.31 \pm 0.47	4.97 \pm 0.16	4.71 \pm 0.74	5.84 \pm 0.87
5	0.50	400	155	3.61 \pm 0.88	3.38 \pm 0.78	3.48 \pm 0.27	3.52 \pm 0.24	2.66 \pm 0.09	1.50 \pm 0.08	3.47 \pm 0.36	3.09 \pm 0.83
52	0.87	700	175	2.42 \pm 0.65	3.95 \pm 0.36	4.74 \pm 0.25	8.95 \pm 1.12	5.03 \pm 0.40	5.68 \pm 0.24	3.69 \pm 0.08	4.92 \pm 0.32
53	0.97	600	175	2.78 \pm 0.98	2.14 \pm 0.55	4.55 \pm 0.69	5.77 \pm 0.69	5.79 \pm 0.31	4.27 \pm 0.89	3.51 \pm 0.29	4.12 \pm 0.53
54	0.87	800	160	1.64 \pm 0.73	1.70 \pm 0.33	2.48 \pm 0.50	3.95 \pm 0.58	3.98 \pm 0.69	2.49 \pm 0.09	3.12 \pm 0.30	2.77 \pm 0.02
23	0.80	500	185	9.56 \pm 1.06	8.70 \pm 1.41	9.15 \pm 0.99	8.66 \pm 1.10	8.43 \pm 1.03	9.14 \pm 0.96	8.74 \pm 1.28	8.91 \pm 1.08
24	0.70	700	170	3.48 \pm 1.42	6.52 \pm 0.90	6.55 \pm 1.22	4.47 \pm 0.65	2.92 \pm 0.35	4.27 \pm 0.08	7.57 \pm 1.06	5.11 \pm 0.64
34	0.80	600	170	6.88 \pm 1.15	7.13 \pm 1.21	4.48 \pm 0.87	7.52 \pm 1.38	3.90 \pm 0.73	4.87 \pm 0.21	5.02 \pm 0.41	5.69 \pm 0.88
12	0.80	700	175	6.05 \pm 0.59	4.17 \pm 0.57	4.96 \pm 0.82	2.72 \pm 0.07	5.70 \pm 0.49	5.02 \pm 0.94	7.27 \pm 0.94	5.13 \pm 0.32

CONCLUSIONS

1. The acidic graphene-based catalysts were prepared by functionalization of TRGO with concentrated sulphuric acid, 4-aminobenzenesulphonic acid or phosphoric acid. Characterization performed by FTIR, TGA, XPS and EA methods has confirmed the successful attachment of sulphonic or phosphate groups on TRGO surface. XRD, SEM analyses were used to show the structural evolution of TRGO before and after functionalization. BET analysis proved that all studied samples are predominantly meso- and macroporous materials ($V_{\mu} \approx 0$). The catalytic test in the transesterification of rapeseed oil with methanol showed that all samples exhibited some catalytic activity in above process, however, the best yield of biodiesel was obtained for the sample functionalized with 4-aminobenzenesulphonic acid (the yield of FAME was up to 80%).

2. The basic graphene-based catalysts were prepared by functionalization of TRGO with melamine and gaseous ammonia at different conditions. FTIR, TG, XPS and EA analyses confirmed the successful attachment of nitrogen functional groups on TRGO surface. XPS analysis showed also the occurrence of N-C sp^3 , pyridinic, aminic or pyridone, pyrrolic and graphitic nitrogen in obtained products. From the BET analysis, it was confirmed that all studied samples are meso- and macroporous materials ($V_{\mu} = 0$). SEM and XRD analyses were used to demonstrate the structural changes after functionalization of TRGO surface. The results of catalytic activity test showed that all samples exhibited some catalytic activity in transesterification process, however, the best yield of biodiesel was obtained for the sample functionalized with ammonia at 950 °C for 8 h (the yield of FAME was up to 65%).

3. Graphene-based nanocomposite containing polythiocyanogen (SS/G) was successfully synthesized by solid-solid reaction. SEM analysis revealed the formation of the curled structure on the edges of GrO platelets during the solid-solid reaction between GrO and KSCN. FTIR spectroscopy showed that the structure of inorganic polymer is somewhat dependent on the preparation

protocol, nevertheless, polyazomethine chains are present in all cases. The XRD results evidence the reaction between GrO and KSCN, which leads to the reduction of GrO and formation of polythiocyanogen, are characterized by the unique reflection at about $2\theta = 26.12^\circ$. Results of EA and XPS confirmed the idea that the solid-solid reaction between GrO and KSCN should occur basically on the edges of GrO nanoplatelets. XPS analysis confirmed also the occurrence of potassium ions, S–S and C–S bonds, and polyazomethine chains in SS/G nanocomposite products. TG/DTG curves showed that the products of the solid-solid reaction demonstrate the enhanced ability to adsorb water and, possibly, other small molecules or ions. The set of methods used for the structural characterization revealed that the product of the solid-solid reaction between GrO and KSCN contains polymerized units of SCN^- and polyazomethine chains crosslinked with GrO sheets via S groups.

4. The electrochemical measurements revealed remarkable electrocatalytic activity of product SS/G-60 in acidic media, which current density ($21.4 \text{ mA} \cdot \text{cm}^{-2}$) is 5 times higher compared to that of commercial catalyst. It was found that the mechanism of ORR in acidic media in the presence of SS/G nanocomposite material is dependent on the concentration of H^+ ions. At higher H^+ concentrations the process of electrochemical reduction is limited by adsorption of O_2 . Meanwhile, at higher pH values ($\text{pH} > 1.0 \div 1.5$) the process is likely to be limited by the diffusion of H^+ ions.

5. Using a vertical thermal reduction system, three fractions of TRGO with different physicochemical properties have been prepared from GrO. The process of fractionation was based on the sedimentation rate dependent on the distance from the high-temperature reaction zone. The particles in all three TRGO fractions were different in size and in ability to accumulate an electrostatic charge. Significant decrease in bulk density of all three TRGO fractions ($0.015 \text{ g} \cdot \text{cm}^{-3}$ for TRGO1, $0.017 \text{ g} \cdot \text{cm}^{-3}$ for TRGO2 and $0.014 \text{ g} \cdot \text{cm}^{-3}$ for TRGO3), compared to the pristine graphite and GrO ($0.786 \text{ g} \cdot \text{cm}^{-3}$), was observed. The SEM results also showed the change in morphology of TRGO fractions. Likewise, the XRD analysis revealed the differences in the structure

of three TRGO fractions. The particles in TRGO1 were amorphous and consisted of ca. 5 graphene layers, while certain ordered structure exists in the case of TRGO2 and TRGO3. The particles in TRGO fractions that travel further from the reaction zone contained more defects formed via the loss of the oxygen-containing functional groups at higher temperatures. EA and TG analysis showed that the TRGO2 and TRGO3 fractions include less oxygen-containing functional groups in comparison with the ones in TRGO1. Raman spectra indicated that GrO and all TRGO fractions contain increased amount of defects compared to that of pristine graphite. The particles of TRGO2 fraction possess the highest amount of defects as well as the largest BET surface area ($689.5 \text{ m}^2 \cdot \text{g}^{-1}$) among the other fractions.

6. Optimization, including the transfer of GO layer on the transparent PET substrate, has been performed using a two-stage strategy: a Plackett–Burman experimental design (at the initial stage), and a simplex algorithm (at the final stage). During the initial stage it was determined, that the quality of GO coatings mainly is influenced by the optimization parameters as follows: side of the PET substrate, interlayer thickness, coating thickness, and transfer temperature. The crucial role of hydrogen bond existing in the interlayer polymer material for the transfer procedure was also ascertained. It can be supposed that the hydrogen bonds, formed between GO and polymer molecules in the interlayer, in the case if these molecules are sufficiently large, play a critical role in the quality of process of GO transfer. The morphology of GO layer after the transfer is dependent on the interlayer material. Raman spectra revealed typical changes in the structure of the single GO layer using different interlayer materials. In general, the arrangement of GO sheets in the layer and the structure of the single GO layer can be controlled using appropriate interlayer materials. The final stage was to find the optimal conditions for the GO transfer procedure. Optimal conditions were found as follows: temperature – $185 \text{ }^\circ\text{C}$, thickness of GO coating – 500 nm and thickness of the interlayer – $0,80 \text{ }\mu\text{m}$. GO coatings obtained under optimal conditions can be characterized by good adhesion to the substrate.

LIST OF PUBLICATIONS

Articles in journals

1. **J. Gaidukevič**, J. Razumienė, I. Šakinytė, S. L. H. Rebelo, J. Barkauskas, Study on the structure and electrocatalytic activity of graphene-based nanocomposite materials containing (SCN)_n, Carbon 118 (2017) 156 – 167.
2. I. Šakinytė, J. Barkauskas, **J. Gaidukevič**, J. Razumienė, Thermally reduced graphene oxide: The study and use for reagentless amperometric d-fructose biosensors, Talanta 144 (2015) 1096 – 1103.
3. J. Barkauskas, **J. Dakševič**, S. Budrienė, J. Razumienė, I. Šakinytė, Adhesion of graphene oxide on a transparent PET substrate: a study focused on the optimization process, Journal of Adhesion Science and Technology 28 (2014) 2016 – 2031.

Published contributions to academic conference

1. J. Razumienė, I. Šakinytė, V. Gurevičienė, **J. Gaidukevič**, J. Barkauskas, Thermally reduced graphene oxide fractions for urea biosensor design: implementation and study. 150th ICB Seminar “Micro and Nanosystems in biochemical Analysis”, Warsaw, Poland, 12th – 14th of November, 2016, p. 22.
2. **J. Gaidukevič**, J. Barkauskas, J. Razumienė, I. Šakinytė, R. Baronas, K. Petrauskas, Graphene/(SCN)_n composites as efficient electrocatalysts for the oxygen reduction reaction. 3rd European Conference on Smart Inorganic Polymers, Porto, Portugal, 12th – 14th of September, 2016, p. 61.
3. **J. Gaidukevič**, J. Barkauskas, I. Šakinytė, J. Razumienė, Graphite oxide/(SCN)_x nanocomposite materials: synthesis, characterization and applications for ORR. 18th International Conference-School “Advanced Materials and Technologies 2016”, Palanga, Lithuania, 27th – 31th of August, 2016, p. 116.
4. J. Barkauskas, **J. Gaidukevič**, J. Razumienė, I. Šakinytė, R. Baronas, K. Petrauskas, Electrocatalytic activity of graphene/(SCN)_n composites for

oxygen reduction reaction. World Conference on Carbon “Carbon'16”, Pennsylvania, JAV, 10th – 15th of July, 2016, p. 1 – 6.

5. **J. Gaidukevič**, J. Barkauskas, P. Rechnia, A. Miklaszewska, M. Kozłowski, Functionalized graphene oxide and its application in rapeseed oil transesterification reaction. 59th scientific conference for students of physics and natural sciences “Open readings/Laisvieji skaitymai 2016”, Vilnius, Lithuania, 15th – 18th of March, 2016, p. 173.

6. **J. Gaidukevič**, J. Barkauskas, P. Rechnia, A. Miklaszewska, M. Kozłowski, Nitrogen – Enriched Reduced Graphite Oxide as Solid Basic Catalyst for Transesterification of Rapeseed oil. 2nd International Conference of Chemists “Nanochemistry and Nanomaterials 2015”, Vilnius, Lithuania, 22th – 24th of October, 2015, C5.

7. **J. Gaidukevič**, P. Rechnia, A. Miklaszewska, J. Barkauskas, M. Kozłowski, Functionalized graphene-like materials as efficient solid catalysts for transesterification of rapeseed oil. 6th International Conference on Carbon for Energy Storage/Conversion and Environment Protection (CESEP' 2015), Poznań, Poland, 18th– 22th of October, 2015, p. 111.

8. J. Barkauskas, **J. Gaidukevič**, J. Razumienė, I. Šakinytė, Synthesis and investigation of graphene-based parathiocyanogen nanocomposites. 2nd European Conference on Smart Inorganic Polymers, Uppsala, Sweden, 24th – 26th of September, 2015, p. 43.

9. **J. Gaidukevič**, P. Rechnia, A. Miklaszewska, J. Barkauskas, M. Kozłowski, Modified thermally reduced graphite oxide and its application in transesterification reaction of rapeseed oil. 17th international conference-school “Advanced materials and technologies 2015”, Palanga, Lithuania, 27th – 31th of August, 2015, p. 42.

10. I. Šakinytė, J. Razumienė, J. Barkauskas, **J. Gaidukevič**, Terminiškai redukuoto grafeno oksido frakcijos: savybių studija ir taikymas efektyviai bioelektrokatalizei. Penktoji jaunųjų mokslininkų konferencija “Fizinių ir technologijos mokslų tarpdalykiniai tyrimai”, Vilnius, Lithuania, 10th of February, 2015, p. 31 – 33.

11. **J. Gaidukevič**, J. Barkauskas, K. Petrikaitė, Graphene-based nanocomposite materials containing parathiocyanogen. International conference of Lithuanian Chemical Society, dedicated to Professor Vitas Daušas on his 80th birth anniversary „Chemistry and chemical technology 2015“, Vilnius, Lithuania, 23th of January, 2015, p. 79 – 82.
12. I. Šakinytė, J. Razumienė, J. Barkauskas, **J. Dakševič**, Synthesis and characterization of sp² hybridized carbonaceous materials for D-(-)-tagatose biosensing. 2nd USA International Conference on Surfaces, Coatings and Nanostructured Materials (NANOSMAT USA), Houston, TX, 19th – 22th of May, 2014, p. 118.
13. J. Barkauskas, **J. Dakševič**, E. Štikūnaitė, J. Razumienė, I. Šakinytė, Application of carbon nanomaterials in bioanalysis. The international and interdisciplinary conference “Nanotechnology: Research and Development“, Vilnius, Lithuania, 15th – 16th of May, 2014, p. 37.
14. **J. Dakševič**, J. Barkauskas, Graphene oxide: thermal exfoliation and characterization. International Conference of Lithuanian Chemical Society „Chemistry and chemical technology 2014“, Kaunas, Lithuania, 25th of April, 2014, p. 83 – 86.
15. I. Šakinytė, J. Razumienė, **J. Dakševič**, J. Barkauskas, Graphite oxidation products: characterization and application. 5th international symposium „Advanced micro- and mesoporous materials“, Bulgaria, 6th – 9th of September, 2013, p. 79.
16. **J. Dakševič**, J. Barkauskas, Transfer of graphene oxide coatings onto polyethylene terephthalate: simplex optimization study. Studentų mokslinė konferencija “Chemistry and Chemical Technology of Inorganic Materials”, Kaunas, Lithuania, 24th – 25th of April, 2013, p. 93 – 97.
17. **J. Dakševič**, J. Barkauskas, Transfer of graphene oxide coatings onto polyethylene terephthalate substrate: a simplex optimization study. 56th scientific conference for young students of physics and natural sciences “Open readings/Laisvieji skaitymai 2013”, Vilnius, Lithuania, 20th – 23th of March, 2013, p. 187.

18. **J. Dakševič**, J. Barkauskas, Graphene oxide coatings: parametric study of the transfer onto polyethylene terephthalate substrate. International conference of young chemists “Nanochemistry and Nanomaterials”, Palanga, Lithuania, 7th – 9th of December, 2012, p. 21.
19. J. Barkauskas, **J. Dakševič**, I. Šakinytė, Graphite oxidation products: synthesis and examination. 10-oji Lietuvos chemikų tarptautinė konferencija “Chemija 2011”, Vilnius, Lithuania, 14th – 15th of October, 2011, p. 30.
20. R. Trusovas, G. Račiukaitis, J. Barkauskas, **J. Dakševič**, I. Šakinytė, R. Mažeikienė, Grafito oksido su Kongo raudonojo dažais redukavimas į grafeną lazerio spinduliuote. 39-oji Lietuvos nacionalinė fizikos konferencija, skirta Rutherfordo atomo modelio 100 metų jubiliejui paminėti, Vilnius, Lithuania, 6th – 8th of October, 2011, p. 314.
21. J. Barkauskas, I. Stankevičienė, **J. Dakševič**, R. Trusovas, G. Račiukaitis, R. Mažeikienė, Interaction between graphite oxide nanoparticles and functionalized molecules: a way to produce and/or stabilize graphene coatings. International Conference “Carbon 2011”, Shanghai, China, 24th – 29th of July, 2011, p. 5373 – 5381.
22. R. Trusovas, G. Račiukaitis, R. Mažeikienė, J. Barkauskas, I. Stankevičienė, **J. Dakševič**, Thermal Conductivity of Laser – treated Graphene/Graphite oxide Coatings. International Conference “Carbon 2011”, Shanghai, China, 24th – 29th of July, 2011.

Publications not included in the thesis

1. J. Barkauskas, **J. Dakševič**, R. Juškėnas, R. Mažeikienė, G. Niaura, G. Račiukaitis, A. Selskis, I. Stankevičienė, R. Trusovas, Nanocomposite films and coatings produced by interaction between graphite oxide and Congo red, *Journal of Materials Science* 47 (2012) 5852 – 5860.
2. J. Barkauskas, I. Stankevičienė, **J. Dakševič**, A. Padarauskas, Interaction between graphite oxide and Congo red in aqueous media, *Carbon* 49 (2011) 5373 – 5381.

ACKNOWLEDGEMENTS

Finally, I came to the part where I can say thanks to a number of people who helped me throughout this long scientific journey.

I am sincerely grateful to my supervisor prof. (HP) dr. Jurgis Barkauskas for the knowledge, all given advices and taking care of me during the years of PhD studies. Besides, I'd like to thank my scientific consultant prof. dr. hab. Mieczysław Kozłowski. I feel honoured for working in his scientific group and very thankful for guiding me through the field of catalysis.

Also I'd kindly like to thank dr. Julija Razumienė and dr. Ieva Šakinytė from VU GMC BchI for the help with the electrochemical measurements and practical advices. Special thanks to dr. Susana Luísa Henriques Rebelo from Porto University and dr. Vitalija Jasulaitienė from FTMC for performing XPS measurements and help in interpretation of obtained results.

I'd also like to thank prof. habil. dr. Gediminas Niaura and dr. Ieva Matulaitienė from FTMC for assistance with Raman spectroscopy. I appreciate the patience of prof. dr. Saulutė Budrienė during our discussions and spent time trying to help me finding answer for arising questions.

I am thankful to PhD student Olga Opuchovič for TG/DTG measurements, PhD student Ceslav Višnevskij for performing SEC measurements, dr. Gražina Petraitytė for elemental analysis measurements, PhD student Danas Sakalauskas and dr. Martynas Misevičius for taking SEM pictures for some of my samples.

During my stay in Poland I was always surrounded by a lot of great people, who made me feel like at home. PhD student Aleksandra Miklaszewska, dr. Paulina Rechnia and others, thanks a lot for the great time and help when necessary. I would also like to express my deepest appreciation to all of my colleagues, Ieva Mališauskaitė, Ieva Paklonskaitė, Eglė Gražėnaitė, Lina Pavasarytė and Eva Raudonytė for motivating me and ensuring me to work in a very pleasant and comfortable environment. I also acknowledge financial support from the Lithuanian Science Council across one year of study (2016). Finally, I thank my family members for their love and support.

REFERENCES

- [1] N. Mameda, S. Peraka, S. Kodumuri, D. Chevella, M. R. Marri, H. P. Aytam, N. Nama, *RSC Advances* 6 (2016) 1296-1300.
- [2] O. Deutschmann, H. Knözinger, K. Kochloefl, T. Turek, *Ullmann's Encyclopedia of Industrial Chemistry*, Wiley-VCH Verlag GmbH & Co. KGaA, (2009) 2-94.
- [3] X. Fan, G. Zhang, F. Zhang, *Chemical Society Reviews* 44 (2015) 3023-3035.
- [4] X. K. Kong, Z. Y. Sun, M. Chen, C. L. Chen, Q. W. Chen, *Energy & Environmental Science* 6 (2013) 3260-3266.
- [5] A. Casitas, X. Ribas, *Chemical Science* 4 (2013) 2301-2318.
- [6] J. Wang, H. Gu, *Molecules* 20 (2015) 17070-17092.
- [7] H. Balcar, W. J. Roth, *New and Future Developments in Catalysis*, Elsevier, Amsterdam (2013).
- [8] P. Serp, B. Machado, *Nanostructured Carbon Materials for Catalysis*, Royal Society of Chemistry, RSC Publ., Cambridge (2015).
- [9] Y. Song, K. Qu, C. Zhao, J. Ren, X. Qu, *Advanced Materials* 22 (2010) 2206-2210.
- [10] C. Huang, C. Li, G. Shi, *Energy & Environmental Science* 5 (2012) 8848-8868.
- [11] C. Si, Z. Sun, F. Liu, *Nanoscale* 8 (2016) 3207-3217.
- [12] X. Huang, X. Qi, F. Boey, H. Zhang, *Chemical Society Reviews* 41 (2012) 666-686.
- [13] P. D. Tran, L. H. Wong, J. Barber, J. S. C. Loo, *Energy & Environmental Science* 5 (2012) 5902-5918.
- [14] C. K. Chua, M. Pumera, *Chemical Communications* 52 (2016) 72-75.
- [15] S. Ding, A. A. Cargill, I. L. Medintz, J. C. Claussen, *Current Opinion in Biotechnology* 34 (2015) 24
- [16] J. Liu, Z. Liu, C. J. Barrow, W. Yang, *Analytica Chimica Acta* 859 (2015) 1-19.

- [17] N. J. Coville, S. D. Mhlanga, E. N. Nxumalo, A. Shaikjee, *South African Journal of Science* 107 (2011) 01-15.
- [18] Q. L. Yan, M. Gozin, F. Q. Zhao, A. Cohen, S. P. Pang, *Nanoscale* 8 (2016) 4799-4851.
- [19] H. W. Kroto, J. R. Heath, S. C. O'Brien, R. F. Curl, R. E. Smalley, *Nature* 318 (1985) 162-163.
- [20] S. Iijima, *Nature* 354 (1991) 56-58.
- [21] I. Suarez-Martinez, N. Grobert, C. P. Ewels, *Carbon* 50 (2012) 741-747.
- [22] Y. Wu, *Two-dimensional Carbon: Fundamental Properties, Synthesis, Characterization, and Applications*, Pan Stanford Publ., Singapore (2014).
- [23] V. Georgakilas, J. A. Perman, J. Tucek, R. Zboril, *Chemical Reviews* 115 (2015) 4744-4822.
- [24] D. Xia, M. Otyepka, X. Li, W. Liu, Q. Zheng, *Journal of Nanomaterials* 2015 (2015) 2.
- [25] V. Kalavakunda, S. Hosmane Narayan, *Nanotechnology Reviews* 5 (2016) 369-376.
- [26] L. Dai, *Carbon Nanotechnology Recent Developments in Chemistry, Physics, Materials Science and Device Applications*, Elsevier, Amsterdam; Boston (2006).
- [27] U. K. Sur, *International Journal of Electrochemistry* 2012 (2012) 12.
- [28] D. R. Cooper, B. D'Anjou, N. Ghattamaneni, B. Harack, M. Hilke, A. Horth, N. Majlis, M. Massicotte, L. Vandsburger, E. Whiteway, V. Yu, *ISRN Condensed Matter Physics* 2012 (2012) 56.
- [29] M. J. Allen, V. C. Tung, R. B. Kaner, *Chemical Reviews* 110 (2010) 132-145.
- [30] C. N. R. Rao, A. K. Sood, *Graphene : Synthesis, Properties, and Phenomena*, Wiley-VCH, Weinheim, Germany (2013).
- [31] E. L. Wolf, *Graphene : a New Paradigm in Condensed Matter and Device Physics*, Oxford University Press, Oxford (2016).
- [32] X. Li, J. G. Yu, S. Wageh, A. A. Al-Ghamdi, J. Xie, *Small* 12 (2016) 6640-6696.

- [33] B. M. Blaschke, N. Tort-Colet, A. Guimera-Brunet, J. Weinert, L. Rousseau, A. Heimann, S. Drieschner, O. Kempfski, R. Villa, M. V. Sanchez-Vives, J. A. Garrido, *2D Materials* 4 (2017) 9.
- [34] K. Patel, P. K. Tyagi, *Carbon* 116 (2017) 744-752.
- [35] X. Huang, Z. Yin, S. Wu, X. Qi, Q. He, Q. Zhang, Q. Yan, F. Boey, H. Zhang, *Small* 7 (2011) 1876-1902.
- [36] H. Song, X. Li, P. Cui, S. X. Guo, W. H. Liu, X. L. Wang, *Diamond and Related Materials* 73 (2017) 56-61.
- [37] A. Valipour, S. Ayyaru, Y. Ahn, *Journal of Power Sources* 327 (2016) 548-556.
- [38] A. A. Arbuzov, S. A. Mozhzhukhin, A. A. Volodin, P. V. Fursikov, B. P. Tarasov, *Russian Chemical Bulletin* 65 (2016) 1893-1901.
- [39] Y. Li, J. Yang, J. Song, *Renewable and Sustainable Energy Reviews* 69 (2017) 652-663.
- [40] S. Y. Wu, S. S. A. An, J. Hulme, *International Journal of Nanomedicine* 10 (2015) 9-24.
- [41] A. Akbari, P. Sheath, S. T. Martin, D. B. Shinde, M. Shaibani, P. C. Banerjee, R. Tkacz, D. Bhattacharyya, M. Majumder, *Nature Communications* 7 (2016) 10891.
- [42] Z. J. Wei, Y. X. Hou, Y. Yang, Y.X. Liu, *Current Organic Chemistry* 20 (2016) 2055-2082.
- [43] K. S. Novoselov, A. K. Geim, S. V. Morozov, D. Jiang, Y. Zhang, S. V. Dubonos, I. V. Grigorieva, A. A. Firsov, *Science* 306 (2004) 666-669.
- [44] Y. Hernandez, V. Nicolosi, M. Lotya, F. M. Blighe, Z. Sun, S. De, I. T. McGovern, B. Holland, M. Byrne, Y. K. Gun'Ko, J. J. Boland, P. Niraj, G. Duesberg, S. Krishnamurthy, R. Goodhue, J. Hutchison, V. Scardaci, A. C. Ferrari, J. N. Coleman, *Nature Nanotechnology* 3 (2008) 563-568.
- [45] A. Reina, X. Jia, J. Ho, D. Nezich, H. Son, V. Bulovic, M. S. Dresselhaus, J. Kong, *Nano Letters* 9 (2009) 30-35.
- [46] X. Yang, X. Dou, A. Rouhanipour, L. Zhi, H. J. Räder, K. Müllen, *Journal of the American Chemical Society* 130 (2008) 4216-4217.

- [47] M. Choucair, P. Thordarson, J. A. Stride, *Nature Nanotechnology* 4 (2009) 30-33.
- [48] K. V. Emtsev, A. Bostwick, K. Horn, J. Jobst, G. L. Kellogg, L. Ley, J. L. McChesney, T. Ohta, S. A. Reshanov, J. Rohrl, E. Rotenberg, A. K. Schmid, D. Waldmann, H. B. Weber, T. Seyller, *Nature Materials* 8 (2009) 203-207.
- [49] P. W. Sutter, J. I. Flege, E. A. Sutter, *Nature Materials* 7 (2008) 406-411.
- [50] L. Jiao, X. Wang, G. Diankov, H. Wang, H. Dai, *Nature Nanotechnology* 5 (2010) 321-325.
- [51] M. J. Fernández-Merino, L. Guardia, J. I. Paredes, S. Villar-Rodil, P. Solís-Fernández, A. Martínez-Alonso, J. M. D. Tascón, *The Journal of Physical Chemistry C* 114 (2010) 6426-6432.
- [52] C. K. Chua, M. Pumera, *Journal of Materials Chemistry A* 1 (2013) 1892-1898.
- [53] Y. Su, X. Gao, J. Zhao, *Carbon* 67 (2014) 146-155.
- [54] W. Chen, L. Yan, P. R. Bangal, *The Journal of Physical Chemistry C* 114 (2010) 19885-19890.
- [55] D. R. Dreyer, S. Park, C. W. Bielawski, R. S. Ruoff, *Chemical Society Reviews* 39 (2010) 228-240.
- [56] X. Feng, W. Chen, L. Yan, *RSC Advances* 6 (2016) 80106-80113.
- [57] V. A. Smirnov, N. N. Denisov, M. V. Alifimov, *Nanotechnologies in Russia* 8 (2013) 1-22.
- [58] S. Pei, H. M. Cheng, *Carbon* 50 (2012) 3210-3228.
- [59] Z. Sofer, O. Jankovský, P. Šimek, D. Sedmidubský, J. Šturala, J. Kosina, R. Mikšová, A. Macková, M. Mikulics, M. Pumera, *ACS Nano* 9 (2015) 5478-5485.
- [60] J. I. Paredes, S. Villar-Rodil, A. Martínez-Alonso, J. M. D. Tascón, *Langmuir : the ACS Journal of Surfaces and Colloids* 24 (2008) 10560-10564.
- [61] B. C. Brodie, *Philosophical Transactions of the Royal Society of London* 149 (1859) 249-259.
- [62] L. Staudenmaier, *Berichte der Deutschen Chemischen Gesellschaft* 31 (1898) 1481-1487.

- [63] W. S. Hummers, R. E. Offeman, *Journal of the American Chemical Society* 80 (1958) 1339-1339.
- [64] Z. U. Khan, A. Kausar, H. Ullah, A. Badshah, W. U. Khan, *Journal of Plastic Film & Sheeting* 32 (2016) 336-379.
- [65] M. A. Vieira, G. R. Gonçalves, D. F. Cipriano, M. A. Schettino Jr, E. A. Silva Filho, A. G. Cunha, F. G. Emmerich, J. C. C. Freitas, *Carbon* 98 (2016) 496-503.
- [66] W. Gao, L. B. Alemany, L. Ci, P. M. Ajayan, *Nature Chemistry* 1 (2009) 403-408.
- [67] H. Hu, J. H. Xin, H. Hu, X. Wang, Y. Kong, *Applied Catalysis A: General* 492 (2015) 1-9.
- [68] D. S. Su, S. Perathoner, G. Centi, *Chemical Reviews* 113 (2013) 5782-5816.
- [69] C. Su, K. P. Loh, *Accounts of Chemical Research* 46 (2013) 2275-2285.
- [70] B. Garg, Y. C. Ling, *Green Materials* 1 (2013) 47-61.
- [71] N. Sharma, H. Ojha, A. Bharadwaj, D. P. Pathak, R. K. Sharma, *RSC Advances* 5 (2015) 53381-53403.
- [72] J. Wang, *Chemical Reviews* 108 (2008) 814-825.
- [73] A. Demirbas, *Energy Conversion and Management* 50 (2009) 14-34.
- [74] L. Lin, C. S. Zhou, S. Vittayapadung, X. Q. Shen, M. D. Dong, *Applied Energy* 88 (2011) 1020-1031.
- [75] L. T. Thanh, K. Okitsu, L. V. Boi, Y. Maeda, *Catalysts* 2 (2012) 191-222.
- [76] A. Demirbas, *Energy Conversion and Management* 49 (2008) 2106-2116.
- [77] Y. Zhang, M. A. Dube, D. D. McLean, M. Kates, *Bioresource Technology* 89 (2003) 1-16.
- [78] G. T. Jeong, D. H. Park, C. H. Kang, W. T. Lee, C. S. Sunwoo, C. H. Yoon, B. C. Choi, H. S. Kim, S. W. Kim, U. T. Lee, *Applied Biochemistry and Biotechnology* 113 (2004) 747-758.
- [79] J. M. Encinar, A. Pardal, N. Sanchez, *Fuel* 166 (2016) 51-58.
- [80] F. Ma, M. A. Hanna, *Bioresource Technology* 70 (1999) 1-15.
- [81] T. Nguyen, L. Do, D. A. Sabatini, *Fuel* 89 (2010) 2285-2291.

- [82] T. Ito, Y. Sakurai, Y. Kakuta, M. Sugano, K. Hirano, *Fuel Processing Technology* 94 (2012) 47-52.
- [83] A. Datta, B. K. Mandal, *Renewable & Sustainable Energy Reviews* 57 (2016) 799-821.
- [84] U. Rashid, F. Anwar, B. R. Moser, S. Ashraf, *Biomass & Bioenergy* 32 (2008) 1202-1205.
- [85] A. Sivasamy, K. Y. Cheah, P. Fornasiero, F. Kemausuor, S. Zinoviev, S. Miertus, *Chemosuschem* 2 (2009) 278-300.
- [86] A. Demirbas, A. Bafail, W. Ahmad, M. Sheikh, *Energy Exploration and Exploitation* 34 (2016) 290-318.
- [87] U. Schuchardt, R. Sercheli, R. M. Vargas, *Journal of the Brazilian Chemical Society* 9 (1998) 199-210.
- [88] A. Abdullah, N. Razali, H. Mootabadi, B. Salamatinia, *Environmental Research Letters* 2 (2007) 034001.
- [89] I. B. Bankovic-Ilie, I. J. Stojkovic, O. S. Stamenkovic, V. B. Veljkovic, Y. T. Hung, *Renewable & Sustainable Energy Reviews* 32 (2014) 238-254.
- [90] S. Semwal, A. K. Arora, R. P. Badoni, D. K. Tuli, *Bioresource Technology* 102 (2011) 2151-2161.
- [91] K. G. Georgogianni, A. K. Katsoulidis, P. J. Pomonis, G. Manos, M. G. Kontominas, *Fuel Processing Technology* 90 (2009) 1016-1022.
- [92] A. F. Lee, J. A. Bennett, J. C. Manayil, K. Wilson, *Chemical Society Reviews* 43 (2014) 7887-7916.
- [93] I. M. Atadashi, M. K. Aroua, A. R. A. Aziz, N. M. N. Sulaiman, *Journal of Industrial and Engineering Chemistry* 19 (2013) 14-26.
- [94] M. Zabeti, W. M. A. W. Daud, M. K. Aroua, *Fuel Processing Technology* 90 (2009) 770-777.
- [95] J. Van Gerpen, *Fuel Processing Technology* 86 (2005) 1097-1107.
- [96] H. Fukuda, A. Kondo, H. Noda, *Journal of Bioscience and Bioengineering* 92 (2001) 405-416.
- [97] E. Lotero, Y. J. Liu, D. E. Lopez, K. Suwannakarn, D. A. Bruce, J. G. Goodwin, *Industrial & Engineering Chemistry Research* 44 (2005) 5353-5363.

- [98] N. U. Soriano, R. Venditti, D. S. Argyropoulos, *Fuel* 88 (2009) 560-565.
- [99] M. Balat, *Energy Source Part A* 31 (2009) 1300-1314.
- [100] X. Chen, W. Du, D. H. Liu, F. X. Ding, *Journal of Chemical Technology and Biotechnology* 83 (2008) 71-76.
- [101] S. V. Ranganathan, S. L. Narasimhan, K. Muthukumar, *Bioresource Technology* 99 (2008) 3975-3981.
- [102] Y. M. Sani, W. M. A. W. Daud, A. R. A. Aziz, *Applied Catalysis A: General* 470 (2014) 140-161.
- [103] N. Viriya-empikul, P. Krasae, W. Nualpaeng, B. Yoosuk, K. Faungnawakij, *Fuel* 92 (2012) 239-244.
- [104] F. Chai, F. H. Cao, F. Y. Zhai, Y. Chen, X. H. Wang, Z. M. Su, *Advanced Synthesis & Catalysis* 349 (2007) 1057-1065.
- [105] E. Leclercq, A. Finiels, C. Moreau, *Journal of the American Oil Chemists' Society* 78 (2001) 1161-1165.
- [106] U. Schuchardt, R. Sercheli, R. M. Vargas, *Journal of the Brazilian Chemical Society* 9 (1998) 199-210.
- [107] X. H. Mo, E. Lotero, C. Q. Lu, Y. J. Liu, J. G. Goodwin, *Catalysis Letters* 123 (2008) 1-6.
- [108] J. F. Gomes, J. F. Puna, J. Bordado, M. J. N. Correia, *Reaction Kinetics and Catalysis Letters* 95 (2008) 273-279.
- [109] H. Liu, J. Chen, L. Chen, Y. Xu, X. Guo, D. Fang, *ACS Sustainable Chemistry & Engineering* 4 (2016) 3140-3150.
- [110] S. Suganuma, K. Nakajima, M. Kitano, D. Yamaguchi, H. Kato, S. Hayashi, M. Hara, *Journal of the American Chemical Society* 130 (2008) 12787-12793.
- [111] P. Maneechakr, J. Samerjit, S. Uppakarnrod, S. Karnjanakom, *Journal of Industrial and Engineering Chemistry* 32 (2015) 128-136.
- [112] H. Yuan, B.L. Yang, G. L. Zhu, *Energy & Fuels* 23 (2009) 548-552.
- [113] Q. Q. Guan, Y. Li, Y. Chen, Y. Z. Shi, J. J. Gu, B. Li, R. R. Miao, Q. L. Chen, P. Ning, *RSC Advances* 7 (2017) 7250-7258.

- [114] M. C. Nongbe, T. Ekou, L. Ekou, K. B. Yao, E. Le Grogneq, F. X. Felpin, *Renewable Energy* 106 (2017) 135-141.
- [115] L. J. Konwar, J. Boro, D. Deka, *Renewable and Sustainable Energy Reviews* 29 (2014) 546-564.
- [116] J. Shui, M. Wang, F. Du, L. Dai, *Science Advances* 1 (2015).
- [117] C. R. Raj, A. Samanta, S. H. Noh, S. Mondal, T. Okajima, T. Ohsaka, *Journal of Materials Chemistry A* 4 (2016) 11156-11178.
- [118] J. Zhang, L. Dai, *ACS Catalysis* 5 (2015) 7244-7253.
- [119] J. Zhang, *PEM Fuel Cell Electrocatalysts and Catalyst Layers : Fundamentals and Applications*, Springer, London (2008).
- [120] D. Geng, N. Ding, T. S. Andy Hor, Z. Liu, X. Sun, Y. Zong, *Journal of Materials Chemistry A* 3 (2015) 1795-1810.
- [121] T. Xing, J. Sunarso, W. Yang, Y. Yin, A. M. Glushenkov, L. H. Li, P. C. Howlett, Y. Chen, *Nanoscale* 5 (2013) 7970-7976.
- [122] K. Gong, F. Du, Z. Xia, M. Durstock, L. Dai, *Science* 323 (2009) 760-764.
- [123] H. J. Choi, N. Ashok Kumar, J. B. Baek, *Nanoscale* 7 (2015) 6991-6998.
- [124] P. Hu, K. Liu, C.P. Deming, S. Chen, *Journal of Chemical Technology & Biotechnology* 90 (2015) 2132-2151.
- [125] Z. Yang, H. Nie, X.a. Chen, X. Chen, S. Huang, *Journal of Power Sources* 236 (2013) 238-249.
- [126] L. T. Soo, K. S. Loh, A. B. Mohamad, W. R. W. Daud, W. Y. Wong, *Journal of Alloys and Compounds* 677 (2016) 112-120.
- [127] L. Yang, S. Jiang, Y. Zhao, L. Zhu, S. Chen, X. Wang, Q. Wu, J. Ma, Y. Ma, Z. Hu, *Angewandte Chemie International Edition* 50 (2011) 7132-7135.
- [128] Z. Yang, Z. Yao, G. Li, G. Fang, H. Nie, Z. Liu, X. Zhou, X.a. Chen, S. Huang, *ACS Nano* 6 (2012) 205-211.
- [129] Z. Jin, H. Nie, Z. Yang, J. Zhang, Z. Liu, X. Xu, S. Huang, *Nanoscale* 4 (2012) 6455-6460.
- [130] C. H. Choi, S. H. Park, S. I. Woo, *Green Chemistry* 13 (2011) 406-412.
- [131] S. A. Wohlgemuth, R. J. White, M. G. Willinger, M. M. Titirici, M. Antonietti, *Green Chemistry* 14 (2012) 1515-1523.

- [132] Y. Su, Y. Zhang, X. Zhuang, S. Li, D. Wu, F. Zhang, X. Feng, *Carbon* 62 (2013) 296-301.
- [133] L. F. Mabena, S. Sinha Ray, S. D. Mhlanga, N. J. Coville, *Applied Nanoscience* 1 (2011) 67-77.
- [134] P. Trogadas, T. F. Fuller, P. Strasser, *Carbon* 75 (2014) 5-42.
- [135] C. T. Campbell, *Nature Chemistry* 4 (2012) 597-598.
- [136] N. M. Julkapli, S. Bagheri, *International Journal of Hydrogen Energy* 40 (2015) 948-979.
- [137] Y. Leng, J. Liu, P. Jiang, J. Wang, *Chemical Engineering Journal* 239 (2014) 1-7.
- [138] K. J. Moor, D. C. Valle, C. Li, J. H. Kim, *Environmental Science & Technology* 49 (2015) 6190-6197.
- [139] W. Zhang, P. Sherrell, A. I. Minett, J. M. Razal, J. Chen, *Energy & Environmental Science* 3 (2010) 1286-1293.
- [140] N. M. D. A. Coelho, J. L. B. Furtado, C. Pham-Huu, R. Vieira, *Materials Research* 11 (2008) 353-357.
- [141] N. Gupta, Y. Ding, Z. Feng, D. Su, *ChemCatChem* 8 (2016) 922-928.
- [142] E. Lam, J. H. T. Luong, *ACS Catalysis* 4 (2014) 3393-3410.
- [143] J. L. Figueiredo, M. F. R. Pereira, *Catalysis Today* 150 (2010) 2-7.
- [144] A. E. Aksoylu, J. L. Faria, M. F. R. Pereira, J. L. Figueiredo, P. Serp, J. C. Hierso, R. Feurer, Y. Kihn, P. Kalck, *Applied Catalysis A: General* 243 (2003) 357-365.
- [145] D. J. Guo, Z. H. Jing, *Journal of Power Sources* 195 (2010) 3802-3805.
- [146] T. Harada, S. Ikeda, M. Miyazaki, T. Sakata, H. Mori, M. Matsumura, *Journal of Molecular Catalysis A: Chemical* 268 (2007) 59-64.
- [147] S. Sotiropoulou, V. Gavalas, V. Vamvakaki, N. A. Chaniotakis, *Biosensors and Bioelectronics* 18 (2003) 211-215.
- [148] P. Yáñez-Sedeño, S. Campuzano, J. Pingarrón, *C* 3 (2017) 3.
- [149] S. F. Oliveira, G. Bisker, N. A. Bakh, S. L. Gibbs, M. P. Landry, M. S. Strano, *Carbon* 95 (2015) 767-779.

- [150] L. Su, W. Jia, C. Hou, Y. Lei, *Biosensors and Bioelectronics* 26 (2011) 1788-1799.
- [151] S. Vaddiraju, I. Tomazos, D. J. Burgess, F. C. Jain, F. Papadimitrakopoulos, *Biosensors and Bioelectronics* 25 (2010) 1553-1565.
- [152] Y. Liu, J. Yu, *Microchimica Acta* 183 (2016) 1-19.
- [153] F. R. Baptista, S. A. Belhout, S. Giordani, S. J. Quinn, *Chemical Society Reviews* 44 (2015) 4433-4453.
- [154] J. J. Gooding, *Electrochimica Acta* 50 (2005) 3049-3060.
- [155] Z. Zhu, L. Garcia-Gancedo, A. J. Flewitt, H. Xie, F. Moussy, W. I. Milne, *Sensors* 12 (2012) 5996.
- [156] W. Feng, P. Ji, *Biotechnology Advances* 29 (2011) 889-895.
- [157] Y. Shao, J. Wang, H. Wu, J. Liu, I. A. Aksay, Y. Lin, *Electroanalysis* 22 (2010) 1027-1036.
- [158] S. K. S. Patel, S. H. Choi, Y. C. Kang, J. K. Lee, *ACS Applied Materials & Interfaces* 9 (2017) 2213-2222.
- [159] Y. Gogotsi, in: G. M. Chow, I.A. Ovid'ko, T. Tsakalacos (Eds.), *Nanostructured Films and Coatings*, Springer Netherlands, Dordrecht, (2000) 25-40.
- [160] P. Avouris, C. Dimitrakopoulos, *Materials Today* 15 (2012) 86-97.
- [161] E. P. Randviir, D. A. C. Brownson, C. E. Banks, *Materials Today* 17 (2014) 426-432.
- [162] F. Bonaccorso, Z. Sun, T. Hasan, A. C. Ferrari, *Nature Photonics* 4 (2010) 611-622.
- [163] Y. Yang, A. M. Asiri, Z. Tang, D. Du, Y. Lin, *Materials Today* 16 (2013) 365-373.
- [164] H. Jang, Y. J. Park, X. Chen, T. Das, M. S. Kim, J. H. Ahn, *Advanced Materials* 28 (2016) 4184-4202.
- [165] N. Mishra, J. Boeckl, N. Motta, F. Iacopi, *Physica Status Solidi (a)* 213 (2016) 2277-2289.
- [166] W. Fang, A. L. Hsu, Y. Song, J. Kong, *Nanoscale* 7 (2015) 20335-20351.

- [167] A. Allagui, M. A. Abdelkareem, H. Alawadhi, A. S. Elwakil, *Scientific Reports* 6 (2016) 21282.
- [168] M. Clausi, M. G. Santonicola, S. Laurenzi, *Composites Part A: Applied Science and Manufacturing* 88 (2016) 86-97.
- [169] R. K. Joshi, S. Alwarappan, M. Yoshimura, V. Sahajwalla, Y. Nishina, *Applied Materials Today* 1 (2015) 1-12.
- [170] A. Rani, K. Chung, J. Kwon, S. J. Kim, Y. H. Jang, Y. J. Jang, L. N. Quan, M. Yoon, J. H. Park, D. H. Kim, *ACS Applied Materials & Interfaces* 8 (2016) 11488-11498.
- [171] L. J. Cote, F. Kim, J. Huang, *Journal of the American Chemical Society* 131 (2009) 1043-1049.
- [172] H. Shi, C. Wang, Z. Sun, Y. Zhou, K. Jin, G. Yang, *Science China Physics, Mechanics & Astronomy* 58 (2015) 1-5.
- [173] A. Chavez-Valdez, M. S. P. Shaffer, A. R. Boccaccini, *The Journal of Physical Chemistry B* 117 (2013) 1502-1515.
- [174] J. H. Chen, M. Ishigami, C. Jang, D. R. Hines, M. S. Fuhrer, E. D. Williams, *Advanced Materials* 19 (2007) 3623-3627.
- [175] Y. Chen, X. L. Gong, J. G. Gai, *Advanced Science* 3 (2016) 1500343-n/a.
- [176] T. Yoon, W. C. Shin, T. Y. Kim, J. H. Mun, T. S. Kim, B. J. Cho, *Nano Letters* 12 (2012) 1448-1452.
- [177] W. Gannett, W. Regan, K. Watanabe, T. Taniguchi, M. F. Crommie, A. Zettl, *Applied Physics Letters* 98 (2011) 242105.
- [178] R. Othmen, K. Rezgui, A. Cavanna, H. Arezki, F. Gunes, H. Ajlani, A. Madouri, M. Oueslati, *Journal of Applied Physics* 115 (2014) 214309.
- [179] P. Y. Huang, C. S. Ruiz-Vargas, A. M. van der Zande, W. S. Whitney, M. P. Levendorf, J. W. Kevek, S. Garg, J. S. Alden, C. J. Hustedt, Y. Zhu, J. Park, P. L. McEuen, D. A. Muller, *Nature* 469 (2011) 389-392.
- [180] J. W. Suk, A. Kitt, C. W. Magnuson, Y. Hao, S. Ahmed, J. An, A. K. Swan, B. B. Goldberg, R. S. Ruoff, *ACS Nano* 5 (2011) 6916-6924.

- [181] C. J. An, S. J. Kim, H. O. Choi, D. W. Kim, S. W. Jang, M. L. Jin, J. M. Park, J. K. Choi, H. T. Jung, *Journal of Materials Chemistry A* 2 (2014) 20474-20480.
- [182] J. Leclercq, P. Sveshtarov, *Bulgarian Journal of Physics* 43 (2016) 121-147.
- [183] L. G. P. Martins, Y. Song, T. Zeng, M. S. Dresselhaus, J. Kong, P. T. Araujo, *Proceedings of the National Academy of Sciences of the United States of America* 110 (2013) 17762-17767.
- [184] J. Sun, S. Deng, W. Guo, Z. Zhan, J. Deng, C. Xu, X. Fan, K. Xu, W. Guo, Y. Huang, X. Liu, *Journal of Nanomaterials* 2016 (2016) 7.
- [185] S. Bae, H. Kim, Y. Lee, X. Xu, J. S. Park, Y. Zheng, J. Balakrishnan, T. Lei, H. Ri Kim, Y. I. Song, Y. J. Kim, K. S. Kim, B. Ozyilmaz, J. H. Ahn, B. H. Hong, S. Iijima, *Nature Nanotechnology* 5 (2010) 574-578.
- [186] B. Hu, W. Chen, J. Zhou, *Sensors and Actuators B: Chemical* 176 (2013) 522-533.
- [187] J. C. Meredith, *Journal of Materials Science* 38 (2003) 4427-4437.
- [188] N. Sukumar, M. Krein, Q. Luo, C. Breneman, *Journal of Materials Science* 47 (2012) 7703-7715.
- [189] X. Yan, J. Chen, J. Yang, Q. Xue, P. Miele, *ACS Applied Materials & Interfaces* 2 (2010) 2521-2529.
- [190] H. C. Schniepp, J. L. Li, M. J. McAllister, H. Sai, M. Herrera-Alonso, D. H. Adamson, R. K. Prud'homme, R. Car, D. A. Saville, I. A. Aksay, *The Journal of Physical Chemistry B* 110 (2006) 8535-8539.
- [191] M. J. McAllister, J. L. Li, D. H. Adamson, H. C. Schniepp, A. A. Abdala, J. Liu, M. Herrera-Alonso, D. L. Milius, R. Car, R. K. Prud'homme, I. A. Aksay, *Chemistry of Materials* 19 (2007) 4396-4404.
- [192] P. Rechnia, A. Malaika, M. Kozłowski, *Fuel* 154 (2015) 338-345.
- [193] M. Toupin, D. Bélanger, *Langmuir : the ACS Journal of Surfaces and Colloids* 24 (2008) 1910-1917.
- [194] A. M. Puziy, O. I. Poddubnaya, B. Gawdzik, M. Sobiesiak, M. M. Tsyba, *Adsorption Science & Technology* 25 (2007) 531-542.

- [195] A. Laheäär, S. Delpeux-Ouldriane, E. Lust, F. Béguin, *Journal of The Electrochemical Society* 161 (2014) A568-A575.
- [196] D. Du, P. Li, J. Ouyang, *ACS Applied Materials & Interfaces* 7 (2015) 26952-26958.
- [197] F. Cataldo, *Journal of Inorganic and Organometallic Polymers* 7 (1997) 35-50.
- [198] S. A. Kahani, M. Sabeti, *Journal of Inorganic and Organometallic Polymers and Materials* 21 (2011) 458.
- [199] W. R. Bowman, C. J. Burchell, P. Kilian, A. M. Z. Slawin, P. Wormald, J. D. Woollins, *Chemistry – A European Journal* 12 (2006) 6366-6381.
- [200] H. A. Früchtl, T. van Mourik, C. J. Pickard, J. D. Woollins, *Chemistry – A European Journal* 15 (2009) 2687-2692.
- [201] S. A. Kahani, M. Sabeti, M. T. Yosefi, *Phosphorus, Sulfur, and Silicon and the Related Elements* 188 (2013) 1584-1590.
- [202] D. R. Dreyer, H. P. Jia, C. W. Bielawski, *Angewandte Chemie International Edition* 49 (2010) 6813-6816.
- [203] B. Tang, L. Y. Deng, *Annals of Statistics* 27 (1999) 1914-1926.
- [204] S. Ray, R. P. Cooney, *Handbook of Environmental Degradation of Materials (Second Edition)*, William Andrew Publishing, Oxford (2012) 213-242.
- [205] T. P. Ryan, *Modern Experimental Design*. Hoboken (NJ):, John Wiley & Sons, Inc., (2007).
- [206] T. Yokoyama, H. Masuda, M. Suzuki, K. Ehara, K. Nogi, M. Fuji, T. Fukui, H. Suzuki, J. Tatami, K. Hayashi, K. Toda, *Nanoparticle Technology Handbook*, Elsevier, Amsterdam (2008) 3-48.
- [207] ASTM Standard D3359-97. Standard Test Methods for Measuring Adhesion by Tape Test. Vol. 06.01. West Conshohocken, PA: ASTM International (2000).
- [208] ASTM Standard D3174-12. Standard Test Method for Ash in the Analysis Sample of Coal and Coke from Coal, West Conshohocken, PA: ASTM International (2012).

- [209] S. J. Gregg, K. S. W. Sing, H. W. Salzberg, *Journal of The Electrochemical Society* 114 (1967) 279C.
- [210] P. D. Patil, V. G. Gude, H. K. Reddy, T. Muppaneni, S. Deng, *Journal of Environmental Protection* 3 (2012) 7.
- [211] H. B. Feng, Y. M. Li, J. H. Li, *RSC Advances* 2 (2012) 6988-6993.
- [212] H. P. Boehm, *Angewandte Chemie International Edition* 49 (2010) 9332-9335.
- [213] Y. G. Andreev, T. Lunstrom, *Journal of Applied Crystallography* 27 (1994) 767-771.
- [214] J. L. Figueiredo, M. F. R. Pereira, M. M. A. Freitas, J. J. M. Órfão, *Carbon* 37 (1999) 1379-1389.
- [215] G. S. Szymański, Z. Karpiński, S. Biniak, A. Świątkowski, *Carbon* 40 (2002) 2627-2639.
- [216] X. Mo, D. E. López, K. Suwannakarn, Y. Liu, E. Lotero, J. G. Goodwin Jr, C. Lu, *Journal of Catalysis* 254 (2008) 332-338.
- [217] P. G. Ren, D. X. Yan, X. Ji, T. Chen, Z. M. Li, *Nanotechnology* 22 (2011).
- [218] I. A. Salem, *Chemosphere* 44 (2001) 1109-1119.
- [219] S. L. H. Rebelo, A. Guedes, M. E. Szefczyk, A. M. Pereira, J. P. Araujo, C. Freire, *Physical Chemistry Chemical Physics* 18 (2016) 12784-12796.
- [220] X. Li, S. P. Lau, L. Tang, R. Ji, P. Yang, *Nanoscale* 6 (2014) 5323-5328.
- [221] J. Bassil, S. Roualdès, V. Flaud, J. Durand, *Journal of Membrane Science* 461 (2014) 1-9.
- [222] Y. Chen, J. Li, T. Mei, X. G. Hu, D. Liu, J. Wang, M. Hao, J. Li, J. Wang, X. Wang, *Journal of Materials Chemistry A* 2 (2014) 20714-20722.
- [223] J. N. Hart, P. W. May, N. L. Allan, K. R. Hallam, F. Claeysens, G. M. Fuge, M. Ruda, P. J. Heard, *Journal of Solid State Chemistry* 198 (2013) 466-474.
- [224] X. Fan, C. Yu, Z. Ling, J. Yang, J. Qiu, *ACS Applied Materials & Interfaces* 5 (2013) 2104-2110.

- [225] D. Yang, A. Velamakanni, G. Bozoklu, S. Park, M. Stoller, R. D. Piner, S. Stankovich, I. Jung, D. A. Field, C. A. Ventrice Jr, R. S. Ruoff, *Carbon* 47 (2009) 145-152.
- [226] R. Rocha, O. Soares, J. Figueiredo, M. Pereira, *C* 2 (2016) 17.
- [227] W. Deng, Y. Zhang, L. Yang, Y. Tan, M. Ma, Q. Xie, *RSC Advances* 5 (2015) 13046-13051.
- [228] A. P. Terzyk, *Journal of Colloid and Interface Science* 268 (2003) 301-329.
- [229] F. Barroso-Bujans, J. L. G. Fierro, S. Rojas, S. Sánchez-Cortés, M. Arroyo, M. A. López-Manchado, *Carbon* 45 (2007) 1669-1678.
- [230] P. Doppelt, G. Hallais, J. Pinson, F. Podvorica, S. Verneyre, *Chemistry of Materials* 19 (2007) 4570-4575.
- [231] D. Geng, S. Yang, Y. Zhang, J. Yang, J. Liu, R. Li, T. K. Sham, X. Sun, S. Ye, S. Knights, *Applied Surface Science* 257 (2011) 9193-9198.
- [232] G. Wang, W. Xing, S. Zhuo, *Electrochimica Acta* 92 (2013) 269-275.
- [233] T. Sharifi, E. Gracia-Espino, H. Reza Barzegar, X. Jia, F. Nitze, G. Hu, P. Nordblad, C. W. Tai, T. Wågberg, *Nature Communications* 4 (2013) 2319.
- [234] K. Ajay, G. Abhijit, P. Pagona, *Journal of Physics: Condensed Matter* 24 (2012) 235503.
- [235] K. S. W. Sing, *Pure and Applied Chemistry* 54 (1982) 2201.
- [236] M. S. Shafeeyan, W. M. A. W. Daud, A. Houshmand, A. Arami-Niya, *Applied Surface Science* 257 (2011) 3936-3942.
- [237] M. G. Plaza, C. Pevida, C. F. Martín, J. Feroso, J. J. Pis, F. Rubiera, *Separation and Purification Technology* 71 (2010) 102-106.
- [238] A. Bagri, C. Mattevi, M. Acik, Y. J. Chabal, M. Chhowalla, V. B. Shenoy, *Nature Chemistry* 2 (2010) 581-587.
- [239] W. Shen, Z. Li, Y. Liu, *Recent Patents on Chemical Engineering* 1 (2008) 27-40.
- [240] M. E. Lipińska, J. P. Novais, S. L. H. Rebelo, B. Bachiller-Baeza, I. Rodríguez-Ramos, A. Guerrero-Ruiz, C. Freire, *Polyhedron* 81 (2014) 475-484.

- [241] X. Yuan, M. Zhang, X. Chen, N. An, G. Liu, Y. Liu, W. Zhang, W. Yan, M. Jia, *Applied Catalysis A: General* 439–440 (2012) 149-155.
- [242] B. Grzyb, S. Gryglewicz, A. Sliwak, N. Diez, J. Machnikowski, G. Gryglewicz, *RSC Advances* 6 (2016) 15782-15787.
- [243] E. Titus, N. Ali, G. Cabral, J. C. Madaleno, V. F. Neto, J. Gracio, P. Ramesh Babu, A. K. Sikder, T. I. Okpalugo, D. S. Misra, *Thin Solid Films* 515 (2006) 201-206.
- [244] J. L. Zimmerman, R. Williams, V. N. Khabashesku, J. L. Margrave, *Nano letters* 1 (2001) 731-734.
- [245] B. J. Matsoso, K. Ranganathan, B. K. Mutuma, T. Lerotholi, G. Jones, N. J. Coville, *RSC Advances* 6 (2016) 106914-106920.
- [246] N. Daems, X. Sheng, I. F. J. Vankelecom, P. P. Pescarmona, *Journal of Materials Chemistry A* 2 (2014) 4085-4110.
- [247] F. A. Permatasari, A. H. Aimon, F. Iskandar, T. Ogi, K. Okuyama, *Scientific Reports* 6 (2016) 21042.
- [248] Y. Zhu, Y. Lin, B. Zhang, J. Rong, B. Zong, D.S. Su, *ChemCatChem* 7 (2015) 2840-2845.
- [249] A. Navaee, A. Salimi, *RSC Advances* 5 (2015) 59874-59880.
- [250] B. J. Schultz, R.V. Dennis, J. P. Aldinger, C. Jaye, X. Wang, D. A. Fischer, A. N. Cartwright, S. Banerjee, *RSC Advances* 4 (2014) 634-644.
- [251] A. Datta, B. K. Mandal, *Renewable and Sustainable Energy Reviews* 57 (2016) 799-821.
- [252] K. Nakamoto, *Infrared and Raman Spectra of Inorganic and Coordination Compounds*, John Wiley & Sons, Inc. (2008) 1-147.
- [253] S. Stankovich, R. D. Piner, S. T. Nguyen, R. S. Ruoff, *Carbon* 44 (2006) 3342-3347.
- [254] G. A. Bowmaker, P. A. Kilmartin, G. A. Wright, *Journal of Solid State Electrochemistry* 3 (1999) 163-171.
- [255] H. Gaspar, C. Pereira, S. L. H. Rebelo, M. F. R. Pereira, J. L. Figueiredo, C. Freire, *Carbon* 49 (2011) 3441-3453.

- [256] K. D. Bomben, J. F. Moulder, P. E. Sobol, W. F. Stickle, Handbook of X-ray Photoelectron Spectroscopy. A Reference Book of Standard Spectra for Identification and Interpretation of XPS Data, Physical Electronics, Eden Prairie, MN (1995).
- [257] T. Umebayashi, T. Yamaki, S. Yamamoto, A. Miyashita, S. Tanaka, T. Sumita, K. Asai, Journal of Applied Physics 93 (2003) 5156-5160.
- [258] G. V. Baryshnikov, R. L. Galagan, L. P. Shepetun, V. A. Litvin, B. F. Minaev, Journal of Molecular Structure 1096 (2015) 15-20.
- [259] M. Shao, Q. Chang, J. P. Dodelet, R. Chenitz, Chemical Reviews 116 (2016) 3594-3657.
- [260] J. Zhang, PEM Fuel Cell Electrocatalysts and Catalyst Layers, Springer, Dordrecht (2008).
- [261] E. A. González, M. Gulppi, M. A. Páez, J. H. Zagal, Diamond and Related Materials 64 (2016) 119-129.
- [262] R. A. Meyers, Encyclopedia of analytical chemistry, John Wiley & Sons, Hoboken (2006).
- [263] D. D. Perrin, B. Dempsey, E. P. Serjeant, Pka Prediction of Organic Acids and Bases, Chapman and Hall, London (1981).
- [264] H. Feng, Y. Li, J. Li, RSC Advances 2 (2012) 6988-6993.
- [265] C. D. Latham, M. I. Heggie, M. Alatalo, S. Öberg, P. R. Briddon, Journal of Physics: Condensed Matter 25 (2013) 135403.
- [266] K. Haubner, J. Murawski, P. Olk, L. M. Eng, C. Ziegler, B. Adolphi, E. Jaehne, ChemPhysChem 11 (2010) 2131-2139.
- [267] S. Wenzhong, L. Zhijie, L. Yihong, Recent Patents on Chemical Engineering 1 (2008) 27-40.
- [268] A. C. Ferrari, J. Robertson, Physical Review B 61 (2000) 14095-14107.
- [269] L. G. Cançado, M. A. Pimenta, B. R. A. Neves, M. S. S. Dantas, A. Jorio, Physical Review Letters 93 (2004) 247401.
- [270] K. N. Kudin, B. Ozbas, H. C. Schniepp, R. K. Prud'homme, I. A. Aksay, R. Car, Nano Letters 8 (2008) 36-41.

- [271] C. H. Chuang, Y. F. Wang, Y. C. Shao, Y. C. Yeh, D. Y. Wang, C. W. Chen, J. W. Chiou, S. C. Ray, W. F. Pong, L. Zhang, J. F. Zhu, J. H. Guo, *Scientific Reports* 4 (2014) 4525.
- [272] F. J. Hernandez, V. C. Ozalp, *Biosensors* 2 (2012) 1.
- [273] A. B. Bourlinos, T. A. Steriotis, M. Karakassides, Y. Sanakis, V. Tzitzios, C. Trapalis, E. Kouvelos, A. Stubos, *Carbon* 45 (2007) 852-857.
- [274] M. Thommes, *Chemie Ingenieur Technik* 82 (2010) 1059-1073.
- [275] G. Srinivas, Y. Zhu, R. Piner, N. Skipper, M. Ellerby, R. Ruoff, *Carbon* 48 (2010) 630-635.
- [276] S. Park, R. S. Ruoff, *Nature Nanotechnology* 4 (2009) 217-224.
- [277] T. Szabó, E. Tombácz, E. Illés, I. Dékány, *Carbon* 44 (2006) 537-545.
- [278] I. Šakinytė, J. Barkauskas, J. Gaidukevič, J. Razumienė, *Talanta* 144 (2015) 1096-1103.
- [279] W. M. Berhanu, G. G. Pillai, A. A. Oliferenko, A. R. Katritzky, *ChemPlusChem* 77 (2012) 507-517.
- [280] H. Kim, A. A. Abdala, C. W. Macosko, *Macromolecules* 43 (2010) 6515-6530.
- [281] C. Wu, X. Huang, G. Wang, X. Wu, K. Yang, S. Li, P. Jiang, *Journal of Materials Chemistry* 22 (2012) 7010-7019.
- [282] M. M. Rahman, H. D. Kim, W. K. Lee, *Journal of Adhesion Science and Technology* 23 (2009) 177-193.
- [283] J. F. Kadla, S. Kubo, *Composites Part A: Applied Science and Manufacturing* 35 (2004) 395-400.
- [284] T. Nakashima, J. Zhu, M. Qin, S. Ho, N.A. Kotov, *Nanoscale* 2 (2010) 2084-2090.
- [285] G. W. Jeon, J. E. An, Y. G. Jeong, *Composites Part B: Engineering* 43 (2012) 3412-3418.
- [286] S. Choudhary, R. J. Sengwa, *Indian Journal of Physics* 86 (2012) 335-340.
- [287] L. S. Taylor, G. Zografis, *Pharmaceutical Research* 14 (1997) 1691-1698.
- [288] P. F. Li, Y. Xu, X. H. Cheng, *Surface and Coatings Technology* 232 (2013) 331-339.

- [289] Y. He, Y. Liu, T. Wu, J. Ma, X. Wang, Q. Gong, W. Kong, F. Xing, Y. Liu, J. Gao, *Journal of Hazardous Materials* 260 (2013) 796-805.
- [290] N. Wang, S. Ji, J. Li, R. Zhang, G. Zhang, *Journal of Membrane Science* 455 (2014) 113-120.